

**ANALOG QUANTUM SIMULATORS FOR QUANTUM
ADVANTAGE AND QUANTUM MACHINE LEARNING**

by

SUPANUT THANASILP
(MSci, Imperial College London)

**A THESIS SUBMITTED FOR THE DEGREE OF
DOCTOR OF PHILOSOPHY**

in

PHYSICS

**CENTRE FOR QUANTUM TECHNOLOGIES
NATIONAL UNIVERSITY OF SINGAPORE**

2022

Supervisor:

Associate Professor Dimitris G. Angelakis

Declaration

I hereby declare that this thesis is my original work and it has been written by me in its entirety. I have duly acknowledged all the sources of information which have been used in the thesis.

This thesis has also not been submitted for any degree in any university previously.

Supanut Thanasilp

29 Sep 2022

To my family and friends

Acknowledgement

I would like to take this opportunity to express my sincere gratitude to many people who have direct or indirect involved in my PhD journey. The success of my PhD study could not be happened without them.

Firstly, I would like to thank my beloved senior, Dr.Jirawat, who introduced this research field and his supervisor to me. That was the beginning of my PhD journey and brought me here.

Secondly, I am very thankful to my supervisor, Associate Professor Dimitris G. Angelakis, who gave me an opportunity to work under his supervision and in his research group. He has always given invaluable guidance and feedback, that are very helpful and drive me deeper into the field.

Thirdly, I would also like to thank CQT and its staff, that has provided me research resources and facilities and helped with administrative matters. Also, team members in Dimitris Lab for being friendly and making relax lab atmosphere.

Next, I would like to thank my friends and family for their 24/7 support and being there for me whenever I need. Also, thanks for feeding me good food and drink on the long/stressful day and also taking care of me even after I was drunk. Thanks for really fun time playing badminton. Thanks for making fun of me when we played GatikPhone. Those are really some of fun and enjoyable moments in this harsh PhD path. My beloved friends, whom I love and cherish, Dr.Radit, Dr.Rattakorn, Dr.Wanwisa, Thanawin, Dr.Nette, Dr.Pojchanun, Dr.Sippanat, Dr.Kittipitch, Nuri, Thitinan, Walaiporn, Oranatt, Chitinart, and Panida.

Lastly, thank you, myself, for still keep fighting and surviving until reach this stage of life.

Contents

Author publications	viii
List of Figures	x
List of Tables	xviii
1 Introduction	1
1.1 Quantum simulation	2
1.2 Quantum primacy with NISQ devices	4
1.2.1 Requirements for demonstrating quantum primacy	5
1.2.2 Quantum random sampling tasks	7
1.2.3 Examples of quantum primacy proposals for NISQ devices	9
1.3 Quantum machine learning	11
1.4 Thesis overview	15
1.5 Related on-going work by the author	17
2 Signatures of a quantum advantage in driven quantum systems	18
2.1 Introduction	18
2.2 Framework	20
2.2.1 Driven analog quantum systems and Floquet ETH	20

2.2.2	Sampling quantum advantage	22
2.3	Sampling from COE dynamics is classically intractable	24
2.3.1	#P hardness of simulating COE dynamics	25
2.3.2	Anti-concentration of COE dynamics	31
2.3.3	An absence of an efficient classical machine to sample from COE dynamics	34
2.4	Implications of COE hardness for driven thermalized quantum systems	37
2.4.1	Example of driven thermalized many-body systems	40
2.4.2	Undriven thermalized many-body systems	41
2.5	Conclusion and outlook	44
3	Probing phase transitions with quantum advantage signatures	46
3.1	Introduction	46
3.2	Quantum phases in driven disordered Ising spin chains	50
3.2.1	Model	50
3.2.2	Phases and level-statistics	52
3.3	Complexity of sampling from different phases	55
3.3.1	Quantum primacy in the driven thermalized phase	56
3.3.2	Computational complexity of the MBL phase and the high frequency regime	58
3.4	Quantum phases from primacy signatures: A new order parameter .	61
3.4.1	Phase diagram	61

3.4.2	The effect of noise on probing quantum phase transitions using KLD	62
3.4.3	Porter-Thomas distribution and infinite temperature thermalization	64
3.4.4	Drive-induced long-range multi-body interactions	66
3.4.5	Entanglement entropy as an alternative signature	70
3.5	Conclusion and outlook	71
4	Parametrized analog quantum systems for machine learning applications	74
4.1	Introduction	74
4.2	General framework	77
4.2.1	Quench dynamics as a parametrized model	77
4.2.2	The four phases of $U(\boldsymbol{\theta}_m)$	78
4.2.3	Driven disordered quantum Ising chains	80
4.3	Expressibility of driven quantum-many body systems	81
4.3.1	Expressibility and quantum primacy	82
4.3.2	Achieving quantum primacy with quenched quantum many-body systems	83
4.4	Trainability of driven analog quantum-many body systems	85
4.4.1	Generative modeling in classical machine learning	86
4.4.2	Sequential training scheme using an analog quantum model	88
4.4.3	Training results	89

4.5	Conclusions	92
5	Conclusion and Future Work	94
5.1	Conclusion	94
5.1.1	Summary of results	94
5.1.2	Future prospects	95
	Bibliography	97
A	Mapping procedure from COE dynamics to complex Ising models	135
A.1	One-qubit example	135
A.2	Two-qubit example	139
A.3	Full COE dynamics	140
B	MBL phase and its sampling complexity	142
B.1	General framework	142
B.2	Concentration of output distribution	143
B.3	Complexity of sampling task	144

Author publications

- [1] J. Tangpanitanon, S. Thanasilp, M.-A. Lemonde, N. Dangiam, and D. G. Angelakis, “Quantum supremacy in driven quantum many-body systems”, *arXiv preprint arXiv:2002.11946*, 2020. [Online]. Available: <https://arxiv.org/abs/2002.11946>.
- [2] S. Thanasilp, J. Tangpanitanon, M.-A. Lemonde, N. Dangiam, and D. G. Angelakis, “Quantum supremacy and quantum phase transitions”, *Phys. Rev. B*, vol. 103, p. 165 132, 16 Apr. 2021. [Online]. Available: <https://link.aps.org/doi/10.1103/PhysRevB.103.165132>.
- [3] J. Tangpanitanon, S. Thanasilp, N. Dangiam, M.-A. Lemonde, and D. G. Angelakis, “Expressibility and trainability of parametrized analog quantum systems for machine learning applications”, *Phys. Rev. Research*, vol. 2, p. 043 364, 4 Dec. 2020. [Online]. Available: <https://link.aps.org/doi/10.1103/PhysRevResearch.2.043364>.
- [4] B. Tan, M.-A. Lemonde, S. Thanasilp, J. Tangpanitanon, and D. G. Angelakis, “Qubit-efficient encoding schemes for binary optimisation problems”, *Quantum*, vol. 5, p. 454, 2021. [Online]. Available: <https://quantum-journal.org/papers/q-2021-05-04-454/>.

AUTHOR PUBLICATIONS

- [5] S. Thanasilp, S. Wang, N. A. Nghiem, P. J. Coles, and M. Cerezo, “Subtleties in the trainability of quantum machine learning models”, *arXiv preprint arXiv:2110.14753*, 2021. [Online]. Available: <https://arxiv.org/abs/2110.14753>.

- [6] S. Thanasilp, S. Wang, M. Cerezo, and Z. Holmes, “Exponential concentration and untrainability in quantum kernel methods”, *arXiv preprint arXiv:2208.11060*, 2022. [Online]. Available: <https://arxiv.org/abs/2208.11060>.

List of Figures

2.1 **Mapping COE dynamics to the partition function of complex Ising lattices:** (a) An example of a random circuit that generates COE dynamics and its conversion to the Ising model. (b) An example of a simple random quantum circuit, illustrating the mapping to the classical Ising model. STEP I to STEP III in the diagrammatic procedure are shown in (b)-(d), respectively. (e) Lookup table for the contribution of each gate to the local fields h_i , h_j and the interaction J_{ij} in the Ising lattice. 28

2.2 (a) The eigenstate distribution $d_n(\mathbf{z})$ for the Ising and the BH models. The blue line is the Bessel function of the second kind predicted by COE. (b) The statistics of level spacings obtained from the Ising and the BH chain at $M = 1, 25$. The blue dashed and the solid lines are the POI and the COE distributions, respectively. Ising and BH parameters: $L = 10$ (with half-filling for the BH model), $W = 1J, B_0 = -\delta B = F_0 = -\delta F = 1.25J, \omega = 8J$, and 500 disorder realizations. 37

2.3 The l_1 -norm distance between the output distribution from different quantum systems and the Porter-Thomas distribution at different m . The results from the Ising chain and the BH chain are labeled as circles and squares, respectively. Ising and BH parameters: $L = 10$ (with half-filling for the BH model), $W = 1J, B_0 = -\delta B = F_0 = -\delta F = 1.25J, \omega = 8J$, and 500 disorder realizations. The inset shows the plot of l_1 -norm distance in the long time limit as a function of L 38

2.4 **Undriven thermalized Ising models versus the GOE:** (a) Level-spacing statistic of an ensemble $\{\hat{H}\}$ and their corresponding long-time evolution operator \hat{U} obtained from the physical Ising system (circle) and the GOE (square). The blue dashed and the orange solid lines are theoretical predictions for the POI and the GOE distributions, respectively. (b) The eigenstate distribution $d_n(\mathbf{z})$ [see Eq. (5) of the main text] with the GOE prediction (solid line). (c) The l_1 -norm distance between the output distribution and the PT distribution as a function of time. The driven case studied in the main text is presented for comparison. The parameters used are: $L = 9, W = 1.5J, B_0 = 1.25J$ ($\delta B = -1.25J, \omega = 8J$ for the driven case) and 500 disorder realizations. 42

3.1 Schematic of a periodically driven quantum Ising chain with nearest-neighbor interactions and disordered onsite energies. 49

3.2 Phase diagram and level statistics of the driven disordered Ising

spin chain. (a) Average level spacing $\langle r \rangle_{\hat{U}_F}$ of the full unitary \hat{U}_F as a function of the disorder strength W/J and the driving frequency ω/J for $L = 9$ and $B_0 = -\delta B = 1.25J$. (b) A cut along the frequency $\omega = 8J$ [vertical dashed line in (a)] shows $\langle r \rangle_{\hat{U}_F}$ as a function of W/J and captures the phase transition from driven thermalized to the driven MBL. (c) A cut along $W = 4J$ [horizontal dashed line in (a)] captures the transition as a function of ω/J from the driven thermalized phase to the prethermalized regime and beyond. The red triangles represent the mean value $\langle r \rangle_{\hat{U}_0}$ computed only considering the evolution under \hat{H}_0 for a time $t = 2\pi/\omega$. (d)-(f) Full distribution $\text{Pr}(r)$ for the driven thermalized phase ($W = 4J, \omega = 4.2J$) following the COE, MBL phase ($W = 30J, \omega = 8J$) following POI and the high frequency regime ($W = 4J, \omega = 20.1J$) converging towards the GOE respectively. In (d), the statistics of \hat{U}_F and \hat{U}_0 drastically differ while they converge in (f); contrasting the importance of the the multi-body long-range interaction induced by the drive at different ω . Each data point results from 100 disorder realizations. 51

3.3 Reaching the PT distribution. (a) $\text{KLD}(\text{Pr}(p) \parallel \text{PT}(p))$ with $p = p_m(\mathbf{z})$ as a function of the driving cycle m for the driven thermalized phase ($W = 3J, \omega = 8J$; dark red squares) , the driven MBL phase ($W = 30J, \omega = 8J$; blue circles) and the high frequency regime ($W = 4J, \omega = 20J$; green triangles). (b)-(d) Output probability distributions $\text{Pr}(Np)$ for $m = 10$ in the three different regimes. (b) $\text{Pr}(Np)$ in the driven thermalized phase ($\omega = 8J$) is in a good agreement with the PT distribution (black line) while it is not in (c) for the high frequency regime and in (d) for the driven MBL phase. The other parameters are $L = 9$ with $N = 2^L$, $B_0 = -\delta B = 1.25J$ and each data points has been computed over 100 disorder realizations. 58

3.4 Probing the phase diagram with the $\text{KLD}(\text{Pr}(p) \parallel \text{PT}(p))$. (a) $\text{KLD}(\text{Pr}(p) \parallel \text{PT}(p))$ with $p = p_m(\mathbf{z})$ after $m = 10$ driving cycles as a function of the disorder strength W/J and the driving frequency ω/J . The solid black line represents the parameters for which $\langle r \rangle_{\hat{U}_F} = 0.51$ as a comparison with Fig. 4.1 (a). (b) A cut along the frequency $\omega = 8J$ (vertical dashed line in (a)) comparing the $\text{KLD}(\text{Pr}(p) \parallel \text{PT}(p))$ (blue dot, left y-axis) with $\langle r \rangle_{\hat{U}_F}$ (gray squares, right y-axis) as a function of W/J along the phase transition from driven thermalized to driven MBL. (c) A cut along $W = 4J$ (horizontal dashed line in (a)) as a function of ω/J demonstrates the transition towards the prethermalization regime. This time, we compare the $\text{KLD}(\text{Pr}(p) \parallel \text{PT}(p))$ with $\langle r \rangle_{\hat{U}_F}$ and $\langle r \rangle_{\hat{U}_0}$ (see Fig. 4.1 (c) and main text). The other parameters are as in Fig. 4.1. 60

3.5 The effect of noise on probing quantum phase transitions with KLD: (a) Output probability distribution $\text{Pr}(Np)$ for $m = 10$ in the driven thermalized phase ($W = 4J, \omega = 8J$) as a function of noise strengths ($\gamma = \gamma_1 = \gamma_2$). The phase transition with respect to disorder W/J (b) and driving frequency ω/J (c) can be obtained by measuring the KLD to PT from the output state even in presence of finite coupling to the environment. For the circle data points, γ_1 and γ_2 are taken to be consistent with the IBMQ cloud-based quantum computing platform [173] while the triangle data points are obtained by doubling those rates. The other parameters are as in Fig 3.4. 63

3.6 Benchmarking the efficiency of producing the PT distribution with analog and digital approaches: (a) a circuit diagram of the analog driven quantum Ising chain with m driving cycles. (b) a circuit diagram of random quantum circuits containing m layers of random single qubits in the set $\{\sqrt{\hat{\sigma}^x}, \sqrt{\hat{\sigma}^y}, \hat{T}\}$ and controlled-Z gates. (c) ((d)) $\text{KL}(\text{Pr}(p) \parallel \text{PT}(p))$ as a function of m and the size of the system L for the analog (digital) approach. (e) The output distribution, weighted by $N = 2^L$, in the analog case with $L = 11$ and $m = 40$. The yellow line is the exact PT distribution. (f) KL divergence at the long time limit of the analog and the digital cases as a function of L . ($W = 3J, B_0 = -\delta B = 1.25J, \omega = 8J$ and 500 disorder realizations.) 70

3.7 Probing the phase diagram with entanglement entropy. (a) The average entanglement entropy over six different subsystems, each containing three sites chosen randomly, is used as an alternative quantum primacy signature to revisit the phase diagram. The vertical and horizontal cuts show the average entanglement entropy as a function of (b) W/J and (c) ω/J . The shaded orange region indicates one standard deviation. The horizontal dashed lines represent the maximal entropy at the infinite temperature $S_{\max} = S_e(T_{\text{eff}} = \infty)$. The KLD to PT $\text{KLD}(\text{Pr}(p) \parallel \text{PT}(p))$ (blue circles) and the average level spacing $\langle r \rangle_{\hat{U}_F}$ (grey squares) are also plotted for comparison. All parameters are identical to those in Fig. 3.4. The low variance in the thermalized phase indicates the homogeneity. 72

4.1 Level statistics of $\hat{H}_{\text{ave}}(\boldsymbol{\theta}_m)$ for $f(t) = 0$ and $\hat{U}(\boldsymbol{\theta}_m)$ for $\delta B = -1.25J$. The thermalized and the MBL phases are obtained with $W = 1J$ and $W = 20J$, respectively. ($L = 9$, $\omega = 8J$, $B_0 = 1.25J$, 500 disorder realizations). 81

4.2 **Statistics of parameterized analog quantum many-body evolution:** (a) and (b) shows the eigenstate distribution $\Pr(Nc)$ and the level statistics $\Pr(r_\alpha)$ for the four phases of $\hat{U}(\boldsymbol{\theta}_m)$, respectively with $M = 400$. The shaded areas are the predictions from the CUE statistics. (c) The KLD of the output distribution from the Porter-Thomas distribution as a function of M . (d) The KLD of $p(\mathbf{z}; \boldsymbol{\Theta}_{m+\delta m})$ from $p(\mathbf{z}; \boldsymbol{\Theta}_m)$ as a function of δm . The KLD is averaged over $M \in [378, 400)$ for a given δm . The thermalized and the MBL phases are obtained with $W = 1J$ and $W = 20J$, respectively. ($L = 9$, $\omega = 8J$, $B_0 = 1.25J$ and $\delta B = -B_0$ with the drive, 500 disorder realizations). 85

4.3 **Machine learning with a driven analog quantum processor:** (a) A table demonstrating a real-world application of generative modeling tasks in machine learning. Each customer is asked to rate whether he/she likes (+1) or dislikes (-1) a given product. (b) A sketch of optimization loops used in the training protocol. (c) A diagram showing the movement of the system in the Hilbert space during the training in the MBL phase. 87

4.4 **Training analog quantum systems in the Hilbert space:** (a) The lowest cost function at each training step M for $\delta B = 0$ and $\delta B = -1.25J$. The thermalized and the MBL phases are obtained with $W = 1J$ and $W = 20J$, respectively. The shaded areas represent standard deviations. (b) The cost function at $M = 10^4$ as a function of W . The results are averaged over 10 dataset, i.e., 10 realizations of $\{a_i, b_i\}$ in Eq. (4.11). Each dataset consists of 3000 samples. (c) The averaged level spacing $\langle r_\alpha \rangle$ at $M = 10^4$ as a function of W . ($L = 9, \omega = 8J, B_0 = 1.25J, k_B T_0 = J$ and $D = 200$.) 90

4.5 The lowest cost function at each training step M for $\delta B = -1.25J$ and $W = 30J$. The training data (2,000 samples) and the testing data (1,000 samples) are independently generated from Eq. (4.10). ($L = 9, \omega = 8J, B_0 = 1.25J, k_B T_0 = J$.) 92

List of Tables

- 4.1 A summary of statistics, expressibility, and trainability in the four regimes, defined by whether $\hat{U}(\boldsymbol{\theta}_m)$ is thermalized or MBL and whether $f(t) = 0$ or $f(t) \neq 0$. The symbol ‘-’ indicates that the statistics is not defined. . 77

Chapter 1

Introduction

Performing computation with the principles of quantum mechanics was envisioned in the early 1980s [1–4]. Ever since, the field of quantum computation and simulation has tremendously grown in particular during these recent years with direct industrial involvement from large companies and start-ups around the world [5]. There has been rapid development of quantum hardware across multiple different platforms including superconducting circuits [6, 7], trapped ions [8, 9], ultra-cold atoms in optical lattices [10–12] and many others [13–18]. Despite not being equipped with error correction, currently available quantum devices have the potential to outperform classical computers in some specific computational tasks [19–23]. In this noisy intermediate scale quantum (NISQ) era, analog quantum simulators, which are controllable quantum systems specifically built to mimic other quantum systems of interest, are expected to be much more relevant in terms of practical applications, for example, in the areas of chemistry and material science, and are said to potentially lead to the first practical quantum advantage [20].

In this chapter, we first introduce various relevant concepts including quantum simulation, quantum primacy in NISQ device and quantum machine learning. We

then conclude the chapter with the thesis overview which is broadly concerned about connecting analog quantum simulators with quantum primacy and quantum machine learning.

1.1 Quantum simulation

Understanding nature often requires us to build and study some theoretical models that simplify a system or a real natural process of interest. Through information obtained from solving these models, one can gain new fundamental understanding of the real system, leading to development of more accurate models or some practical applications. For example, simulating aerodynamic models of drag forces can provide us useful insights into how to design wings of an aircraft [24].

Simulation with classical computers has a tremendous impact on wide ranges of scientific and industrial areas [25–30]. In spite of that, there are still various systems where simulating their underlying models can become too complex and require a computational cost that scales inefficiently with the system’s size. In classical physics, these are usually the classical systems which exhibit chaotic behaviors [31]. Hypersensitivity to an initial condition makes it incredibly difficult to simulate a long-time evolution of chaotic systems. In quantum physics, simulating generic quantum systems with classical computers is widely believed to require an exponential computational resource in the system’s size due to exponentially large Hilbert space [20, 32]. As an example, a complete description of a generic quantum state comprised of n spin-half particles is required to store $2^n - 1$ complex numbers in classical computers. It can be extremely challenging for classical computers to

simulate even a quantum system with $n = 50$, requiring large classical memory in order of several petabytes. In quantum chemistry and material science, the number of quantum particles involved in real systems can be much larger than this, rendering exact simulation with classical computers impossible to be implemented in practice [33].

The difficulty in simulating quantum systems with classical computers can be circumvented with quantum simulation. Envisioned by Richard Feynman in 1981, the idea is to build and engineer a controllable quantum system to simulate a quantum model of our interest [4, 20, 34, 35]. There are two main approaches for quantum simulation. The first approach is to discretize an entire evolution of the quantum model into smaller time steps which can be constructed from a series of well-controlled operations applied on single and pairs of qubits [35, 36]. With this digital gate-based approach, one can simulate any arbitrary physical quantum models with local interactions. This generally requires an access to an universal quantum computers with full-fledged error corrections. Despite the rapid development of quantum hardware, current quantum devices, also referred as noisy intermediate-scale quantum (NISQ) devices, are still not error corrected and it may take a long time before a practical realization of such universal fault-tolerant quantum computers.

Alternatively, in the second approach, one can simulate quantum dynamics using analog quantum simulators. These are special purpose quantum computers specifically built such that their natural evolution generated by the underlying Hamiltonian of the analog quantum simulators realizes the quantum dynamics of the complex

quantum models [4, 20, 35]. Albeit a lack of universal programmability, parameters of the hardware’s Hamiltonian can generally be fine-tuned to high precision, allowing us to capture a large family of quantum models. The major benefit of this analog approach is that it generally requires less precise local controls of the quantum hardware and is also more robust to noise, making this a promising application of the near-term quantum devices. There are a plethora of quantum platforms that can implement analog quantum simulation including ultracold atoms in optical lattices [10–12], trapped ions [8, 9], superconducting circuits [6, 7], interacting photons [13, 14] and others [15–18]. Experiments using analog quantum simulators have already provided us deeper physical insights into fundamental questions of quantum physics, ranging from thermalization in isolated quantum systems [37] and effects of disorders in quantum many-body systems [38–40] to better understanding of topological phases [41, 42] and high temperature superconductors [43, 44]. Already, there are some experimental results produced in the regime that cannot be classically simulated with the current state-of-the-art classical algorithms, for example, 2D transitions towards many-body localized (MBL) phase [40].

1.2 Quantum primacy with NISQ devices

The field of quantum computation and simulation has been built on the premise that quantum computers have more computational power than classical computers and promise to solve some difficult problems more efficiently. Apart from simulating quantum systems introduced in the previous section, computational tasks with expected quantum computational advantages include, for example, prime fac-

torization [45], database search [46] and solving a system of linear equations [47]. Efficiently solving these tasks, in turn, has a tremendous impact on various scientific and industrial areas, including information security, drug design, and big data analysis, to name only a few.

The extended Church-Turing thesis states that any physical models of computation can be efficiently simulated using classical computers with only polynomial overhead [48, 49]. In particular, according to the thesis, the separation in computational power between classical and quantum computers should not be possible. One can see the extended Church-Turing thesis in the similar way to the statement that nature is described by local realism. In that case, quantum correlation generated by entanglement leads to the violation of the Bell’s inequality, ruling out the local hidden variable models of nature. Similarly, experiments that demonstrate a quantum computational advantage (also known as “*quantum primacy*”) violate the long-standing extended Church-Turing thesis, marking a crucial milestone in the field of quantum computation [32, 50]. From the theoretical perspective, this implies that there exists computational models power beyond the reach of classical computers. From the practical perspective, this is an important benchmark of available quantum hardware’s capability and boosting our confidence in the eventual arrival of universal fault-tolerant quantum computers.

1.2.1 Requirements for demonstrating quantum primacy

In order to demonstrate quantum primacy, there are a few requirements one must fulfil [21, 50]: (i) define a computational task, (ii) propose a quantum algorithm

that can efficiently solve the task, (iii) state a level of confidence as why this task is not expected to be solved efficiently with classical computers, (iv) experimentally solve the task with quantum computers on the scale that requires too much computational resources with current classical computers, and optionally (v) the mean for verification. We note that a computational task for demonstrating quantum primacy does not need to have any practical interest to real-world problems.

As an example, we can consider performing prime factorization. Here, the task is to simply factorize a large prime integer and this can be solved efficiently using the famous Shor’s algorithm. Our confidence of classical hardness lies in the fact that many smart mathematicians has been working on this problem for very long time and still no efficient classical algorithm has been found. This is further boosted by the practical use of prime factorization in the information security and encryption around the world. In addition, the verification of a solution from factorization is also straightforward by simply multiplying the obtained factors. However, factorizing large integers such as those used in RSA-2048 requires millions of universal quantum computers on the scale of millions physical qubits with low enough error rates to perform error correction [51].

The hardware requirement for using factorization to demonstrate quantum primacy is too far beyond the reach of the NISQ quantum devices. Available universal quantum devices are comprised of up to roughly 100 qubits and can only implement a limited number of quantum operations before computational errors start to dominate [22, 52–55]. Much larger devices up to tens of thousands atoms can be found for analog quantum simulators [20]. Despite being susceptible to

quantum decoherence, NISQ hardware can have the size of the entire Hilbert space that is already not classically simulable even with the currently largest classical supercomputers. Therefore, it is a natural question to ask if we can design the experimental demonstration of quantum primacy using NISQ hardware [19]. This is indeed a very challenging question, as one not only has to identify a task that is in favor of quantum computers but also the task has to be simple enough to be implementable with noisy quantum devices.

1.2.2 Quantum random sampling tasks

Sampling from the output distribution of a quantum state is the most fundamental act one can do to extract information from a quantum system. In fact, measurements in all quantum experiments can be thought as a combination of sampling and classical processing. That is, given an experimental protocol, measurement outcomes are obtained by repeatedly sampling (in some measurement basis) from a output distribution determined by the Born rule, and then quantities of our interest, such as two-point correlation functions, are computed through classical post-processing.

It may not come as a surprise that tasks of sampling from the output distribution generated by random complex quantum evolution are considered the most promising and natural candidates to demonstrate quantum primacy with NISQ devices [21, 50, 56]. Examples of quantum primacy proposals based on quantum random sampling tasks include universal quantum random circuit sampling [57, 58], instantaneous quantum polynomial time (IQP) circuit sampling [59–61] and boson sampling [62–64] (more details in the following section). Experimental implementations of quantum

primacy protocols have recently been done on the scale that becomes intractable for currently available classical supercomputers, achieving quantum primacy with NISQ hardware [22, 52–55, 65]. These quantum primacy experiments have been conducted on superconducting qubits up to 66 qubits for quantum random circuit sampling [22, 52, 65] and on large-scale photonic systems for boson sampling [53–55].

Classical hardness of these quantum random sampling tasks intuitively stems from the speculation that, if the quantum evolution is sufficiently random and complex, classical computers have no apparent structure to be exploited and have to simulate the whole Hilbert space, which requires a resource that grows exponentially with the system’s size [21]. More formally, theoretical studies using tools from the computational complexity theory provide rigorous evidence of the connection between classical hardness and the polynomial hierarchy of computational complexity classes [21, 50, 56–63]. The latter is a complexity-theoretic concept in computer science which informally states that computational tasks can be sorted into different levels of difficulty [66]. The non-collapse of this polynomial hierarchy is a strongly held conjecture in computer science with the most famous example of $P \neq NP$ [60, 62]. In particular to our context, the existence of an efficient classical algorithm implies the collapse of the polynomial hierarchy. As this fundamentally goes against the non-collapse of the polynomial hierarchy, we conclude that a classical algorithm that can efficiently solve these sampling tasks does not exist.

Using the computational complexity theory provides us much stronger confidence of classical hardness. While it is undoubtedly true that factorizing integers and simulating strongly interacting quantum many-body systems cannot be done

efficiently with the best known classical algorithms, their classical hardness arguments do not exclude the possibility that efficient classical algorithms exist and we have just not yet discovered them. This leaves a room for skeptics who doubt potentials of quantum computers. The lack of imagination has been taken care with the non-collapse of the polynomial hierarchy which ensures the absence of efficient classical algorithms.

1.2.3 Examples of quantum primacy proposals for NISQ devices

In this section, we introduce some quantum primacy proposals based on sampling tasks, including universal quantum random circuit sampling, IQP circuit sampling and boson sampling.

1.2.3.1 Universal quantum random circuit sampling

The universal quantum random circuit sampling is arguably the most famous quantum primacy proposal. The complex quantum evolution is generated by implementing a random circuit where each quantum gate is randomly selected from a universal gate set [57, 58]. Intuitively, the protocol aims to uniformly explore the entire Hilbert space as fast as possible with increasing layers of the circuit. The milestone of experimentally demonstrate a quantum computational advantage for the very first time has been marked by sampling from a quantum random circuit comprised of 53 qubits and 20 layers [22]. The follow-up experiments have implemented up to 66 qubits [52, 65].

There are variants on how to construct a universal gate set and the selection rules

of quantum gates. As an example, we consider the protocol provided in Ref. [22]. For each layer of a circuit, single qubit gates are randomly selected to apply on all qubits from a gate set $\{\sqrt{\hat{\sigma}^x}, \sqrt{\hat{\sigma}^y}, \hat{W}\}$ where $\hat{\sigma}^x$ (and $\hat{\sigma}^y$) is the Z -(and X -) Pauli matrices, and $\hat{W} = (\hat{\sigma}^x + \hat{\sigma}^y)/2$. After randomly implementing single-qubit gates, a fixed two-qubit entangling gate is applied to a particular pair of qubits. The entangling gate iSWAP^* is a native gate specifically to the hardware, which is given by

$$\text{iSWAP}^* = \begin{pmatrix} 1 & 0 & 0 & 0 \\ 0 & 0 & -i & 0 \\ 0 & -i & 0 & 0 \\ 0 & 0 & 0 & e^{-i\pi/6} \end{pmatrix}. \quad (1.1)$$

1.2.3.2 IQP circuit sampling

Instantaneous quantum polynomial time (IQP) circuit sampling is considered as one of the earliest proposals to demonstrate a sampling quantum computational advantage dated back to 2009 [59–61]. The IQP circuit structure consists of a layer of Hadamard gates on all qubits, followed by an arbitrary diagonal unitary in computational basis $\hat{\mathcal{Z}}$, and another layer of Hadamard gates i.e., $\hat{U}_{\text{IQP}} = \hat{\mathcal{H}}\hat{\mathcal{Z}}\hat{\mathcal{H}}$. IQP circuits have a connection with the measurement-based quantum computation and can be formulated to the Hamiltonian time evolution.

1.2.3.3 Boson sampling

Another earliest proposal to demonstrate a quantum computational advantage is boson sampling [62–64]. Here, photons are injected into a linear optical networks

consisting of phase shifters and beam splitters, and the measurement in the Fock basis is done at the end of the network. The output distribution due to photon interference is closely related to computing the permanent of a matrix, which is a root of the classical hardness [63].

We note that, in the original proposal, the injected photons are required to be in a Fock state, which is experimentally challenging to implement on the intermediate-to-large scale. An alternative protocol, known as Gaussian boson sampling, replaces an input Fock state with Gaussian photons and is more experimental friendly. The Gaussian boson sampling has been experimentally implemented on the scale that is classically intractable with current supercomputers, demonstrating quantum primacy in photonic platforms [53–55].

1.3 Quantum machine learning

Data analysis has been revolutionized over the past decades due to the advent of machine learning, leads to an enormous impact on our society. Machine learning offers us profound ways to construct models and algorithms which are capable of learning and recognizing hidden complex patterns in data without being explicitly programmed to do so.

Broadly speaking, one can categorize approaches in machine learning into 3 different ways [67]. In supervised learning, models are trained over a training dataset comprised of input data and their associated true labels in such a way that model predictions are in good agreement with the true labels. The aim here is to have trained models that do not only perform well over training data but also make good

predictions on unseen input data (i.e., good generalization). Supervise learning has a wide range of practical applications such as image classification [68], speech recognition [69] and stock price prediction in finance [70]. In unsupervised learning, the training data do not contain true labels and models are trained to identify underlying data structure. Well known examples of unsupervised learning include clustering and generative modelling which leads to applications such as product recommendations for customers [71]. Lastly, in reinforcement learning, agents are learnt to take actions and interact with an environment to maximize their returned rewards. Applications of reinforcement learning, for example, include autonomous vehicles [72] or building agents that are capable of playing games [73].

On the other hand, quantum systems are well known to generate complex patterns intractable to classical computers. One can then expect quantum computers can be applied to machine learning problems. This is exactly the field of quantum machine learning (QML), which has recently gained much attention due to its promise to achieve a practical quantum advantage in data analysis [23, 74–80].

So far, one can separate the developments of QML into 2 revolutionary waves. The first wave of QML dated back to early 2010s has mainly focused on how to speed up already existing machine learning algorithms using quantum computers [74, 81–84]. Most machine learning algorithms (e.g., support vector machine) rely on performing linear algebra subroutines such as solving linear equations or finding eigenvalues and eigenvectors. These subroutines can be performed on quantum computers using quantum algorithms such as the famous HHL algorithm for solving linear equations [47]. As a consequence, the number of operations required to

execute existing machine learning algorithms can be reduced, potentially leading to an exponential speed up in some particular circumstances. Nevertheless, we note that there are some caveats one has to consider. For example, the process of loading classical data into quantum computers and read-out measurements leads to an overhead, which can even cancel out the exponential speed up obtained from running quantum algorithms [74].

The second revolutionary wave of QML has recently started off as one of the applications for NISQ hardware but soon realizes its potential to extend beyond the NISQ era [85, 86]. Here quantum systems with variational parameters are employed as machine learning models and an expectation value of some observable is commonly interpreted as an output from the models [85–87].

Expressibility generally concerns with how large a class of output functions can be represented by a quantum model. Measuring expressibility of quantum model can be done in different ways depending on the tasks [88–92]. For example, consider unsupervised generative modelling tasks that aim to train output distributions of the model to mimic an unknown target distribution. In this case, the expressibility of the model can be seen as complexity of output distribution. Translating this into the language of quantum mechanics, we can measure the expressive power of the quantum model as how large the quantum model can explore the Hilbert space [93].

Similar to training the conventional machine learning models such as deep neural networks, the quantum machine learning models can be trained by adjusting the variational parameters such that the model outputs are in good agreement with training data. How agreeable our model outputs are to the training data can be

quantified with a loss function, which in turn leads to a loss function landscape in parameter space. Trainability of the quantum model can be seen as how difficult it is to navigate through this loss landscape in an attempt to reach a global minimum [94–100]. In the context of QML, there exist phenomena known as barren plateaus where the loss landscapes become exponentially flat (in the system’s size), leading to the untrainability of the quantum models [94]. Barren plateaus can arise from various features including too large expressibility of the models [94, 97], large entanglement [101], global measurement [95] and noise [102]. Designing the model architectures that can avoid barren plateaus and guarantee the training success is an active research in QML [103, 104].

Ultimately, we hope that well-trained quantum models can generalize beyond the training data. This is the question of generalization which has been studied in [78–80, 105]. Other key theoretical questions in this framework include what kind of machine learning problems and datasets are more suited for the QML models [23, 75–77], how to properly design architectures of the QML models to incorporate the data structure [106, 107].

In contrast to the first QML wave where a quantum advantage is expected to be in the less number of required operations, our main goal here is to establish that quantum models can either be trained with fewer training data or provide better predictions on unseen data (i.e., better generalization). Intuitively, this can be achieved by constructing QML models that can recognize classically intractable complex patterns. Already, some theoretical results have rigorously shown the superiority of the QML models over the classical models in some machine learning

tasks [23, 75–80].

1.4 Thesis overview

While patiently awaiting for the arrival of universal fault-tolerant quantum computers, analog quantum simulators are anticipated to play a crucial role in this NISQ era. This thesis is broadly about how analog quantum simulators can be related to quantum primacy and quantum machine learning. We give an outline of the thesis below.

Although analog quantum simulators can be used to produce experimentally results that are in the classically intractable regime, these measured quantities in the large scale experiments are not rigorously guaranteed to be classically hard by tools from the computational complexity theory. Proposals which demonstrate quantum primacy in the similar fashion as quantum random circuit sampling or boson sampling are still limited. In Chapter 2, we attempt to bridge the gap by proposing a experimentally-friendly quantum primacy proposal based on generic periodically driven analog quantum many-body systems in the thermalized phase. Particularly, we investigate the sampling complexity of periodic evolution of a unitary drawn from the Circular Orthogonal Ensemble (COE) which is a random matrix ensemble with time-reversal symmetry. We provide formal evidence demonstrating the absence of efficient classical algorithms to perform such sampling task unless the polynomial hierarchy collapses. As COE is closely connected with driven analog quantum systems in the thermalized phase, this result suggests that those driven systems could constitute practical candidates for a sampling quantum computational

advantage. To further support this, we give numerical examples of driven disordered Ising chains and 1D driven Bose-Hubbard model.

In Chapter 3, we show how the aforementioned proposed protocol to demonstrate quantum primacy can be extended to explore dynamical quantum phase transitions in periodically-driven quantum many-body systems. In particular, we propose to use key signatures of quantum primacy as new effective ordered parameters. These include the difference between the output probability distribution and the PT distribution and the predicted entanglement value. As an example, we demonstrate that our approach well captures the phase transition from driven thermalized to many-body localized (MBL) phases in a periodically driven disordered one-dimensional Ising model. In addition, we can probe the transition towards the Floquet prethermalized regime in high-frequency drive. Rediscovering quantum phase diagrams with quantum primacy signatures indicates the fundamental connection between computational complexity and quantum many-body physics.

In Chapter 4, we turn our attention to Quantum Machine Learning (QML) with analog quantum simulators as machine learning models. We investigate the relationship between the phases of matter and the performance of the models. In particular, we study how quench dynamics generated by the driven Ising spin chain can be used to perform an unsupervised generative modelling task. Due to the chaotic behavior of the thermalized phase, the model employed in this phase cannot be trained despite having maximally expressive power. By incorporating large disorders, we show that the model in the MBL phase become trainable while maintaining large expressibility due to the quench. In addition, we study the role of

the external drive and found that it can accelerate the training process. Altogether, this indicates the fundamental link between quantum many-body physics and its application in machine learning.

1.5 Related on-going work by the author

In this section, we summarize other related works by the author that do not appear in this thesis.

At the moment, we have been involved in an on-going experiment with a team led by J.W. Pan and Zhen-Sheng Yuan in University of Science and Technology of China (USTC) to implement the quantum primacy scheme proposed in Chapter 2 with the ultra-cold atom platform up to 32 sites and 20 atoms. Sampling one sample from the experiment requires around 500 seconds. In comparison, estimated time of around 10^4 seconds and classical memory of around 600 TB are required to generate one sample on Frontier supercomputer using exact diagonalization.

Chapter 2

Signatures of a quantum advantage in driven quantum systems

This chapter summarizes the material published in

- J. Tangpanitanon[†], S. Thanasilp[†], MA. Lemonde, N. Dangiam, DG. Angelakis, “Quantum supremacy in driven quantum many-body systems”, arXiv:2002.11946, (2020). ¹

2.1 Introduction

A quantum computational advantage is the ability of quantum devices to efficiently perform certain tasks that cannot be efficiently done on a classical computer [19, 50]. Early proposals for realizing this include boson sampling [56, 62, 63] and random quantum circuits [57, 58, 60]. In both cases, the computational hardness stems from the inability of a classical computer to efficiently sample the output probabilities of a complex quantum evolution. Experimental efforts towards achieving *quantum primacy* include optical networks for boson sampling [53–55, 108–112] and superconducting circuits for quantum random circuits [22, 65, 113].

¹the first two authors have contributed equally and are ordered alphabetically.

CHAPTER 2. SIGNATURES OF A QUANTUM ADVANTAGE IN DRIVEN QUANTUM SYSTEMS

On the other hand, analog quantum simulators are controllable quantum platforms specifically built to implement complex quantum many body models [34, 35, 114, 115]. In these experiments, complex quantum dynamics have been implemented leading to the measured quantities which cannot be reproduced with existing classical numerics and have shed light on important questions in quantum many-body physics [40]. However, rigorous proof of a quantum advantage involving complexity theory in those analog systems is limited to specific models such as the 2D quantum Ising [116, 117] and the 2D cluster-state models [118]. A natural question to ask is: would it be possible to make a complexity statement not only on particular models but on an entire class of quantum many-body systems e.g., when they are in the same quantum phase ?

When generic isolated quantum many-body systems thermalize in the sense that any observables can be obtained from the microcanonical ensemble, they share the same statistical properties with random matrix ensembles [119, 120]. One then can expect to gain some insight about the complexity of the thermalized quantum systems by analyzing an evolution of their respective random matrix ensembles.

In this chapter, we provide strong evidence that sampling from a periodic evolution generated by an instance drawn from a Circular Orthogonal Ensemble (COE) cannot be performed efficiently with a classical computer. Our analysis is based on the absence of collapse of the polynomial hierarchy and a plausible assumption of the worst- to average-case hardness of the sampling task. As shown in Ref. [119, 120], COE is an underlying random matrix ensemble for periodically-driven quantum many-body systems in the thermalized phase. Hence, our findings suggest

CHAPTER 2. SIGNATURES OF A QUANTUM ADVANTAGE IN DRIVEN QUANTUM SYSTEMS

the possibility that sampling from those driven thermalized quantum systems is also a classically intractable task. We further support the link between COE and the thermalized driven quantum systems by numerically examining specific examples of disordered quantum Ising chain driven by a global magnetic field and the one-dimensional Bose-Hubbard (BH) model with modulated hoppings. We note that the suggestion to extend the results found in the random matrix ensemble to physical systems only plausible in the driven case. This is because the relation between a random matrix ensemble and physical system are much stronger in the driven case compared to the static one, due to the external drive generating additional randomness into the systems lifting most of the physical constraints imposed by local interactions. To clarify this point, we further discuss the difference between the driven thermalized and undriven thermalized phases of the physical systems. As periodically driven systems have been implemented experimentally with current available quantum hardware [10, 37, 38, 113, 121–124], this makes our results also a broad interest to the experimental community.

2.2 Framework

2.2.1 Driven analog quantum systems and Floquet ETH

Let us consider a generic periodically-driven quantum many-body system whose Hamiltonian is described by $\hat{H}(t) = \hat{H}_0 + f(t)\hat{H}_d$. Here \hat{H}_0 is the undriven Hamiltonian, \hat{H}_d is the driving Hamiltonian such that $[\hat{H}_0, \hat{H}_d] \neq 0$, and $f(t)$ is periodic with period T . We require that the time-averaged Hamiltonian $\hat{H}_{\text{ave}} = \frac{1}{T} \int_0^T \hat{H}(t) dt$

CHAPTER 2. SIGNATURES OF A QUANTUM ADVANTAGE IN DRIVEN
QUANTUM SYSTEMS

describes an interacting many-body system [125].

Let $\mathcal{Z} = \{|\mathbf{z}\rangle = \otimes_i^L |z_i\rangle\}$ be a complete basis of many-body Fock states, where $z_i = \{0, 1, 2, \dots, D_i - 1\}$ denotes the basis state of a local quantum system of dimension D_i and where $i \in [1, L]$. In what follows, we assume without loss of generality that $D_i = D$ for all i , resulting in an Hilbert space of dimension $N = D^L$. The state after M driving periods is $|\psi_M\rangle = \hat{U}_F^M |\mathbf{z}_0\rangle$, where $\hat{U}_F = \hat{\mathcal{T}} \exp\left(-i \int_0^T \hat{H}(t) dt\right) \equiv \exp\left(-i \hat{H}_F T\right)$ and $\hat{\mathcal{T}}$ is the time-ordering operator. We assume that the initial state $|\mathbf{z}_0\rangle$ is a product state. The effective time-independent Floquet Hamiltonian \hat{H}_F fully describes the dynamics probed at stroboscopic times $t = nT$. The probability of measuring the Fock state $|\mathbf{z}\rangle$ is then $p_M(\mathbf{z}) = |\langle \mathbf{z} | \psi_M \rangle|^2$ with

$$\langle \mathbf{z} | \psi_M \rangle = \sum_{\mathbf{z}_1, \dots, \mathbf{z}_{M-1} \in \mathcal{Z}} \prod_{m=0}^{M-1} \langle \mathbf{z}_{m+1} | \hat{U}_F | \mathbf{z}_m \rangle, \quad (2.1)$$

where the sum is performed over $M - 1$ complete sets of basis states. More precisely, the set of basis states $\{|\mathbf{z}_m\rangle\}$ is associated with the quantum evolution after m driving cycles with \mathbf{z}_0 ($\mathbf{z}_M = \mathbf{z}$) being the initial (readout) configuration. The expression in Eq. (2.1) can be viewed as the Feynman's path integral where each trajectory is defined by a set of configurations $\{\mathbf{z}_0, \mathbf{z}_1, \dots, \mathbf{z}_M\}$. If \hat{U}_F reaches a required level of randomness, there are many random Feynman trajectories that are equally important, leading to the hardness in calculating the output probability of Eq. (2.1).

The ETH states that generic isolated many-body quantum systems thermalize by their own dynamics after a long enough time, regardless of their initial state. In that case, any generic observable is expected to evolve toward the canonical ensemble

CHAPTER 2. SIGNATURES OF A QUANTUM ADVANTAGE IN DRIVEN QUANTUM SYSTEMS

with a finite temperature [119]. For driven quantum many-body systems, it has been shown that not only thermalization still occurs, but that for low-frequency driving, the associated temperature becomes infinite [120]. In this limit, the Floquet operator \hat{U}_F shares the statistical properties of the Circular Orthogonal Ensemble (COE). This is an ensemble of matrices whose elements are independent normal complex random variables subjected to the orthogonality and the unitary constraints.

As directly analyzing a complexity of \hat{U}_F without further specifying structures of the systems is very challenging, in this work we attempt to gain some generic complexity insight of \hat{U}_F from studying periodic evolution of an instance drawn from COE. Particularly, \hat{U}_F in Eq. Equation 2.1 is replaced with \hat{U}_{COE} where \hat{U}_{COE} is a unitary randomly drawn from COE. We later on discuss the implication of this result for periodically driven systems in the thermalized phase in Section 2.4.

2.2.2 Sampling quantum advantage

We first introduce a standard procedure used to prove a quantum advantage in quantum random sampling [21]. To understand the sampling task, we first define some essential terms used in the complexity theory, namely *approximating*, *sampling*, *multiplicative error* and *additive error*. Let us imagine an analog quantum device built to mimic the quantum dynamics that would lead to $p_M(\mathbf{z}) = |\langle \mathbf{z} | \psi_M \rangle|^2$. In practice, such device will encode an output probability $q(\mathbf{z})$ that differs from $p_M(\mathbf{z})$ due to noise, decoherence and imperfect controls. Both probabilities are said to be multiplicatively close if

$$|p_M(\mathbf{z}) - q(\mathbf{z})| \leq \alpha p_M(\mathbf{z}) \quad (2.2)$$

CHAPTER 2. SIGNATURES OF A QUANTUM ADVANTAGE IN DRIVEN
QUANTUM SYSTEMS

where $\alpha \geq 0$. The task of *approximating* $p_M(\mathbf{z})$ *up to multiplicative error* is to calculate $q(\mathbf{z})$ that satisfies the above equation for a given \mathbf{z} . However, such degree of precision is difficult to achieve experimentally as the allowed error is proportional to $p_M(\mathbf{z})$ which can be much smaller than unity. A more feasible task is to *approximate* $p_M(\mathbf{z})$ *up to additive error*, defined as

$$\sum_{\mathbf{z} \in \mathcal{Z}} |p_M(\mathbf{z}) - q(\mathbf{z})| \leq \beta, \quad (2.3)$$

with $\beta > 0$. Note that the additive error involves summing over all possible output strings $\mathbf{z} \in \mathcal{Z}$, while the multiplicative condition applies to each \mathbf{z} individually.

The task of *approximating* $p_M(\mathbf{z})$ even with additive error is still unrealistic as it requires a number of measurements that grows exponentially with the size of the system. What a quantum device can do is to sample strings from $q(\mathbf{z})$. Hence, we define the task of *sampling from* $p_M(\mathbf{z})$ *up to additive error* as generating strings from $q(\mathbf{z})$ while $q(\mathbf{z})$ is additively close to $p_M(\mathbf{z})$. This task is our central focus to show a sampling quantum advantage. We emphasize that it is different from “verification of a quantum advantage” [126] which consists of verifying if Eq. (2.3) holds.

To show that the above sampling task cannot be done efficiently by a classical computer, we follow the standard argument which proceeds as follows. Let us suppose that there is a classical machine \mathcal{C} able to *sample from* $p_M(\mathbf{z})$ *up to additive error* and that the distribution of $p_M(\mathbf{z})$ anti-concentrates, i.e.

$$\Pr \left(p_M(\mathbf{z}) > \frac{\delta}{N} \right) \geq \gamma, \quad (2.4)$$

CHAPTER 2. SIGNATURES OF A QUANTUM ADVANTAGE IN DRIVEN
QUANTUM SYSTEMS

for some positive constants $\delta, \gamma > 0$ for all $\mathbf{z} \in \mathcal{Z}$ [127]. The Stockmeyer theorem states that, with the help of a NP oracle, the machine \mathcal{C} can also *approximate* $p_M(\mathbf{z})$ up to multiplicative error for some outcomes \mathbf{z} [21, 128]. We emphasize that the *sampling* task is converted to the *approximation* task in this step. If the latter is #P-hard, then the existence of that machine \mathcal{C} would imply the collapse of the polynomial hierarchy to the third level, which is strongly believed to be highly unlikely from the computational complexity theory. Hence, assuming that the polynomial hierarchy does not collapse to the third level, we reach the conclusion that a classical machine \mathcal{C} does not exist.

2.3 Sampling from COE dynamics is classically intractable

In this section, we analytically show that sampling up to additive error from a periodic evolution of an instance drawn from COE is classically intractable. The two fundamental conditions of the proof, that is the #P-hardness of *approximating* $\tilde{p}_M(\mathbf{z})$ up to multiplicative error and the anti-concentration of $\tilde{p}_M(\mathbf{z})$, are formally stated in the two following theorems.

Theorem 1 (Worst-case hardness). *Let \mathcal{Y} be a set of output probabilities $\tilde{p}_M(\mathbf{z}) = |\langle \mathbf{z} | \hat{U}_{COE}^M | \mathbf{z}_0 \rangle|^2$ obtained from all possible COE matrices $\{\hat{U}_{COE}\}$ and all possible output strings $\mathbf{z} \in \mathcal{Z}$. Approximating $\tilde{p}_M(\mathbf{z})$ in \mathcal{Y} up to multiplicative error is #P-hard in the worst case.*

Theorem 2 (Anti-concentration). *The distribution of $\tilde{p}_M(\mathbf{z})$ in \mathcal{Y} anti-concentrates*

CHAPTER 2. SIGNATURES OF A QUANTUM ADVANTAGE IN DRIVEN
QUANTUM SYSTEMS

with $\delta = 1$ and $\gamma = 1/e$, where e is the base of the natural logarithm.

In theorem 1, we introduced the key notion of *worst-case* hardness of the entire set of COE matrices $\{\hat{U}_{\text{COE}}\}$. This corresponds to the scenario where at least one instance $\tilde{p}_M(\mathbf{z})$, i.e. a single unitary $\hat{U} \in \{\hat{U}_{\text{COE}}\}$ and a single configuration $\mathbf{z} \in \mathcal{Z}$, is hard to approximate with multiplicative error. More desirable is the *average-case* hardness where most instances are hard. Consequently, to ensure that the hard instance in \mathcal{Y} can be found within $\{\hat{U}_{\text{COE}}\}$ we further assume the following commonly used conjecture which leads to the worst-to-average case reduction in \mathcal{Y} .

Conjecture 1 (Average-case hardness). *For any $1/2e$ fraction of \mathcal{Y} , approximating $\tilde{p}_M(\mathbf{z})$ up to multiplicative error with $\alpha = 1/4 + o(1)$ is as hard as the hardest instance. Here $o(\cdot)$ is the little-o notation.*

In combination of theorems 1 and 2 and the conjecture finally allow us to state the main theorem.

Theorem 3. *Assuming conjecture 1, the ability to classically sample from $\tilde{p}_M(\mathbf{z})$ up to an additive error $\beta = 1/8e$ for all unitary matrices in $\{\hat{U}_{\text{COE}}\}$ implies the collapse of the polynomial hierarchy to the third level.*

In what follows, we address in detail the proofs of our theorems.

2.3.1 #P hardness of simulating COE dynamics

To prove Theorem 1, we first notice that the COE is an ensemble of all orthogonal unitary matrices. This includes the well-known instantaneous quantum polynomial time (IQP) circuits $\hat{U}_{\text{IQP}} = \hat{\mathcal{H}}\hat{\mathcal{Z}}\hat{\mathcal{H}}$, where $\hat{\mathcal{H}}$ consists of Hadamard gates and $\hat{\mathcal{Z}}$ is an

CHAPTER 2. SIGNATURES OF A QUANTUM ADVANTAGE IN DRIVEN
QUANTUM SYSTEMS

arbitrary (possibly non-local) diagonal gate on the computational basis, both acting on all qubits [60]. The IQP circuits constitute one of the early proposals of quantum supremacy. Multiplicative approximation of their output probabilities are known to be #P-hard in the worst case [129, Theorem 1.4]. Since $\hat{U}_{\text{IQP}}^M = \hat{\mathcal{H}}\hat{\mathcal{Z}}^M\hat{\mathcal{H}}$ still adopt the general form of the IQP circuits, we conclude that there exists at least one instance in \mathcal{Y} that is #P-hard for multiplicative approximation. This completes the proof of Theorem 1

Now, we provide evidence to support Conjecture 1, showing how hardness instances could appear on average. To do this, we map the task of approximating an output distributions of COE dynamics onto calculating the partition function of a classical Ising model with random complex fields which is widely believed to be #P-hard on average for multiplicative approximation [61, 116]. In this context, the key is to note that a COE unitary evolution can be written as $\hat{U}_{\text{COE}} = \hat{U}_{\text{CUE}}^T \hat{U}_{\text{CUE}}$, where \hat{U}_{CUE} is a random matrix drawn from the Circular Unitary Ensemble (CUE), i.e., the ensemble of Haar-random matrices [130]. Furthermore, \hat{U}_{CUE} can be decomposed into a set of universal quantum gates which can be mapped onto a complex Ising model. This last step which maps random circuits to complex Ising models has been described in ref. [57] to support the conjecture of the worst-to-average case in the context of random quantum circuits. In the following subsection, we explain the overall concept and physical intuition of the whole mapping procedure.

2.3.1.1 Mapping of approximating output distribution of COE dynamics onto estimating partition function of complex Ising models

The mapping protocol consists of two intermediate procedures. First, we map the COE unitary evolution on *universal* random quantum circuits and, second, we derive a complex Ising model from those circuits following Ref. [57].

Let us begin by expressing an unitary evolution of COE as $\hat{U}_{\text{COE}} = \hat{U}_{\text{CUE}}^T \hat{U}_{\text{CUE}}$ where \hat{U}_{CUE} is a random unitary drawn from the Circular Unitary Ensemble (CUE) i.e. Haar ensemble [130]. We then further decompose \hat{U}_{CUE} into a set of universal quantum gates [57]. Following Ref. [57], we choose random quantum circuits consisting of $n + 1$ layers of gates and $\log_2 N$ qubits, as shown in Fig. 2.1(a). The first layer consists of Hadamard gates applied to all qubits. The following layers consist of randomly chosen single-qubit gates from the set $\{\sqrt{\hat{\sigma}^x}, \sqrt{\hat{\sigma}^y}, \hat{T}\}$ and two-qubit controlled-Z (CZ) gates. Here, $\sqrt{\hat{\sigma}^x}$ (and $\sqrt{\hat{\sigma}^y}$) represents a $\pi/2$ rotation around the X (and Y) axis of the Bloch sphere and \hat{T} is a non-Clifford gate representing a diagonal matrix $\{1, e^{i\pi/4}\}$. Such circuits have been shown to be approximately t -design [131] for an arbitrary large t when $n \rightarrow \infty$, which implies the CUE evolution [132]. The operator \hat{U}_{CUE}^T can be implemented by reversing the order of the gates in \hat{U}_{CUE} and replacing $\sqrt{\hat{\sigma}^y}$ with $\sqrt{\hat{\sigma}^y}^T$. We emphasize that decomposing the COE evolution into the random circuits is only done theoretically with an aim to show the average case hardness. In the real experiments, this COE dynamics is realized by the driven many-body systems.

The mathematical procedure for the mapping from random quantum circuits to classical complex Ising models is discussed in details in Appendix A. Specifically,

CHAPTER 2. SIGNATURES OF A QUANTUM ADVANTAGE IN DRIVEN QUANTUM SYSTEMS

(a) Periodic evolution of COE

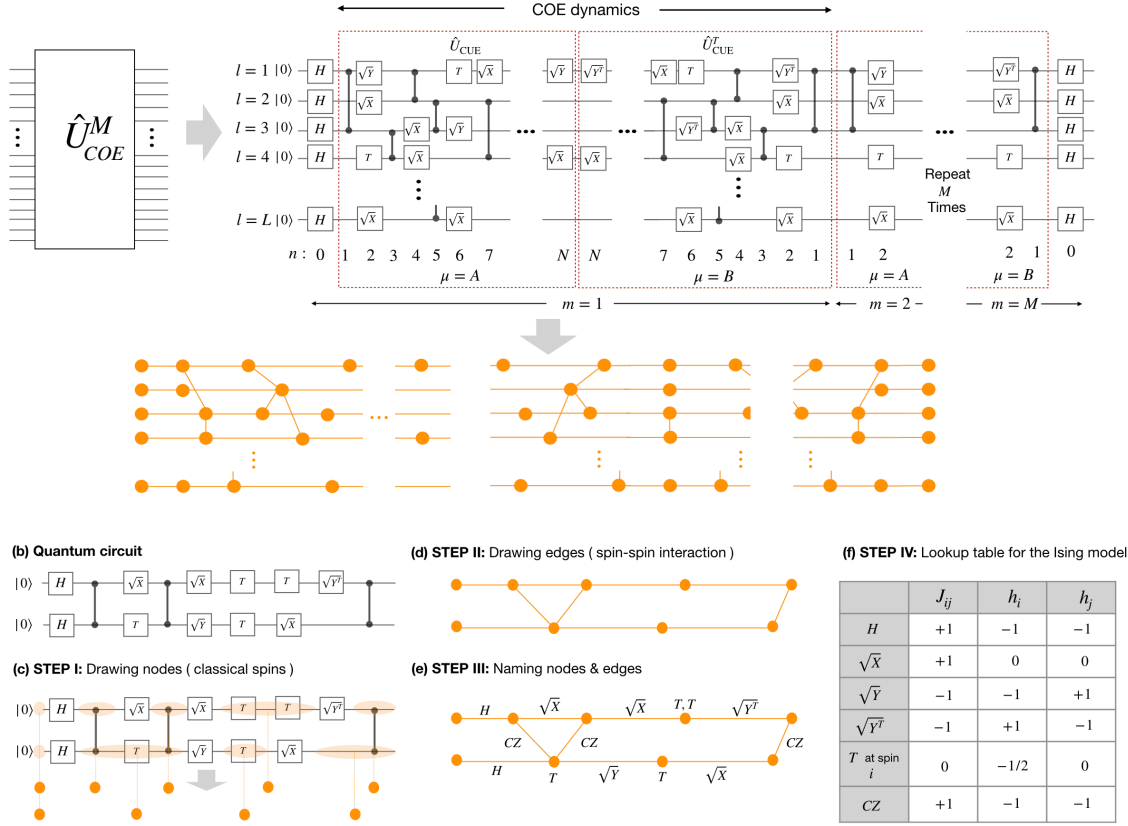


Figure 2.1: **Mapping COE dynamics to the partition function of complex Ising lattices:** (a) An example of a random circuit that generates COE dynamics and its conversion to the Ising model. (b) An example of a simple random quantum circuit, illustrating the mapping to the classical Ising model. STEP I to STEP III in the diagrammatic procedure are shown in (b)-(d), respectively. (e) Lookup table for the contribution of each gate to the local fields h_i , h_j and the interaction J_{ij} in the Ising lattice.

$p_M(\mathbf{z})$ from the circuit $(\hat{U}_{\text{COE}}^T \hat{U}_{\text{COE}})^M$, as depicted in Fig. 2.1(a), can be calculated from the partition function,

$$\langle \mathbf{z} | \hat{U}_{\text{COE}}^M | \mathbf{z}_0 \rangle = \sum_{\mathbf{s} \in \mathcal{S}} A(\mathbf{s}) \exp \left[\frac{i\pi}{4} \left(\sum_i h_i s_i + \sum_{\langle i,j \rangle} J_{ij} s_i s_j \right) \right]. \quad (2.5)$$

Here, $A(\mathbf{s})$ is the degeneracy number associated with a classical spin configuration \mathbf{s} in the lattice \mathcal{S} , $s_i = \pm 1$, h_i represents a on-site field on site i and J_{ij} represents the coupling between the classical spins on site i and j . Since the output probability can

CHAPTER 2. SIGNATURES OF A QUANTUM ADVANTAGE IN DRIVEN QUANTUM SYSTEMS

also be interpreted as the path integral in Eq. (2.5) in the main text, the intuition behind the mapping is that the sum over all possible paths is translated into the sum over all possible classical spin configurations, where the phase accumulated in each path is given by the energy of the complex Ising lattice \mathcal{S} . To gain intuitive understanding of this standard mapping, we provide a diagrammatic approach to visualize the lattice \mathcal{S} and extract the field parameters $\{h_i\}$, $\{J_{ij}\}$. To begin with, we use the random circuit in Fig. 2.1(b) as a demonstration. The mathematical descriptions behind each steps are discussed in the next part.

- STEP I - For each qubit, draw a circle between every consecutive non-diagonal gates, see Fig. 2.1(c). Each circle or ‘node’ represents one classical spin.
- STEP II - For each qubit, draw a horizontal line between every consecutive nodes i,j , see Fig. 2.1(d). These lines or ‘edges’ represent interaction J_{ij} between two neighboring spins in the same row. In addition, draw a line between every two nodes that are connected by CZ gates. These lines represent the interaction J_{ij} between spins in different rows.
- STEP III - Labeling each nodes and edges with the corresponding gates, see Fig. 2.1(e).
- STEP IV - Use the lookup table in Fig. 2.1(f) to specify h_i and J_{ij} introduced by each gate. For example, the $\sqrt{\sigma^y}$ gate that acts between nodes i and j adds -1 to J_{ij} , -1 to h_i and $+1$ to h_j . We use the convention that the leftmost index represents the leftmost node. Also, the two T-gates that are enclosed by

CHAPTER 2. SIGNATURES OF A QUANTUM ADVANTAGE IN DRIVEN
QUANTUM SYSTEMS

the node i will add $0.5 + 0.5 = +1$ to the local field h_i .

- STEP V - Finally, spins at the leftmost side of the lattice are fixed at $+1$, corresponding to the initial state $|\mathbf{0}\rangle$. Similarly, spins at the rightmost side of the lattice are fixed according to the readout state $|z\rangle$.

Following the above recipe, we provide the exact form of the parameters in the Ising model for the COE dynamics in the next part, showing that the field parameters $\{h_i\}$ and $\{J_{ij}\}$ are quasi-random numbers with no apparent structure. Specifically, neither the phase $\pi \sum_i h_i s_i/4$ nor the phase $\pi \sum_{\langle i,j \rangle} J_{ij} s_i s_j/4$ is restricted to the values $0, \pi/2, \pi, 3\pi/2 \pmod{2\pi}$ for each spin configurations \mathbf{s} . Without such stringent restrictions, approximating the partition function up to multiplicative error is known to be $\#P$ -hard in the worst case [129, Theorem 1.9]. This motivates a widely used conjecture in quantum supremacy proposals that such task is also hard on average [61, 116].

We note here the major differences between random quantum circuits as proposed in Ref. [57] and our COE dynamic. The evolution of an instance drawn from COE is periodic and the overall dynamic has discrete time-reversal symmetry, while such symmetry is absent in random quantum circuits in Ref. [57]. In addition, the periodic evolution of COE does not have the t -design property [133, pp.117-119]. Nevertheless, as shown above, the hardness arguments for the random quantum circuits can be naturally applied to our case.

2.3.2 Anti-concentration of COE dynamics

In this section, we provide the proof of Theorem 2 which is the second and necessary ingredient to demonstrate quantum primacy. First, let us consider the output probability $\tilde{p}_M(\mathbf{z}) = |\langle \mathbf{z} | \psi_M \rangle|^2$ with

$$\langle \mathbf{z} | \psi_M \rangle = \langle \mathbf{z} | U_{\text{COE}}^M | \mathbf{0} \rangle \quad (2.6)$$

$$= \langle \mathbf{z} | \left[\sum_{n=0}^{N-1} e^{iME_n} |E_n\rangle \langle E_n| \right] | \mathbf{0} \rangle \quad (2.7)$$

$$= \sum_{n=0}^{N-1} d_n(\mathbf{z}) e^{i\phi_{M,n}} \quad (2.8)$$

$$= \left[\sum_{n=0}^{N-1} d_n(\mathbf{z}) \cos \phi_{M,n} \right] + i \left[\sum_{n=0}^{N-1} d_n(\mathbf{z}) \sin \phi_{M,n} \right] \quad (2.9)$$

$$= a_{\mathbf{z}} + ib_{\mathbf{z}}, \quad (2.10)$$

where N is the dimension of the Hilbert space, $|E_n\rangle$ is an eigenstate of \hat{U}_{COE} with an associated eigenvalue e^{iE_n} , $d_n(\mathbf{z}) = \langle \mathbf{z} | E_n \rangle \langle E_n | \mathbf{0} \rangle$, $\phi_{M,n} = ME_n \bmod 2\pi$, $a_{\mathbf{z}} =$

$$\text{Re} [\langle \mathbf{z} | \psi_M \rangle] = \sum_{n=0}^{N-1} d_n(\mathbf{z}) \cos \phi_{M,n} \text{ and } b_{\mathbf{z}} = \text{Im} [\langle \mathbf{z} | \psi_M \rangle] = \sum_{n=0}^{N-1} d_n(\mathbf{z}) \sin \phi_{M,n}.$$

We now introduce the two following lemmas.

Lemma 1. *The distribution of $d_n(\mathbf{z})$ over $\forall n \in \{0, \dots, N-1\}$ or $\forall \mathbf{z} \in \{0, \dots, D-1\}^L$ is the Bessel function of the second kind.*

Lemma 2. *The distribution of $a_{\mathbf{z}}$ and $b_{\mathbf{z}}$ over $\forall \mathbf{z} \in \{0, \dots, D-1\}^L$ is the normal distribution with zero mean and variance equal to $1/2N$.*

To prove Lemma 1, we first write $d_n(\mathbf{z}) = c_{\mathbf{z},n} c_{\mathbf{0},n}$, where $c_{\mathbf{z},n} = \langle \mathbf{z} | E_n \rangle$ and $c_{\mathbf{0},n} = \langle \mathbf{0} | E_n \rangle$. For the COE dynamics, the coefficients $c_{\mathbf{z},n}$ and $c_{\mathbf{0},n}$ are real numbers

CHAPTER 2. SIGNATURES OF A QUANTUM ADVANTAGE IN DRIVEN
QUANTUM SYSTEMS

following the distribution [130]

$$\Pr(c) = \sqrt{\frac{2N}{\pi}} \exp\left[-\frac{Nc^2}{2}\right]. \quad (2.11)$$

The distribution of $d_n(\mathbf{z})$ can be obtained using the product distribution formula

$$\Pr(d) = \int_0^\infty \Pr(c) \Pr\left(\frac{d}{c}\right) \cdot \frac{1}{c} \cdot dc \quad (2.12)$$

$$= \frac{2N}{\pi} \int_0^\infty \exp\left(-\frac{Nc^2}{2}\right) \exp\left(-\frac{Nd^2}{2c^2}\right) dc \quad (2.13)$$

$$= \frac{2N}{\pi} K_0(Nd), \quad (2.14)$$

where K_0 is the modified Bessel function of the second kind.

To prove Lemma 2, first let us consider the statistics of the phases $\{\phi_{M,n}\}$. We define the level spacing as $r = \min(\delta_{n+1}, \delta_n) / \max(\delta_{n+1}, \delta_n)$ with $\delta_n = \phi_{M,n+1} - \phi_{M,n}$ ². For a single driving cycle $M = 1$, the phases $\{\phi_{1,n}\}$ for COE are known to exhibit phase repulsion, i.e. the phases are correlated [120]. The COE distribution $\Pr_{\text{COE}}(r)$ is depicted in Fig. 4.1(b), where $\Pr_{\text{COE}}(0) = 0$ explicitly indicates the phase repulsion. For multiple driving cycles $M \gg 2\pi/E_n$, the correlations are erased due to energy folding, i.e. the effect of the modulo 2π . This results in the Poisson (POI) distribution of the level spacing, $\Pr_{\text{POI}}(r) = 2/(1+r^2)$, with the peak at $r = 0$, see Fig. 4.1(b). Consequently, the phases $\{\phi_{M,n}\}$ can be thought of as independent variables randomly and uniformly distributed in the range $[0, 2\pi)$.

Now, we note that the distribution of $\cos \phi_{M,n}$ and $\sin \phi_{M,n}$ with $\phi_{M,n}$ being uniformly distributed in the range $[0, 2\pi)$ are (i.e., note that we introduce a shorthand

²This is a standard tool used to analyze phases of matter in quantum many-body systems. More detailed description is given in Chapter 3 where we explore dynamical phase transitions of driven quantum many-body systems.

CHAPTER 2. SIGNATURES OF A QUANTUM ADVANTAGE IN DRIVEN
QUANTUM SYSTEMS

$\phi_{M,n} = \phi$ for readability)

$$\Pr(\cos \phi) = \frac{1}{\pi \sqrt{1 - \cos^2 \phi}}, \quad (2.15)$$

$$\Pr(\sin \phi) = \frac{1}{\pi \sqrt{1 - \sin^2 \phi}}. \quad (2.16)$$

We then calculate the distribution of $\kappa_n \equiv d_n(\mathbf{z}) \cos \phi_{M,n}$ using the product distribution formula, i.e.

$$\Pr(\kappa) = \int_{-1}^1 \frac{1}{\pi \sqrt{1 - \cos^2 \phi}} \cdot \frac{2N}{\pi} K_0 \left(\frac{N\kappa}{d} \right) \cdot \frac{1}{\cos \phi} d \cos \phi \quad (2.17)$$

$$= \frac{N}{\pi^2} K_0^2 \left(\frac{N|\kappa|}{2} \right). \quad (2.18)$$

The mean and the variance of κ_n can be calculated as

$$\langle \kappa \rangle = \int_{-\infty}^{\infty} d \cos \phi \cdot \frac{N}{\pi^2} \cdot K_0^2 \left(\frac{N|\kappa|}{2} \right) \cdot d\kappa = 0 \quad (2.19)$$

$$\text{Var}(\kappa) = \int_{-\infty}^{\infty} (d \cos \phi)^2 \cdot \frac{N}{\pi^2} \cdot K_0^2 \left(\frac{N|\kappa|}{2} \right) \cdot d\kappa = \frac{1}{2N^2}. \quad (2.20)$$

Since $a_{\mathbf{z}}$ is a sum of independent and identically distributed random variables, i.e. $a_{\mathbf{z}} = \sum_{n=1}^{N-1} \kappa_n$, we can apply the central limit theorem for large N . Hence, the distribution of $a_{\mathbf{z}}$ is normal with the mean zero and variance $\text{Var}(a) = N \cdot \text{Var}(\kappa) = 1/2N$. The same applies for the distribution of $b_{\mathbf{z}}$. This completes the proof of Lemma 2.

Theorem 2 can be proven using the fact that the sum of the square of Gaussian variables follows the χ -squared distribution with second degree of freedom $\Pr_{\chi^2, k=2}(p) = \exp\{-p/2\sigma^2\}$ [134]. By specifying the variance obtained in Lemma 2 and normalization, $\Pr(p)$ follows the so-called Porter-Thomas distribution $\Pr_{\text{PT}}(p) = Ne^{-Np}$, which suggests that the system explores uniformly (approximately Haar-

random) the Hilbert space [113, 116]. Since the Porter Thomas distribution anti-concentrates i.e. $\Pr_{\text{PT}}\left(p > \frac{1}{N}\right) = \int_{Np=1}^{\infty} d(Np)e^{-Np} = 1/e$, we complete the proof of the theorem 2.

2.3.3 An absence of an efficient classical machine to sample from COE dynamics

In this section, we provide a detailed proof of Theorem 3 which follows the standard Stockmeyer argument [21].

Let us begin by considering a classical probabilistic computer with an NP oracle, also called a BPP^{NP} machine. This is a theoretical object that can solve problems in the third level of the polynomial hierarchy. The Stockmeyer theorem states that a BPP^{NP} machine with an access to a classical sampler \mathcal{C} , as defined in Section 2.2.2, can efficiently output an approximation $\tilde{q}(\mathbf{z})$ of $q(\mathbf{z})$ such that

$$|q(\mathbf{z}) - \tilde{q}(\mathbf{z})| \leq \frac{q(\mathbf{z})}{\text{Poly}(L)}. \quad (2.21)$$

We emphasise that the BPP^{NP} machine grants us the ability to perform the approximating task, in contrast to the machine \mathcal{C} that can only sample strings from a given distribution. To see how the BPP^{NP} machine can output a multiplicative

CHAPTER 2. SIGNATURES OF A QUANTUM ADVANTAGE IN DRIVEN
QUANTUM SYSTEMS

approximation of $\tilde{p}_M(\mathbf{z})$ for most of $\mathbf{z} \in \mathcal{Z}$, let us consider

$$|\tilde{p}_M(\mathbf{z}) - \tilde{q}(\mathbf{z})| \tag{2.22}$$

$$\leq |\tilde{p}_M(\mathbf{z}) - q(\mathbf{z})| + |q(\mathbf{z}) - \tilde{q}(\mathbf{z})| \tag{2.23}$$

$$\leq |\tilde{p}_M(\mathbf{z}) - q(\mathbf{z})| + \frac{q(\mathbf{z})}{\text{Poly}(L)} \tag{2.24}$$

$$\leq |\tilde{p}_M(\mathbf{z}) - q(\mathbf{z})| + \frac{|\tilde{p}_M(\mathbf{z}) - q(\mathbf{z})| + \tilde{p}_M(\mathbf{z})}{\text{Poly}(L)} \tag{2.25}$$

$$= \frac{\tilde{p}_M(\mathbf{z})}{\text{Poly}(L)} + |\tilde{p}_M(\mathbf{z}) - q(\mathbf{z})| \left(1 + \frac{1}{\text{Poly}(L)}\right). \tag{2.26}$$

The first and the third lines are obtained using the triangular inequality. To get multiplicative approximation of $\tilde{p}_M(\mathbf{z})$ using $\tilde{q}(\mathbf{z})$, we need the term $|\tilde{p}_M(\mathbf{z}) - q(\mathbf{z})|$ to be small. Given the additive error defined in Eq. (3) in the main text, this is indeed the case for a large portion of $\{\mathbf{z}\} \in \mathcal{Z}$. Since the left hand side of Eq. (3) in the main text involves summing over an exponentially large number of terms but the total error is bounded by a constant β , most of the terms in the sum must be exponentially small. This statement can be made precise using Markov's inequality.

Lemma 3 (Markov's inequality). *If X is a non-negative random variable and $a > 0$, then the probability that X is at least a is*

$$\text{Pr}(X \geq a) \leq \frac{\mathbb{E}(X)}{a}, \tag{2.27}$$

where $\mathbb{E}(X)$ is the expectation value of X .

By setting $X = |\tilde{p}_M(\mathbf{z}) - q(\mathbf{z})|$, we get

$$\text{Pr}_{\mathbf{z}}(|\tilde{p}_M(\mathbf{z}) - q(\mathbf{z})| \geq a) \leq \frac{\mathbb{E}_{\mathbf{z}}(|\tilde{p}_M(\mathbf{z}) - q(\mathbf{z})|)}{a}, \tag{2.28}$$

CHAPTER 2. SIGNATURES OF A QUANTUM ADVANTAGE IN DRIVEN
QUANTUM SYSTEMS

Here, the distribution and the expectation value are computed over $\mathbf{z} \in \mathcal{Z}$. Note that $\mathbb{E}_{\mathbf{z}}(|\tilde{p}_M(\mathbf{z}) - q(\mathbf{z})|) \leq \beta/N$ is given by the additive error defined in Eq. (3) in the main text. By setting $a = \beta/N\zeta$ for some small $\zeta > 0$, we get

$$\Pr_{\mathbf{z}} \left(|\tilde{p}_M(\mathbf{z}) - q(\mathbf{z})| \geq \frac{\beta}{N\zeta} \right) \leq \zeta \quad (2.29)$$

or equivalently

$$\Pr_{\mathbf{z}} \left(|\tilde{p}_M(\mathbf{z}) - q(\mathbf{z})| < \frac{\beta}{N\zeta} \right) > 1 - \zeta. \quad (2.30)$$

By substituting $|\tilde{p}_M(\mathbf{z}) - q(\mathbf{z})|$ from Eq. (2.22), we get

$$\Pr_{\mathbf{z}} \left(|\tilde{p}_M(\mathbf{z}) - \tilde{q}(\mathbf{z})| < \frac{\tilde{p}_M(\mathbf{z})}{\text{Poly}(L)} + \frac{\beta}{N\zeta} \left(1 + \frac{1}{\text{Poly}(L)} \right) \right) > 1 - \zeta. \quad (2.31)$$

Theorem 2 in the main text (the anti-concentration condition) imply that $\{\tilde{p}_M(z)\}$ follows the Porter-Thomas distribution, specially that $1/N < \tilde{p}_M(\mathbf{z})$ for at least $1/e$ fraction of the unitary matrices in $\{\hat{U}_{COE}\}$. Hence, we can rewrite Eq. (2.31) as

$$\Pr_{\mathbf{y}} \left\{ |\tilde{p}_M(\mathbf{z}) - \tilde{q}(\mathbf{z})| < \tilde{p}_M(\mathbf{z}) \left[\frac{1}{\text{Poly}(L)} + \frac{\beta}{\zeta} \left(1 + \frac{1}{\text{Poly}(L)} \right) \right] \right\} > 1/e - \zeta. \quad (2.32)$$

Here, the distribution is over all $\mathbf{z} \in \mathcal{Z}$ and all unitary matrices in $\{\hat{U}_{COE}\}$. To understand the right hand side of the equation, let $P \cap Q$ be the intersection between the set P of probabilities that anticoncentrate and the set Q of probabilities that satisfy the Markov's inequality. Since $\Pr(P \cap Q) = \Pr(P) + \Pr(Q) - \Pr(P \cup Q) \geq \Pr(P) + \Pr(Q) - 1$, $\Pr(P) = 1/e$ and $\Pr(Q) = 1 - \zeta$, it follows that $\Pr(P \cap Q)$ is no less than $1/e + 1 - \zeta - 1 = 1/e - \zeta$.

Following [57, 61], we further set $\beta = 1/(8e)$ and $\zeta = 1/(2e)$, so that

$$\Pr_{\hat{U}_{COE}, \mathbf{z}} \left\{ |\tilde{p}_M(\mathbf{z}) - \tilde{q}(\mathbf{z})| < \left(\frac{1}{4} + o(1) \right) \tilde{p}_M(\mathbf{z}) \right\} > \frac{1}{2e}, \quad (2.33)$$

CHAPTER 2. SIGNATURES OF A QUANTUM ADVANTAGE IN DRIVEN QUANTUM SYSTEMS

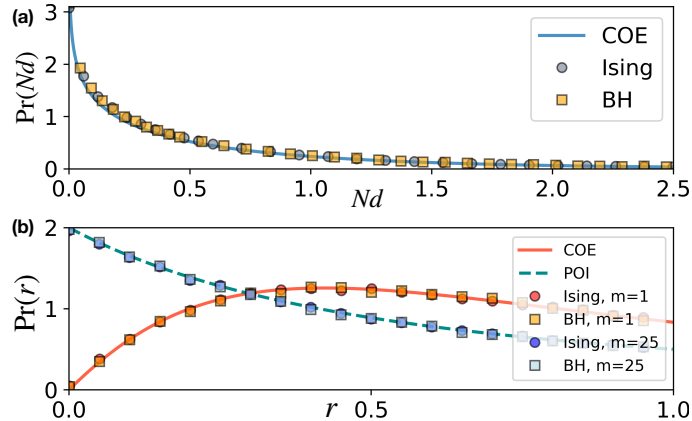


Figure 2.2: (a) The eigenstate distribution $d_n(\mathbf{z})$ for the Ising and the BH models. The blue line is the Bessel function of the second kind predicted by COE. (b) The statistics of level spacings obtained from the Ising and the BH chain at $M = 1, 25$. The blue dashed and the solid lines are the POI and the COE distributions, respectively. Ising and BH parameters: $L = 10$ (with half-filling for the BH model), $W = 1J, B_0 = -\delta B = F_0 = -\delta F = 1.25J, \omega = 8J$, and 500 disorder realizations.

giving an approximation up to multiplicative error $1/4 + o(1)$ for at least $1/(2e)$ instances of the COE matrices $\{\hat{U}_{COE}\}$. If according to the conjecture 1, multiplicatively estimating $1/(2e)$ fraction of the output probabilities from $\{\hat{U}_{COE}\}$ is #P-hard, then the Polynomial Hierarchy collapses. This concludes the proof of Theorem 3.

2.4 Implications of COE hardness for driven thermalized quantum systems

So far, we have demonstrated that sampling from COE dynamics cannot be performed efficiently with classical computers. Here we discuss implications of this result for the periodically driven quantum many-body systems when they thermalize. As the driven thermalized quantum systems and COE are closely related, the absence of efficient classical algorithms to classically sample from COE dynamics

CHAPTER 2. SIGNATURES OF A QUANTUM ADVANTAGE IN DRIVEN QUANTUM SYSTEMS

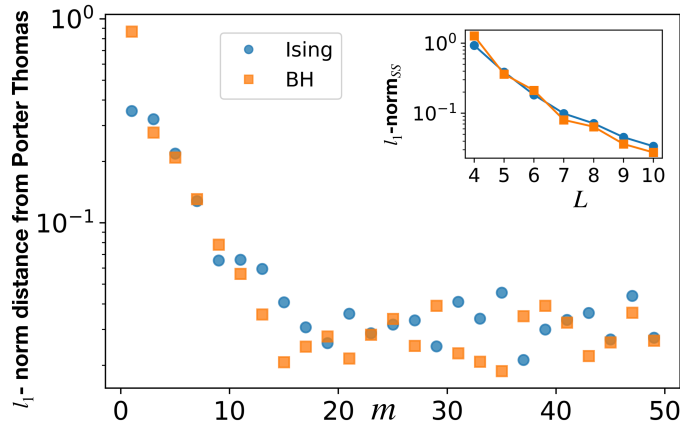


Figure 2.3: The l_1 -norm distance between the output distribution from different quantum systems and the Porter-Thomas distribution at different m . The results from the Ising chain and the BH chain are labeled as circles and squares, respectively. Ising and BH parameters: $L = 10$ (with half-filling for the BH model), $W = 1J$, $B_0 = -\delta B = F_0 = -\delta F = 1.25J$, $\omega = 8J$, and 500 disorder realizations. The inset shows the plot of l_1 -norm distance in the long time limit as a function of L .

suggests the possibility that the same result also holds for the generic thermalized driven quantum systems. We note that this suggestion is plausible only thanks to the external periodic drive boosting the level of randomness [135, 136].

To see why this is possible, we first consider how random matrix theory can be applied to thermalization in undriven isolated quantum systems. Eigenstate thermalization hypothesis (ETH) states that, given an initial state $|\psi_0\rangle$ corresponding to $\bar{E} = \langle\psi_0|\hat{H}_0|\psi_0\rangle$ and $\Delta E = \sqrt{\langle\psi_0|\hat{H}_0^2|\psi_0\rangle - |\langle\psi_0|\hat{H}_0|\psi_0\rangle|^2}$, an expectation value of any generic observable can be calculated with the microcanonical ensemble associated with the energy $\bar{E} \pm \Delta E$. In the thermodynamic limit, this is equivalent to the canonical ensemble with a finite temperature $T = \bar{E}/k_B$. One way to explain the origin of ETH is through the use of the random matrix theory. In this undriven case, accurate descriptions of the systems using random matrix theory is in general only possible over small energy windows far from the energy-spectrum edges. In this

CHAPTER 2. SIGNATURES OF A QUANTUM ADVANTAGE IN DRIVEN QUANTUM SYSTEMS

small energy window, the eigenstates of an undriven thermalized Hamiltonian \hat{H}_0 can be seen as eigenstates of a random matrix when expressed in a generic basis (e.g., computational basis). However, if one analyses the entire energy spectrum, the local structure of typically encountered in static Hamiltonians \hat{H}_0 emerges and random matrix theory fails to capture it.

This is not the case for driven thermalized systems where the system continues to absorb energy from the external drive, leading to $\Delta E \rightarrow \infty$. Here the random matrix theory can be accurately applied to the entire \hat{U}_F spectrum. That is, the eigenstates of \hat{U}_F are expected to be random only now on the entire energy spectrum. A more detailed analysis of \hat{H}_F using Magnus expansion shows that the presence of low-frequency driving allows to generate effective infinite-range multi-body interactions [120, 137]. Therefore lifting most of the constraints imposed by the limited local few-body interactions generally encountered in physical systems. Furthermore, under the condition that COE and the driven thermalized systems share the same statistical distributions, the anti-concentration result (Theorem 2) is readily applicable to the driven thermalized quantum systems.

Nevertheless, we note here that one should not interpret our results as a formal proof of a sampling quantum advantage in the generic driven thermalized quantum systems, but rather as an indication to support the statement. Lastly, our discussion here only applies to the periodically driven systems when they *already* thermalize. There are other phases and regimes such as a many-body localized phase [138] and a prethermalized regime [139] which we will discuss their complexities later on in Chapter 3.

2.4.1 Example of driven thermalized many-body systems

We give two specific examples of driven systems that display statistical properties consistent with the COE and are able to reach the Porter-Thomas distribution with a polynomial number of cycles, hence partially support our suggestion of a sampling quantum advantage. For both cases, the modulation is $f(t) = \cos(\omega t)$, where ω is the driving frequency and an initial state is a product state.

(i) 1D Ising chain: We consider an Ising chain described by the Hamiltonian $\hat{H}_0^{\text{ISING}} = \sum_{i=1}^L h_i \hat{\sigma}_i^z + J \sum_{i=1}^{L-1} \hat{\sigma}_i^z \hat{\sigma}_{i+1}^z + B_0 \sum_{i=1}^L \hat{\sigma}_i^x$, where $h_i \in [-W/2, W/2]$ is a local disorder on site i with the disorder strength W , $\hat{\sigma}_i^z$ (and $\hat{\sigma}_i^x$) is the Z - (and X -) Pauli spin operator acting on site i , J is the interaction strength and B_0 is the amplitude of the static part of the magnetic field along X . The drive is a global fluctuation in the magnetic field $\hat{H}_d^{\text{ISING}} = \delta B \sum_{i=1}^L \hat{\sigma}_i^x$, where δB is the fluctuation in the magnetic field along X . Similar models have been implemented in various quantum platforms, including trapped ions [123] and superconducting circuits [124].

(ii) 1D Bose-Hubbard model: We consider the BH model described by the Hamiltonian $\hat{H}_0^{\text{BH}} = \sum_{i=1}^L (h_i \hat{a}_i^\dagger \hat{a}_i + \frac{U}{2} \hat{a}_i^\dagger \hat{a}_i^\dagger \hat{a}_i \hat{a}_i) + \sum_{i=1}^{L-1} F_0 (\hat{a}_i^\dagger \hat{a}_{i+1} + \text{H.c.})$, where \hat{a}_i (\hat{a}_i^\dagger) is a bosonic annihilation (creation) operator at site i , U is the on-site interaction, h_i is the local disorder as defined above, and F_0 is the hopping amplitude of the static part. The drive modulates the hopping amplitudes $\hat{H}_d^{\text{BH}} = \delta F \sum_{i=1}^{L-1} (\hat{a}_i^\dagger \hat{a}_{i+1} + \text{H.c.})$. Similar models have been implemented in superconducting circuits [113] and cold atoms [37, 38, 122].

The distribution of $d_n(\mathbf{z})$ from both models are depicted in Fig. 4.1(a), showing

CHAPTER 2. SIGNATURES OF A QUANTUM ADVANTAGE IN DRIVEN QUANTUM SYSTEMS

an agreement with the Bessel function as predicted by COE. The level statistics at $M = 1$ and $M = 25$ are depicted in Fig. 4.1(b), showing an agreement with the COE and the POI distribution, respectively. The driving frequency and the disorder strength are tuned to ensure the observation of the thermalized phase and prevent many-body localization [120, 140].

Fig. 4.2 shows the l_1 -norm distance between $\Pr(p)$ and the Porter-Thomas distribution at different m for the Ising and the BH models. It can be seen that, in all cases, the system reaches the Porter-Thomas distribution after multiple driving cycles. The l_1 -norm distance in the long-time limit is decaying towards zero as the size of the system increases. Therefore, the anti-concentration condition is satisfied.

2.4.2 Undriven thermalized many-body systems

In absence of the drive, a similar analysis can be performed for the infinite-time unitary evolution corresponding to generic instances of the undriven thermalized phase in both models. In this case, $d_n(\mathbf{z})$ does not follow the Bessel function of the second kind and the output distribution never reaches the Porter-Thomas distribution. This is consequence of the energy conservation and the structure imposed by the local interactions, highlighting the key role played by the drive.

In this section, we analyze the long-time unitary evolution for undriven systems in the thermalized phase. The results presented here highlight the key role played by the drive in generating the randomness required for the above quantum supremacy proof. In particular, we show that for typical undriven physical systems with local constraints (e.g. finite-range interactions) and conserved energy, the output

CHAPTER 2. SIGNATURES OF A QUANTUM ADVANTAGE IN DRIVEN QUANTUM SYSTEMS

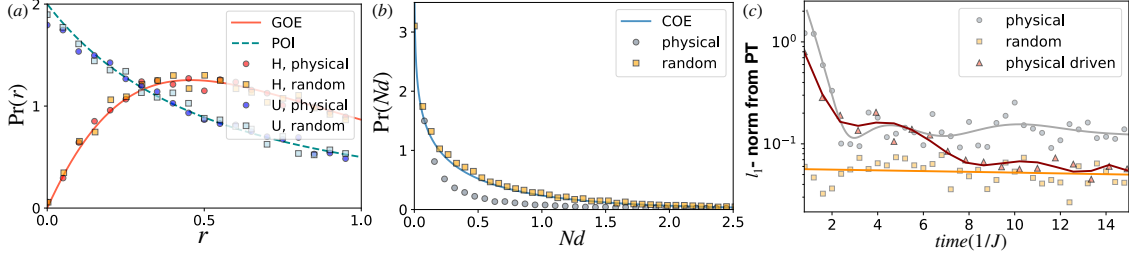


Figure 2.4: **Undriven thermalized Ising models versus the GOE:** (a) Level-spacing statistic of an ensemble $\{\hat{H}\}$ and their corresponding long-time evolution operator \hat{U} obtained from the physical Ising system (circle) and the GOE (square). The blue dashed and the orange solid lines are theoretical predictions for the POI and the GOE distributions, respectively. (b) The eigenstate distribution $d_n(\mathbf{z})$ [see Eq. (5) of the main text] with the GOE prediction (solid line). (c) The l_1 -norm distance between the output distribution and the PT distribution as a function of time. The driven case studied in the main text is presented for comparison. The parameters used are: $L = 9$, $W = 1.5J$, $B_0 = 1.25J$ ($\delta B = -1.25J$, $\omega = 8J$ for the driven case) and 500 disorder realizations.

distribution never coincides with the PT distribution.

We emphasize that this is a consequence of the inability of the random matrix theory to accurately describe the full spectral range of undriven thermalized many-body systems. Indeed, it has been shown that for undriven many-body systems which thermalizes (to a finite temperature), the statistics of the Hamiltonian resembles the statistics of the Gaussian orthogonal ensemble (GOE) [119]. However, it is implicit that an accurate match only applies over a small energy window (usually far from the edges of the spectrum). If one zooms in this small energy window, the Hamiltonian looks random, but if one consider the full spectrum, the local structure of the Hamiltonian appears and the random matrix theory fails at capturing it.

To see this, we numerically simulate the undriven Ising Hamiltonian, $\hat{H}_0 = \sum_{i=1}^L h_i \hat{\sigma}_i^z + J \sum_{i=1}^{L-1} \hat{\sigma}_i^z \hat{\sigma}_{i+1}^z + B_0 \sum_{i=1}^L \hat{\sigma}_i^x$, where $h_i \in [-W/2, W/2]$ is a local disorder, W is the disorder strength, B_0 is the static global magnetic field along X and J is

CHAPTER 2. SIGNATURES OF A QUANTUM ADVANTAGE IN DRIVEN
QUANTUM SYSTEMS

the interaction strength. This Hamiltonian is in fact the average Hamiltonian of the driven Ising Hamiltonian used in the main text. In comparison, we also simulate the quantum evolution under an ensemble $\{\hat{H}_{\text{GOE}}\}$ of synthetic Hamiltonians that are uniformly drawn from the GOE (i.e. without any local constraints).

Fig.2.4 (a) shows the level-spacing statistics of $\{\hat{H}_0\}$ (obtained over 500 disorder realizations), $\{\hat{H}_{\text{GOE}}\}$ (obtained over 500 random instances) and their corresponding long-time unitary operators $\hat{U} = \lim_{t \rightarrow \infty} e^{-it\hat{H}}$. We see that the level statistic of the physical Hamiltonian (and its long-time evolution) is indistinguishable from the GOE. However, the discrepancy between the physical and synthetic (GOE) realizations becomes apparent when looking at the eigenstate statistics as shown in Fig.2.4 (b). While the distribution of $d_n(\mathbf{z})$ from the GOE is in a good agreement with the Bessel function of the second kind, the physical undriven system fails to meet the theoretical prediction. This is in contrast to the driven case as observed before in Fig 4.2 (and also plotted in Fig.2.4 for comparison). More importantly in the context of this work, a key difference between the physical Hamiltonian and the random matrix theory prediction can be seen by comparing the distribution of the output states after some time evolution. In Fig.2.4 (c), we show that the Porter-Thomas distribution is never achieved with the physical systems while it is for the synthetic realizations as well as for the driven case. These results underline the gap between physical Hamiltonians and true random matrices and more importantly, they highlights the important role of the drive in bridging that gap.

2.5 Conclusion and outlook

Analog quantum simulators realizing quantum many-body systems have generated quantum dynamics beyond the reach of existing classical numerical methods for some time. However, such dynamics has not been theoretically proven to be hard to compute by a classical computer. We have taken the first step into proving that in the particular case of driven many-body systems, when they thermalize, sampling from their output distribution cannot be efficiently performed on a classical computer. Using complexity theory arguments, we provide strong analytical evidence of the computational hardness of sampling from the COE dynamics. As a consequence, the same complexity result might be expected for the driven thermalized quantum systems thanks to their closed link with COE. We further argue that this possibility is much more likely to happen in the driven case compared to the undriven one as more randomness added into the systems due to the external drive. We provide numerical results showing that COE statistics and reaching the Porter-Thomas distribution with polynomially many cycles can be obtained from driven quantum Ising and BH models for realistic parameters.

All together, our results pave the way to realise a sampling quantum advantage of analog quantum simulators with currently available platforms, including trapped ions and cold atoms. In the future, the next important step is to analyze complexity of a specific model in driven thermalization, such as driven Ising spin chains, and demonstrate a sampling quantum advantage directly from the physical system. In addition, it would be interesting to see at what extent one can probe the complexity

CHAPTER 2. SIGNATURES OF A QUANTUM ADVANTAGE IN DRIVEN QUANTUM SYSTEMS

of physical systems from their respective matrix ensembles. For example, whether this approach can be extended to other classes of quantum many-body systems such as those with gauge fields or frustrated systems.

Chapter 3

Probing phase transitions with quantum advantage signatures

This chapter summarizes the material published in

- S. Thanasilp, J. Tangpanitanon, MA. Lemonde, N. Dangiam, DG. Angelakis, “Quantum supremacy and quantum phase transitions”, *Physical Review B* 103 (16), 165132, (2021).

3.1 Introduction

Recent experimental developments [22, 64, 112, 113, 141] have made the first steps toward demonstrating the ability of noisy intermediate-scale quantum (NISQ) devices [19] to perform certain computational tasks intractable to classical computers [50, 56–58, 60, 62–64, 116, 117, 142, 143]. Early proposals to demonstrate this quantum primacy include sampling from random superconducting circuits [57, 58] and boson sampling on photonic platforms [62–64]. Despite being an important milestone for quantum computation in the NISQ era, extending the proposed computational tasks to address real-world problems remains an open challenge. This is particularly true in the context of sampling from quantum random circuits where

CHAPTER 3. PROBING PHASE TRANSITIONS WITH QUANTUM ADVANTAGE SIGNATURES

any practical applications remains limited [144–146]. For example, the randomness required in such circuits makes them in principle unsuitable for medium- to large-scale variational quantum algorithms [94], thus greatly limiting their applications in near-term quantum chemistry [33, 147], material science [148, 149] and quantum machine learning [150].

As described in details in Chapter 2, the computational task of sampling from generic closed periodically-driven quantum many-body systems has been proposed recently to demonstrate quantum primacy [151]. This opens the road for a plethora of analog based quantum simulators on periodically driven cold atoms and ions to be used for such tasks [9, 10]. The computational complexity of sampling from such dynamics is intimately related to the ability of the closed system to thermalize under the combined influence of interactions and the external drive. Once thermalised, the associated temperature is effectively infinite resulting in a quantum evolution capable of uniformly exploring the Hilbert space [120, 139, 152, 153]. This is in contrast with the driven many-body localized (MBL) phase where the presence of disorder prevents the system to thermalize and limits the quantum evolution to a restricted portion of the Hilbert space [138, 152–156]. Efficient theoretical representations exploiting this fact suggest that the sampling from MBL dynamics is tractable to classical computers [157–159]. Therefore, the experiment we proposed in Chapter 2 to achieve quantum primacy can be interpreted as a protocol to probe how much of the Hilbert space has been explored under specific driven quantum dynamics. This ability of tuning in and out of the chaotic evolution characterizing the thermal phase, by controlling the level of disorder, has already been exploited

CHAPTER 3. PROBING PHASE TRANSITIONS WITH QUANTUM ADVANTAGE SIGNATURES

as a potential application in the context of quantum machine learning [160] and we describe this in more details in Chapter 4.

In this chapter, we describe how the quantum primacy experiment proposed in the previous chapter can be extended to probe the quantum phases of periodically-driven disordered many-body systems. More specifically, we propose utilising key quantum primacy signatures as order parameters, such as the Kullback-Leibler divergence (KLD) [161] between the output probability distribution and the Porter-Thomas (PT) distribution [162]. The one to one matching in the behaviour of these two distributions is a strong indication that the system is capable of uniformly exploring its Hilbert space [57] and thus intimately related to the computational complexity of the sampling task ¹. Therefore, such order parameter offers additional insights into the dynamics compared to the measure of the population imbalance commonly used in experiments [138, 165–167]. In addition, the measurement of the KLD from the PT distribution, performed only in the computational basis, should also be experimentally more accessible compared to probing the level-statistics [163], which is already challenging for undriven systems [39] with no known efficient extension to the driven cases. We show that probing the KLD from the PT distribution allows to distinguish the driven thermalized phase from the driven MBL phase as well as from the Floquet prethermalized regime [37, 137, 139]. The latter corresponds to the scenario where the drive frequency roughly exceeds the single-particle energy

¹This is similar to the growth of the bipartite entanglement entropy in closed systems which also captures the increase in the capacity of the system to explore its Hilbert space [163]. While a large entanglement entropy implies a classically intractable matrix product state (MPS) representation [164], a vanishing KLD from the PT distribution has been shown to be a key condition to prove that any classical approach is intractable [57, 151].

CHAPTER 3. PROBING PHASE TRANSITIONS WITH QUANTUM
ADVANTAGE SIGNATURES

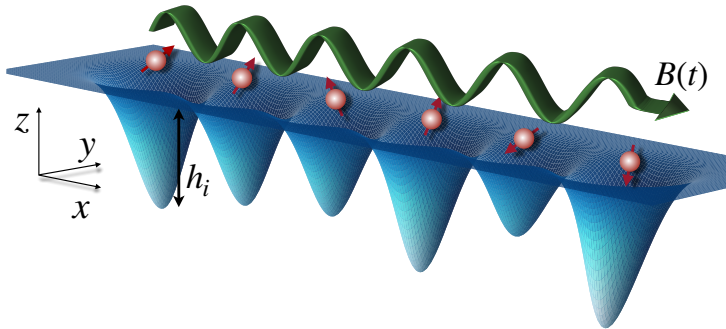


Figure 3.1: Schematic of a periodically driven quantum Ising chain with nearest-neighbor interactions and disordered onsite energies.

(without exceeding the entire spectrum range of the many-body Hamiltonian), leading to long-lived prethermalization dynamics [137]. Although we focus on the KLD between the output and the PT distributions as it is a straightforward quantum primacy signature, we emphasize that our idea could be extended to any suitable metrics associated with the computational complexity of sampling from the different phases. For example as we discuss in Section 3.4.5, the entanglement entropy over multiple sub-systems can also be used as an alternative primacy signature for probing the phase diagram.

As a specific model, we focus on an isolated Ising spin chain with nearest-neighbour interactions, disordered on-site energies and a periodically time-varying global magnetic field. We analyse the dynamics using the Floquet formalism which allows to highlight the role played by the effective long-range multi-body interactions generated by the drive in the context of quantum primacy. Our work thus proposes a direct application of a potential quantum primacy experiment and present additional physical intuitions about the origin of the computational complexity associated with sampling from a driven thermalized quantum system.

3.2 Quantum phases in driven disordered Ising spin chains

3.2.1 Model

The particular model we consider is sketched in Fig. 3.1 and consists of a periodically-driven Ising chain with disordered onsite energies. The corresponding Hamiltonian reads $\hat{H}(t) = \hat{H}_0 + f(t)\hat{H}_d$, where

$$\hat{H}_0 = \sum_{i=1}^L h_i \hat{\sigma}_i^z + B_0 \sum_{i=1}^L \hat{\sigma}_i^x + J \sum_{i=1}^{L-1} \hat{\sigma}_i^z \hat{\sigma}_{i+1}^z, \quad (3.1)$$

$$\hat{H}_d = \sum_{i=1}^L \hat{\sigma}_i^x, \quad (3.2)$$

with $f(t) = \delta B \cos(\omega t)$. Here $\hat{\sigma}_i^x$ ($\hat{\sigma}_i^z$) is the X (Z) Pauli operator acting on the i^{th} spin of an open chain of L total sites, J represents the nearest-neighbour interaction strength and $B(t) = B_0 + \delta B \cos(\omega t)$ represents a periodic magnetic field along the x -axis of frequency $\omega \equiv 2\pi/T$. We consider disordered static magnetic fields along the z -axis with strengths $h_i \in [-W/2, W/2]$ being drawn from a uniform distribution ranging from $-W/2$ to $W/2$. Importantly, the Hamiltonian at different times t_1 and $t_2 \neq t_1 + nT$ with $n \in \mathbb{Z}$ do not commute, i.e. $[\hat{H}(t_1), \hat{H}(t_2)] \neq 0$, and the contribution from the drive averages to zero over a period, i.e. $\frac{1}{T} \int_0^T \hat{H}_d(t) dt = 0$.

The time evolution over a driving period is described by the unitary operator

$$\hat{U}_F = \hat{\mathcal{T}} \exp \left[-i \int_0^T \hat{H}(t) dt \right] \equiv \exp \left[-i \hat{H}_F T \right], \quad (3.3)$$

where $\hat{\mathcal{T}}$ is the time-ordering operator. The time-independent Hamiltonian \hat{H}_F is known as the Floquet Hamiltonian and fully describes the dynamics at stroboscopic times $t_n = nT$. While a specific form of the Ising model is studied in this work, the

CHAPTER 3. PROBING PHASE TRANSITIONS WITH QUANTUM ADVANTAGE SIGNATURES

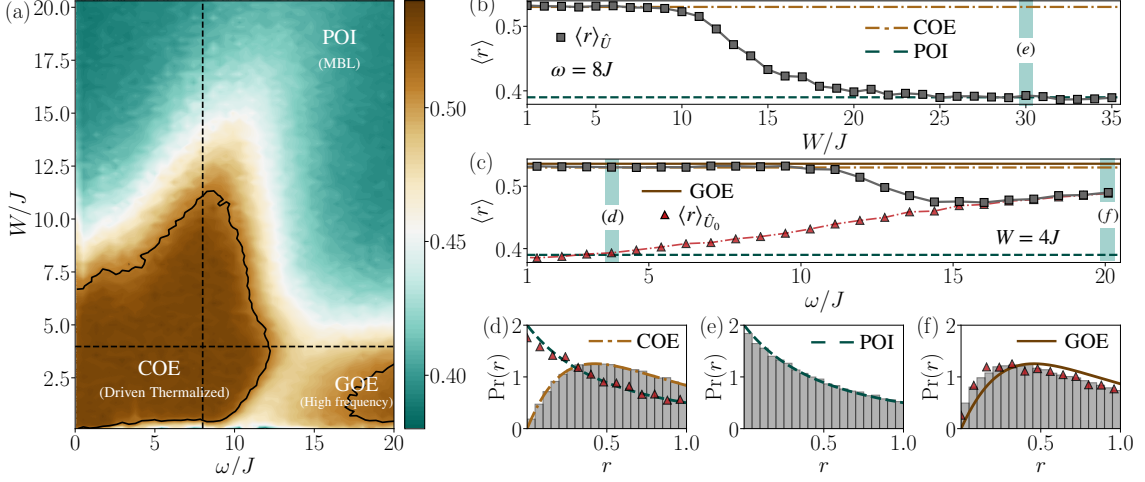


Figure 3.2: **Phase diagram and level statistics of the driven disordered Ising spin chain.** (a) Average level spacing $\langle r \rangle_{\hat{U}_F}$ of the full unitary \hat{U}_F as a function of the disorder strength W/J and the driving frequency ω/J for $L = 9$ and $B_0 = -\delta B = 1.25J$. (b) A cut along the frequency $\omega = 8J$ [vertical dashed line in (a)] shows $\langle r \rangle_{\hat{U}_F}$ as a function of W/J and captures the phase transition from driven thermalized to the driven MBL. (c) A cut along $W = 4J$ [horizontal dashed line in (a)] captures the transition as a function of ω/J from the driven thermalized phase to the prethermalized regime and beyond. The red triangles represent the mean value $\langle r \rangle_{\hat{U}_0}$ computed only considering the evolution under \hat{H}_0 for a time $t = 2\pi/\omega$. (d)-(f) Full distribution $\text{Pr}(r)$ for the driven thermalized phase ($W = 4J, \omega = 4.2J$) following the COE, MBL phase ($W = 30J, \omega = 8J$) following POI and the high frequency regime ($W = 4J, \omega = 20.1J$) converging towards the GOE respectively. In (d), the statistics of \hat{U}_F and \hat{U}_0 drastically differ while they converge in (f); contrasting the importance of the the multi-body long-range interaction induced by the drive at different ω . Each data point results from 100 disorder realizations.

results obtained can be generalized for other driven many-body systems such as Bose-Hubbard model or different variations of the Ising spin model. All together, such driven systems have been experimentally implemented in various quantum platforms including superconducting circuits [113], cold atoms [10, 37, 38] and trapped ions [9].

3.2.2 Phases and level-statistics

Depending on the disorder strength W/J and driving frequency ω/J , the system can be in distinct regimes [138, 139]. At low disorder strengths, the system thermalizes under its own dynamics if given enough time and follows the eigenstate thermalization hypothesis [139]. Under the assumption that the system can be considered closed over the entire process, the constant energy input provided by the drive leads to an effective temperature that is infinite [120, 139, 152, 153]. The time-scale over which this thermalization process takes place strongly depends on the drive frequency [137]. For low-frequency drives, the system can efficiently respond and rapidly reaches this infinite-temperature limit corresponding to what is known as the *driven thermalized phase* [120, 139, 152, 153]. In the case where the driving frequency roughly exceeds the single-particle energy, however, the time required for thermalizing can be greatly extended leading to a long-lived *prethermalization regime* [37, 137, 139]. Further increasing the drive frequency beyond all relevant energy scales results in the inability for the system to absorb the quantized energy from the drive and the failure to thermalize to infinite temperature. Finally, in presence of large disorders, the system fails to thermalize at any time and is said to be in the *driven MBL phase* [152–156]. The two phases and the high-frequency limit are depicted in Fig. 4.1 (a).

One of the standard approach to distinguish the different phases is based on the notion of level statistics of the unitary operator \hat{U}_F [120, 154]. Let $|\phi_n\rangle$ be an eigenstate of the Floquet Hamiltonian with eigenvalue ϵ_n , i.e. $\hat{H}_F|\phi_n\rangle = \epsilon_n|\phi_n\rangle$, it

CHAPTER 3. PROBING PHASE TRANSITIONS WITH QUANTUM
ADVANTAGE SIGNATURES

follows that

$$\hat{U}_F = \sum_n e^{i\theta_n} |\phi_n\rangle\langle\phi_n|, \quad (3.4)$$

where $\theta_n = \epsilon_n T$ modulo 2π . The level statistics is defined as the normalized distribution $\text{Pr}(r)$ of the level spacing

$$r = \frac{\min(\delta_n, \delta_{n+1})}{\max(\delta_n, \delta_{n+1})}, \quad (3.5)$$

with $\delta_n = \theta_{n+1} - \theta_n$ and $\theta_{n+1} \geq \theta_n$.

In the driven thermalized phase, the level statistics of \hat{U}_F coincides with the circular orthogonal ensemble (COE) statistics, given by

$$\text{Pr}_{\text{COE}}(r) = \frac{2}{3} \left[\frac{\sin\left(\frac{2\pi r}{r+1}\right)}{2\pi r^2} + \frac{1}{(r+1)^2} + \frac{\sin\left(\frac{2\pi}{r+1}\right)}{2\pi} - \frac{\cos\left(\frac{2\pi}{r+1}\right)}{r+1} - \frac{\cos\left(\frac{2\pi r}{r+1}\right)}{r(r+1)} \right]. \quad (3.6)$$

This result means that, from a statistical point of view, a generic \hat{U}_F associated with this phase is equivalent to a unitary matrix randomly sampled from the complete ensemble of unitaries that conserves the time-reversal symmetry [130]. The fact that $\text{Pr}_{\text{COE}}(0) = 0$ indicates phase repulsion and thus correlations between the different eigenstates. A COE evolution in low-frequency driven systems is an indicator of thermalization to infinite temperatures [120].

The scenario is completely different for systems in the driven MBL phase where the level statistics is described by a Poisson distribution [156],

$$\text{Pr}_{\text{POI}}(r) = \frac{2}{(1+r)^2}. \quad (3.7)$$

This time, $r = 0$ corresponds to the peak of $\text{Pr}_{\text{POI}}(r)$ indicating a high level of degeneracies in the MBL phase. This absence of phase repulsion is intuitive as spatially distant localized eigenstates are uncorrelated.

CHAPTER 3. PROBING PHASE TRANSITIONS WITH QUANTUM ADVANTAGE SIGNATURES

In the limit where the driving frequency exceeds all relevant energy scales of the system, a slightly different interpretation of the level statistics is required. This comes as all phases $\theta_n = \epsilon_n T < 2\pi$ (for $\omega > \max[\epsilon_n]$) become strictly linearly related to the eigenenergies of \hat{H}_F so that the statistics of \hat{U}_F must coincide with the statistics of \hat{H}_F . In addition, for $\omega \rightarrow \infty$, $\hat{H}_F \rightarrow \hat{H}_0$ (see section 3.4.4) and one should expect to recover the statistics of the undriven Ising model as the frequency increases. Similar to the driven case, \hat{H}_0 has two distinct phases: the MBL phase for large disorder and the finite-temperature thermalized phase for weak disorder. While the undriven MBL still leads to the Poisson statistics, $\text{Pr}(r)$ of the undriven thermalized phase follows the Gaussian orthogonal ensemble (GOE),

$$\text{Pr}_{\text{GOE}}(r) = \frac{27}{4} \frac{r + r^2}{(1 + r + r^2)^{5/2}}, \quad (3.8)$$

which corresponds to the ensemble of matrices with independent normal random variables as elements and subjected to the orthogonality constraint [130]. We note that in the thermodynamics limit, the energy spectrum of the system becomes infinite so that the driving frequency required to reach this limit also becomes infinite.

In Fig. 4.1, we show the level statistics as a function of the drive frequency ω/J and the disorder strength W/J for an Ising chain of $L = 9$. The results are obtained by exactly diagonalizing \hat{U}_F of Eq. Equation 3.3 over 100 disorder realizations for each data point. In panels (a)-(c), we show the mean value of level spacing $\langle r \rangle_{\hat{U}_F}$ as a metric to characterize the different phases and compare it to the values obtained in the COE ($\langle r \rangle_{\text{COE}} \approx 0.527$), the POI ($\langle r \rangle_{\text{POI}} \approx 0.386$) and

the GOE ($\langle r \rangle_{\text{GOE}} \approx 0.536$). We distinguish the distinct regimes of the driven dynamics and explicitly show the transition from driven thermalized to driven MBL phases as we increase W/J with fixed ω/J in panel (b) and from driven thermalized phase to prethermalization regime and beyond as we increase ω/J with fixed W/J in panel (c). In panels (d)-(f), we show $\text{Pr}(r)$ obtained from \hat{U}_F in these three regimes where it coincides with their respective statistical ensembles. Finally, we also compute the level statistics of the unitary operator produced by only considering the undriven Hamiltonian \hat{H}_0 , i.e. $\hat{U}_0 = \exp -i\hat{H}_0 T$, and compare it to the exact results corresponding to the same frequency $\omega = 2\pi/T$. As expected, $\langle r \rangle_{\hat{U}_F}$ and $\langle r \rangle_{\hat{U}_0}$ converge as ω/J increases. The intermediate frequency range for which $\langle r \rangle_{\hat{U}_F}$ diverges from COE but does not coincide with the statistic of \hat{U}_0 indicates the presence of long-lived prethermalization dynamics. At higher frequencies, where $\langle r \rangle_{\hat{U}_F}$ and $\langle r \rangle_{\hat{U}_0}$ match perfectly, the dynamics is expected to never lead to infinite-temperature thermalization [120]. We note that in absence of disorder, $W \rightarrow 0$, the statistics of \hat{U}_F differs from the COE for a wide range of frequencies. This is reminiscent of the fact that the dynamics described by Eq. Equation 3.1 with $W = 0$ is equivalent to a non-interacting fermionic system [168].

3.3 Complexity of sampling from different phases

In this section, we discuss the computational complexity of sampling from quantum states evolving under the dynamics associated with the different regimes discussed above. We begin by briefly reviewing the formal evidence presented in Chapter 2 which suggests that such a task is classically intractable in the driven

thermalized phase following the COE. We focus on the convergence of the distribution of the output probabilities towards the PT distribution as a key quantum primacy signature which we contrast in the MBL phase and the high frequency regime.

3.3.1 Quantum primacy in the driven thermalized phase

We define the exact probability of measuring the basis state $|\mathbf{z}\rangle = \otimes_i^L |z_i\rangle$ after m driving cycles as $p_m(\mathbf{z}) \equiv |\langle \mathbf{z} | \psi_m \rangle|^2$, where $\hat{\sigma}_i^z |z_i\rangle = z_i |z_i\rangle$ is the eigenstate of the single-qubit Pauli Z matrix acting on site i and where $|\psi_m\rangle = \hat{U}_F^m |\psi_0\rangle$. The initial state $|\psi_0\rangle$ is assumed to be a product state. The computational task considered here is *the sampling of output bitstrings \mathbf{z} from $p_m(\mathbf{z})$ up to (realistic) additive errors*. More precisely, it requires to produce a sampler \mathcal{C} capable of providing bitstrings from a distribution $q(\mathbf{z})$ that is *additively closed* to the exact distribution $p_m(\mathbf{z})$, i.e.

$$\sum_{\mathbf{z}} |p_m(\mathbf{z}) - q(\mathbf{z})| \leq \beta, \quad (3.9)$$

where β is a small positive constant. The sampler \mathcal{C} can be either constructed by a quantum or a classical device. Quantum-mechanically, this can be achieved by performing projective measurements on an analog quantum simulator capable of reproducing the exact driven Hamiltonian. The difference between $q(\mathbf{z})$ and $p_m(\mathbf{z})$ can be kept small if the noise from the environment and imperfections in the controls remains sufficiently low.

Producing this sampler \mathcal{C} with a classical computer is, however, not as natural and analytical evidence presented in Chapter 2 suggests that, given that \hat{U}_F follows the COE statistics, the sampling task is expected to become classically intractable as the system size increases. One of the key features that ensures this computational

CHAPTER 3. PROBING PHASE TRANSITIONS WITH QUANTUM
ADVANTAGE SIGNATURES

complexity is the fact that the associated quantum dynamics anti-concentrates [127]. Mathematically, this means that the distribution of the output probabilities $p_m(\mathbf{z})$ respects the condition

$$\Pr(p_m(\mathbf{z}) > \delta/N) \geq \gamma, \quad (3.10)$$

for all possible \mathbf{z} . Here δ and γ are positive constants, $N = 2^L$ is the dimension of the Hilbert space, and the distribution is computed over all experimentally implementable unitaries $\{\hat{U}_F\}$. Equation Equation 3.10 ensures that most of the basis states have non-zero probability of being measured. Following the anti-concentration condition, one can show that if \hat{U}_F follows the COE, the existence of any efficient classical sampler \mathcal{C} would imply the collapse of the complexity hierarchy to the third level [58].

In the case where the dynamics is such that the output state $|\psi_m\rangle$ has an equal probability of being anywhere in the Hilbert space, its output distribution $\Pr(p_m(\mathbf{z}))$ follows the PT distribution [57],

$$\text{PT}(p) = Ne^{-Np} \quad \text{for} \quad N \gg 1, \quad (3.11)$$

and the dynamics satisfies the anti-concentration condition Eq. Equation 3.10 with $\delta = 1$ and $\gamma = 1/e$. As a consequence, the convergence of the output distribution toward the PT distribution is a key signature of quantum primacy [57, 113, 151]. The difference between these two distributions can be measured by the KLD [161], defined as ($p = p_m(\mathbf{z})$ for readability)

$$\text{KLD}(\Pr(p) \parallel \text{PT}(p)) \equiv \sum_p \Pr(p) \log \left(\frac{\Pr(p)}{\text{PT}(p)} \right) \geq 0. \quad (3.12)$$

The KLD is zero only when $\Pr(p) = \text{PT}(p)$ for all p .

CHAPTER 3. PROBING PHASE TRANSITIONS WITH QUANTUM
ADVANTAGE SIGNATURES

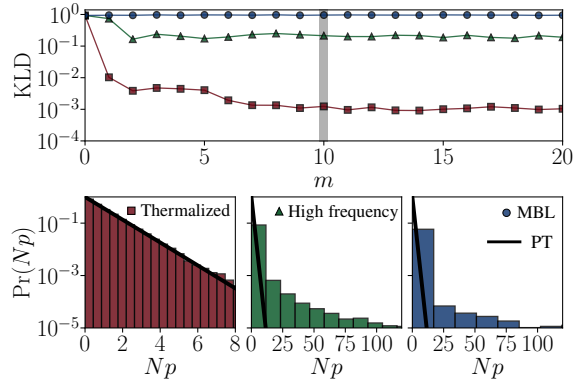


Figure 3.3: **Reaching the PT distribution.** (a) $\text{KLD}(\text{Pr}(p) \parallel \text{PT}(p))$ with $p = p_m(\mathbf{z})$ as a function of the driving cycle m for the driven thermalized phase ($W = 3J, \omega = 8J$; dark red squares), the driven MBL phase ($W = 30J, \omega = 8J$; blue circles) and the high frequency regime ($W = 4J, \omega = 20J$; green triangles). (b)-(d) Output probability distributions $\text{Pr}(Np)$ for $m = 10$ in the three different regimes. (b) $\text{Pr}(Np)$ in the driven thermalized phase ($\omega = 8J$) is in a good agreement with the PT distribution (black line) while it is not in (c) for the high frequency regime and in (d) for the driven MBL phase. The other parameters are $L = 9$ with $N = 2^L$, $B_0 = -\delta B = 1.25J$ and each data points has been computed over 100 disorder realizations.

In Fig. 4.2, we plot the KLD between the output distribution $\text{Pr}(p = p_m(\mathbf{z}))$ after m driving cycles and the PT distribution $\text{PT}(p = p_m(\mathbf{z}))$ for the three regimes of a driven Ising chain with $L = 9$. In panel (a), we show the evolution of the KLD as a function of m and see that only in the driven thermalised phase $\text{Pr}(p)$ reaches the PT distribution after a number of cycles that increases as the driving frequency increases.

3.3.2 Computational complexity of the MBL phase and the high frequency regime

In the MBL phase, only a small fraction of the Hilbert space near the initial state is explored. Consequently, given an initial product state e.g., $|\psi_0\rangle = |0\rangle^{\otimes L}$, only a limited number of output bitstrings can be measured after the quantum

CHAPTER 3. PROBING PHASE TRANSITIONS WITH QUANTUM ADVANTAGE SIGNATURES

evolution and the anti-concentration condition can never be satisfied (see Appendix B for more details). Consequently, the existence of a classical sampler \mathcal{C} capable of providing bitstrings from a distribution additively closed to $p_m(\mathbf{z})$ is not prohibited by the accepted hierarchy of the complexity classes.

The more involved question of whether the simulation of the MBL dynamics is classically intractable or not has already been studied extensively [138, 157–159] and the answer lies in the properties of the bipartite entanglement entropy. For an isolated system described by $|\Psi\rangle$, the bipartite entanglement entropy S_e is obtained by dividing the system into two subsystems \mathcal{S} and \mathcal{B} and calculating the von Neumann entropy of one of the reduced density matrix, i.e. $S_e = -\text{Tr}_{\mathcal{S}}\{\hat{\rho}_{\mathcal{S}} \log_2 \hat{\rho}_{\mathcal{S}}\}$ with $\hat{\rho}_{\mathcal{S}} = \text{Tr}_{\mathcal{B}}\{|\Psi\rangle\langle\Psi|\}$. In the MBL phase, all eigenstates of \hat{U}_F obey the “area law” [138], meaning that S_e is independent of the subsystem size in 1D systems. This property suggests an efficient classical representation using matrix product states (MPS) with low bond dimensions and the use of density matrix renormalization group (DMRG) techniques [159, 169]. Moreover, given an initial product state, the entanglement entropy evolves logarithmically with time [170, 171], allowing efficient and accurate classical simulation of long-time dynamics. Therefore, further supporting that driven MBL dynamics never converges towards the PT distribution which would represent infinite-temperature thermalization and would imply maximal entanglement entropy. In Appendix B, we analytically show that the MBL dynamics can be efficiently approximated with MPS up to additive errors.

The scenario in the high frequency regime where \hat{U}_F tends towards the GOE statistics is very different and many questions remain open. For example, the

CHAPTER 3. PROBING PHASE TRANSITIONS WITH QUANTUM
ADVANTAGE SIGNATURES

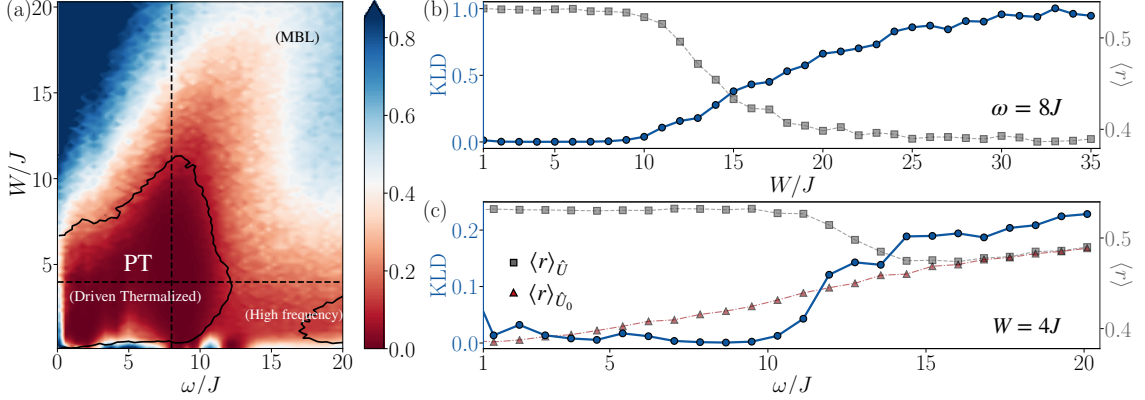


Figure 3.4: **Probing the phase diagram with the $\text{KLD}(\text{Pr}(p) \parallel \text{PT}(p))$.** (a) $\text{KLD}(\text{Pr}(p) \parallel \text{PT}(p))$ with $p = p_m(\mathbf{z})$ after $m = 10$ driving cycles as a function of the disorder strength W/J and the driving frequency ω/J . The solid black line represents the parameters for which $\langle r \rangle_{\hat{U}_F} = 0.51$ as a comparison with Fig. 4.1 (a). (b) A cut along the frequency $\omega = 8J$ (vertical dashed line in (a)) comparing the $\text{KLD}(\text{Pr}(p) \parallel \text{PT}(p))$ (blue dot, left y-axis) with $\langle r \rangle_{\hat{U}_F}$ (gray squares, right y-axis) as a function of W/J along the phase transition from driven thermalized to driven MBL. (c) A cut along $W = 4J$ (horizontal dashed line in (a)) as a function of ω/J demonstrates the transition towards the prethermalization regime. This time, we compare the $\text{KLD}(\text{Pr}(p) \parallel \text{PT}(p))$ with $\langle r \rangle_{\hat{U}_F}$ and $\langle r \rangle_{\hat{U}_0}$ (see Fig. 4.1 (c) and main text). The other parameters are as in Fig. 4.1.

entanglement entropy of the eigenstates of \hat{U}_{GOE} obeys the “volume law” and an initial product state would see its entanglement entropy increase linearly in time [163]. Both properties force an efficient MPS representation to fail. On the other hand, the fact that the output distribution does not follow the PT distribution implies that the system does not uniformly explore the whole Hilbert space and leaves uncertain whether or not the output distribution anti-concentrates [see Eq. Equation 3.10]. The complexity class associated with sampling from a quantum state in the high frequency regime thus remains unclear.

3.4 Quantum phases from primacy signatures: A new order parameter

Now that we have presented the different phases and discussed the computational complexity to sample from their dynamics, we analyse how quantum primacy signatures, here taken to be the KLD to PT, can be directly used to probe the dynamical phase diagram of the driven Ising chain. The motivation is not only to provide an alternative order parameter, compared to the mean level spacing $\langle r \rangle$ and the population imbalance for example, but also to revisit these phase transitions from a computational complexity point of view.

3.4.1 Phase diagram

The protocol consists of initializing the system in a product state $|\psi_0\rangle = |0\rangle^{\otimes L}$, letting it evolve for m driving cycles and compute its output probability distribution $\Pr(p)$ [$p = p_m(\mathbf{z})$]. We repeat the procedure for 100 disorder realizations and average the results. In Fig. 3.4 (a), we construct a “phase diagram” from the KLD of the output distributions to PT as a function of the disorder strength W/J and the drive frequency ω/J . The solid black lines represent the parameter boundaries with $\langle r \rangle_{\hat{U}_F} = 0.51$ as in Fig. 4.1 for easier comparison. From the low-frequency and low-disorder enclosed region corresponding to $\langle r \rangle_{\hat{U}_F} > 0.51$, we see that the convergences of $\Pr(p)$ towards the PT distribution at $m = 10$ coincide with the convergence of the unitary \hat{U}_F towards the COE. The divergence from the PT distribution as $W \rightarrow 0$ is again a consequence of the non interacting nature of the model described by Eq. Equation 3.1 with $W = 0$. The PT is also not reached in

the high-frequency limit where \hat{U}_F does not coincide with the COE. As discussed earlier, the computational complexity associated with this prethermalized regime has yet to be formally identified.

In Fig. 3.4 (b) and (c), we show a cut along $\omega = 8J$ and $W = 4J$ respectively. We explicitly see the ability of the KLD to PT to capture the changes in $\langle r \rangle_{\hat{U}_F}$ and thus the phase transition from driven thermalized to MBL (panel b) and to the prethermalized regime (panel c). Importantly, for experimentally relevant timescales, measuring the KLD to PT will not distinguish between prethermalized dynamics and higher-frequency limit where the system never thermalize to infinite temperature. In order to separate those two different scenarios, one would have to perform the experiment over timescales that grow exponentially with the drive frequency [37, 137]. Furthermore, it shows that the output probability distribution starts converging towards PT when the dynamics stop being accurately described by the time-averaged Hamiltonian \hat{H}_0 . Lastly, we note that the population imbalance is not expected to capture the difference between the driven thermalized phase and the high-frequency limit with the GOE statistic is reached. This is due to the observation of similar real-space expansion in both driven and undriven thermalized phases [38, 172].

3.4.2 The effect of noise on probing quantum phase transitions using KLD

In this section, we analyze how the finite coupling to the environment can affect the probing of quantum phase transitions using the KLD to PT. We simulate the open dynamics by considering a dissipation and a dephasing channel that are

CHAPTER 3. PROBING PHASE TRANSITIONS WITH QUANTUM ADVANTAGE SIGNATURES

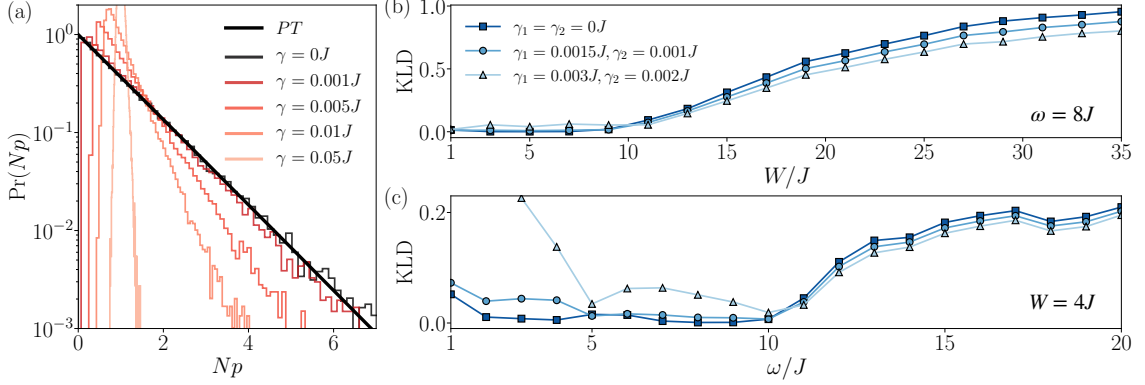


Figure 3.5: **The effect of noise on probing quantum phase transitions with KLD:** (a) Output probability distribution $\text{Pr}(Np)$ for $m = 10$ in the driven thermalized phase ($W = 4J, \omega = 8J$) as a function of noise strengths ($\gamma = \gamma_1 = \gamma_2$). The phase transition with respect to disorder W/J (b) and driving frequency ω/J (c) can be obtained by measuring the KLD to PT from the output state even in presence of finite coupling to the environment. For the circle data points, γ_1 and γ_2 are taken to be consistent with the IBMQ cloud-based quantum computing platform [173] while the triangle data points are obtained by doubling those rates. The other parameters are as in Fig 3.4.

characterised by the timescales T_1 and T_2 respectively. Given the limited amount of control required for the analog quantum simulators proposed in this work, such noise model is expected to capture the dominant experimental imperfections. Under the Born-Markov approximation, the time evolution of the density matrix $\hat{\rho}(t)$ can be described by the Lindblad master equation

$$\frac{d\rho(t)}{dt} = -i [\hat{H}(t), \rho(t)] + \sum_{i=1}^L \frac{\gamma_1}{2} \mathcal{D}[\hat{\sigma}_i^-] \hat{\rho}(t) + \frac{\gamma_2}{2} \mathcal{D}[\hat{\sigma}_i^z] \hat{\rho}(t). \quad (3.13)$$

Here, $\hat{H}(t)$ is the time-dependant Hamiltonian given in eq. Equation 3.1, $\gamma_1 = 1/T_1$ and $\gamma_2 = 1/T_2$ are the dissipation and decoherence rates respectively and $\mathcal{D}[\hat{o}]\rho(t) = 2\hat{o}\rho(t)\hat{o}^\dagger - \rho(t)\hat{o}^\dagger\hat{o} - \hat{o}^\dagger\hat{o}\rho(t)$. Equation 3.13 represents each qubit being coupled to zero-temperature independent thermal baths and is standard to accurately describe many quantum.

CHAPTER 3. PROBING PHASE TRANSITIONS WITH QUANTUM ADVANTAGE SIGNATURES

The results of the full numerical simulation of Equation 3.13 is shown in Fig 3.5. In panel (a), we show how the output distribution in the driven thermalized phase changes as the coupling to the environment increases with $\gamma_1 = \gamma_2 \equiv \gamma$. The interplay between dissipation, decoherence and continuous driving leads to a deviation of the output distribution from the PT distribution consistent with the predictions of Ref. [57]. In panels (b) and (c), we show the phase transitions as the disorder and drive frequency are respectively increased. For coupling rates γ_1 and γ_2 representative of state-of-the-art experiments [9, 173–176] (circle data points), we still observe clear phase transitions. As expected, the regime that is the most affected corresponds to long period times T (i.e. low-frequency driving $\omega = 2\pi/T$) which requires longer experimental times for fixed driving cycles $m = 10$. To emphasize this observation, we compare with larger coupling rates to the environment (2x increased in γ) as shown by the triangle data points; revealing the robustness of the experiment for a large portion of the parameter space.

Those results highlight the maturity of existing analog quantum simulators [9, 173–176] compared to the more standard gate-based computations where the limited gate fidelities generally become the dominant source of experimental imperfections. They are thus a promising sign for driven analog systems for NISQ applications.

3.4.3 Porter-Thomas distribution and infinite temperature thermalization

So far, our only intuition about PT distribution is a signature of the dynamics with a capability to uniformly explore its Hilbert space. Here we provide additional

CHAPTER 3. PROBING PHASE TRANSITIONS WITH QUANTUM ADVANTAGE SIGNATURES

physical intuitions by making a direct link between the PT distribution and thermalization to infinite temperature. This relation highlights the crucial role of the drive in providing the required energy to reach the PT distribution in our finite-size model.

In an isolated quantum system \mathcal{S}_{tot} described by a pure state $|\Psi\rangle$, the concept of thermalization is usually understood as the emergence of homogeneous statistical properties of the reduced density matrices $\hat{\rho}_{\mathcal{S}} = \text{Tr}_{\mathcal{B}}|\Psi\rangle\langle\Psi| \equiv \exp(-\hat{H}_{\mathcal{S}}/k_B T_{\text{eff}})/\mathcal{Z}$. Here, \mathcal{S} denotes any “small” subsystems with corresponding Hamiltonian $\hat{H}_{\mathcal{S}}$ of dimensions $N_{\mathcal{S}}$ and partition function \mathcal{Z} such that $\mathcal{S}_{\text{tot}} = \mathcal{S} + \mathcal{B}$ and $N_{\mathcal{B}} \gg N_{\mathcal{S}}$. The effective temperature T_{eff} is defined from the reduced density matrices and should become independent of frequency and of the subsystem choice as the full system reaches thermalization [139, 163]. By writing $|\Psi\rangle = \sum_i^{N_{\mathcal{S}}} \sum_j^{N_{\mathcal{B}}} c_{ij} |i_{\mathcal{S}}\rangle |j_{\mathcal{B}}\rangle$, where $|j_{\mathcal{S}}\rangle$ and $|i_{\mathcal{B}}\rangle$ are basis states of the subsystem and the bath respectively with $c_{ij} \in \mathbb{C}$, we obtain

$$\hat{\rho}_{\mathcal{S}} = \sum_{i,j=1}^{N_{\mathcal{S}}} \left[\sum_{k=1}^{N_{\mathcal{B}}} c_{ik} c_{jk}^* \right] |i_{\mathcal{S}}\rangle \langle j_{\mathcal{S}}|. \quad (3.14)$$

In the case where $N_{\mathcal{B}} \gg N_{\mathcal{S}}$ and the output probability distribution of $|\Psi\rangle$ follows the PT distribution given in Eq. Equation 3.11, it can be shown that $\langle i_{\mathcal{S}} | \hat{\rho}_{\mathcal{S}} | j_{\mathcal{S}} \rangle = \sum_{k=1}^{N_{\mathcal{B}}} c_{ik} c_{jk}^* \rightarrow \delta_{ij}/N_{\mathcal{S}}$ with δ_{ij} being the Kronecker delta function [177]. The vanishing off-diagonal elements come as a consequence that the amplitudes c_{ik} underlying the PT distribution are random complex numbers subjected to the normalization constraint $\langle \Psi | \Psi \rangle = 1$. This result leads to an effective infinite temperature $T_{\text{eff}} \rightarrow \infty$.

CHAPTER 3. PROBING PHASE TRANSITIONS WITH QUANTUM ADVANTAGE SIGNATURES

Interestingly, this link between PT distribution and infinite temperature thermal phase suggests an alternative quantum primacy signature that could be probed to observe the phase transitions. One could consider to use as an order parameter the difference between the entanglement entropy S_e (see section 3.3.2) of all possible subsystems $\{\mathcal{S}\}$ and the entropy averaged over the Haar-measure on the space of unit vectors of size 2^L , $S_{\text{PT}} = \log_2(N_{\mathcal{S}}) - \frac{N_{\mathcal{S}}-1}{2\ln(2)N_{\mathcal{S}}}$ [177] (i.e. leading to the PT distribution). More details concerning the entanglement entropy as a possible alternative route are given in Section 3.4.5.

3.4.4 Drive-induced long-range multi-body interactions

More physical intuitions can be gained by highlighting the crucial role of the effective long-range multi-body interactions induced by the drive in facilitating a more efficient exploration of the Hilbert space. To see this, it is insightful to investigate the time-independent Floquet Hamiltonian \hat{H}_F . For interacting systems, it is generally impossible to find an analytic form for \hat{H}_F and one needs to resort to approximations. The most common approach is using the Magnus expansion to expand $\exp[-iH_F T]$ in a power series of E_c/ω , where E_c is a characteristic energy of the Hamiltonian $\hat{H}(t)$ [178–180]. Doing so, one can write the Floquet Hamiltonian as $\hat{H}_F = \sum_{l=0}^{\infty} \hat{H}_F^{(l)}$, where the two first terms, for example, read

$$\hat{H}_F^{(0)} = \frac{1}{T} \int_0^T d\tau_1 \hat{H}(\tau_1) = \hat{H}_0, \quad (3.15)$$

$$\hat{H}_F^{(1)} = \frac{1}{2iT} \int_0^T d\tau_1 \int_0^{\tau_1} d\tau_2 [\hat{H}(\tau_1), \hat{H}(\tau_2)]. \quad (3.16)$$

In the limit of infinite frequencies $\omega \rightarrow \infty$, \hat{H}_F converges to \hat{H}_0 , while the series diverges in the low frequency regime $\omega < E_c$. For our model, we here explicitly

CHAPTER 3. PROBING PHASE TRANSITIONS WITH QUANTUM
ADVANTAGE SIGNATURES

compute the Magnus expansion up to the second order correction. The first term reads

$$\hat{H}_F^{(1)} = \frac{1}{2iT} \int_{t_0}^{T+t_0} d\tau_1 \int_{t_0}^{\tau_1} d\tau_2 [\hat{H}(\tau_1), \hat{H}(\tau_2)] \quad (3.17)$$

$$= \frac{1}{2iT} \int_{t_0}^{T+t_0} d\tau_1 \int_{t_0}^{\tau_1} d\tau_2 [\hat{H}_0, \hat{H}_d(\tau_2) - \hat{H}_d(\tau_1)] \quad (3.18)$$

$$= \frac{2i\delta B \sin(\omega t_0)}{\omega} \left[\sum_{j=1}^L h_j \hat{\sigma}_j^y + J \sum_{j=1}^{L-1} (\hat{\sigma}_j^y \hat{\sigma}_{j+1}^z + \hat{\sigma}_j^z \hat{\sigma}_{j+1}^y) \right] \quad (3.19)$$

The choice of $t_0 = 0$ is arbitrary and can lead to different forms of the Floquet Hamiltonian \hat{H}_F . Here, we fix $t_0 = 0$, leading to $\hat{H}_F^{(1)} = 0$. The second order correction term adopts the form

$$\hat{H}_F^{(2)} = -\frac{1}{6T} \int_{t_0}^{T+t_0} d\tau_1 \int_{t_0}^{\tau_1} d\tau_2 \int_{t_0}^{\tau_2} d\tau_3 \times \left([\hat{H}(\tau_1), [\hat{H}(\tau_2), \hat{H}(\tau_3)]] + (1 \Leftrightarrow 3) \right) \quad (3.20)$$

$$\begin{aligned} &= \frac{-4\delta B}{\omega^2} \left\{ \sum_{j=1}^L h_j^2 \hat{\sigma}_j^x + 2J \sum_{j=1}^{L-1} (h_j \hat{\sigma}_j^x \hat{\sigma}_{j+1}^z + h_{j+1} \hat{\sigma}_j^z \hat{\sigma}_{j+1}^x) + J^2 \sum_{j=1}^{L-1} (\hat{\sigma}_j^x + \hat{\sigma}_{j+1}^x) \right. \\ &\quad \left. + 2J^2 \sum_{j=1}^{L-2} (\hat{\sigma}_j^z \hat{\sigma}_{j+1}^x \hat{\sigma}_{j+2}^z) \right\} + \frac{4B_0\delta B}{\omega^2} \left\{ \sum_{j=1}^L h_j \hat{\sigma}_j^z + 2J \sum_{j=1}^{L-1} (\hat{\sigma}_j^z \hat{\sigma}_{j+1}^z - \hat{\sigma}_j^y \hat{\sigma}_{j+1}^y) \right\}. \end{aligned} \quad (3.21)$$

The crucial point is that higher-order contributions generally include multi-body and longer-range effective interactions. For example, $\hat{H}_F^{(2)}$ includes three-body interaction terms of the form $\hat{H}_i \sim \frac{J^2}{\omega^2} \delta B \hat{\sigma}_{i-1}^z \hat{\sigma}_i^x \hat{\sigma}_{i+1}^z$. This tendency suggests that in the limit where the series diverges, the dynamics is governed by infinitely-long range multi-body interactions. In Fig. 4.1 (b) we show that as the driving frequency decreases, the level statistics of \hat{U}_F starts converging toward the COE as the higher-order terms in the Magnus expansion start playing an increasingly important role.

CHAPTER 3. PROBING PHASE TRANSITIONS WITH QUANTUM ADVANTAGE SIGNATURES

This is captured by comparing the statistics of the full evolution \hat{U}_F with the statistics of the evolution \hat{U}_0 solely generated by the averaged Hamiltonian \hat{H}_0 . The same is observed in Fig. 3.4 (a) where the output probability distribution $\text{Pr}(p)$ starts converging toward the PT distribution only once the evolution under \hat{H}_0 fails at approximating the exact evolution. This observation sheds light on the advantages of periodically driven systems to explore larger regions of their Hilbert space by highlighting the effectively enhanced connectivity of the model, which leads to faster growth of entanglement. Note that two-body long-range interactions in 1D systems have been shown to slow down the entanglement entropy growth compared to nearest-neighbour interacting models [181]. This results further highlights the importance of the multi-body nature of the induced interactions.

3.4.4.1 Comparison between analog and digital approaches in reaching the PT distribution

The effective long-range interactions generated by the external drive suggests that driven analog quantum simulators should produce output distributions following PT more efficiently compared to digital random quantum circuits with the same topology. Here, we compare the time it takes for a quantum state to evolve toward the PT distribution under the dynamics of the driven analog Ising spin chain and the 1D digital random quantum circuits [57]. To keep the comparison fair, we consider the same interaction topology, i.e. a 1D system with nearest-neighbour couplings and open boundary conditions.

The model we use to simulate the random quantum circuits is based on Ref.[57] and consists of m layers of gates acting on L qubits, as depicted in Fig. 3.6(b). Each

CHAPTER 3. PROBING PHASE TRANSITIONS WITH QUANTUM
ADVANTAGE SIGNATURES

layer consists of a series of single-qubit gates followed by a series of controlled-Z gates. Moreover, a layer of Hadamard gates is added once at the very beginning of the circuit. Each single-qubit gate is chosen randomly from the set $\{\sqrt{\hat{\sigma}^x}, \sqrt{\hat{\sigma}^y}, \hat{T}\}$, where $\sqrt{\hat{\sigma}^x}$ ($\sqrt{\hat{\sigma}^y}$) represents a $\pi/2$ rotation around the X (Y) axis of the Bloch sphere and \hat{T} is a non-Clifford gate represented by the diagonal matrix $\{1, e^{i\pi/4}\}$. As the same to the analog case, we measure the output distribution $\Pr(p)$ averaged over D distinct realizations of this model circuit. In order to compare the evolution time, we set the driving period of the analog Ising chain to be approximately equal to the duration of a single layer of gates ($m = 1$) of the digital circuit. Since single-qubit gates can usually be implemented much faster compared to two-qubit gates, we assume that each layer takes the same time as a controlled-Z gate from a standard $J\sigma_i^z\sigma_{i+1}^z$ coupling, i.e. $t_m \sim \pi/4J$. This results in a driving frequency $\omega = 8J$.

In Fig. 3.6(c)-(d), we plot the $\text{KLD}(\Pr(p) \parallel \text{PT}(p))$ with $p = p_m(\mathbf{z})$ for the driven Ising chain and the digital random circuits, respectively, as a function of the driving cycle m for different system sizes L . The long time limit is shown in Fig. 3.6 (e). We observe that, despite having the same topology, the driven analog system converges to the PT distribution considerably faster as a results of the enhanced connectivity induced by the drive. Given the limited coherence times in the current state-of-the-art quantum platforms, such gain makes the analog approaches more favorable as testbeds for quantum primacy. Moreover, the analog approach does not require precise local control to implement the gates.

CHAPTER 3. PROBING PHASE TRANSITIONS WITH QUANTUM ADVANTAGE SIGNATURES

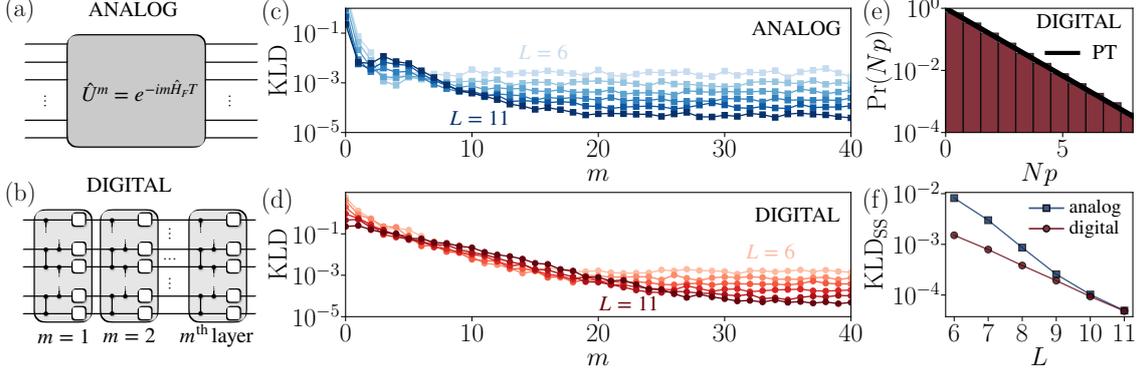


Figure 3.6: **Benchmarking the efficiency of producing the PT distribution** with analog and digital approaches: **(a)** a circuit diagram of the analog driven quantum Ising chain with m driving cycles. **(b)** a circuit diagram of random quantum circuits containing m layers of random single qubits in the set $\{\sqrt{\hat{\sigma}^x}, \sqrt{\hat{\sigma}^y}, \hat{T}\}$ and controlled-Z gates. **(c)** **(d)** $\text{KL}(\text{Pr}(p) \parallel \text{PT}(p))$ as a function of m and the size of the system L for the analog (digital) approach. **(e)** The output distribution, weighted by $N = 2^L$, in the analog case with $L = 11$ and $m = 40$. The yellow line is the exact PT distribution. **(f)** KL divergence at the long time limit of the analog and the digital cases as a function of L . ($W = 3J$, $B_0 = -\delta B = 1.25J$, $\omega = 8J$ and 500 disorder realizations.)

3.4.5 Entanglement entropy as an alternative signature

In this section, we extend upon the discussion in section 3.4.3 and describe how some expected characteristics in the entanglement entropy of driven thermalized quantum states could be used as an alternative order parameter. As mentioned earlier, the convergence of the output distribution of a quantum state towards the PT distribution is an indication of the homogeneous exploration of the Hilbert space by the dynamics. This comes as the output distribution of a fully random quantum state, i.e. sampled from the Haar measure over the space of unit vectors of size $N_{\text{tot}} = 2^L$, is given by the PT distribution. On the other hand, by dividing the system described by such random quantum state into two parts, \mathcal{S} and \mathcal{B} of size $N_{\mathcal{S}}$ and $N_{\mathcal{B}}$ respectively with $1 \ll N_{\mathcal{S}} \leq N_{\mathcal{B}}$, it has been shown to lead to an averaged

CHAPTER 3. PROBING PHASE TRANSITIONS WITH QUANTUM
ADVANTAGE SIGNATURES

entanglement entropy $S_{\text{PT}} = \log_2(N_{\mathcal{S}}) - \frac{N_{\mathcal{S}}-1}{2\ln(2)N_{\mathcal{B}}}$ [177]. Here the average is taken over the Haar measure of quantum states and the entropy is defined in Sec. 3.3.2. Converging towards S_{PT} homogeneously over the system, i.e. independently of the partition \mathcal{S} , thus strongly suggests that the underlying pure quantum state over the entire system follows the PT distribution. Consequently, an alternative route to probe the anti-concentration condition could be to measure the entanglement entropy $S_e = -\text{Tr}\{\hat{\rho}_{\mathcal{S}} \log_2 \hat{\rho}_{\mathcal{S}}\}$ of multiple subsystems \mathcal{S} and show that $S_e \rightarrow S_{\text{PT}}$ homogeneously over the whole system.

In Fig. 3.7, we plot the entanglement entropy S_e as the function of ω and W averaged over multiple subsystems. We choose six different subsystems consisting of three sites randomly selected and calculate their entanglement entropy after an evolution over $m = 10$ driving cycles. We see that the system approaches $S_{\text{PT}} \approx 3$ when the output probability follows PT and the statistics of \hat{U}_F converges toward the COE. The homogeneity of the thermalized phase is indicated by the low variance of S_e over the different subsystems. We note that entanglement entropy of undriven systems has been experimentally measured in different quantum platforms [138, 163, 167, 182].

3.5 Conclusion and outlook

In this work, we have described how key signatures of quantum primacy in a driven analog interacting system can be directly used to probe its dynamical quantum phase diagram. More precisely, we have focused on showing how a divergence as measured via KLD from the distribution of the output state probabilities to the PT

CHAPTER 3. PROBING PHASE TRANSITIONS WITH QUANTUM ADVANTAGE SIGNATURES

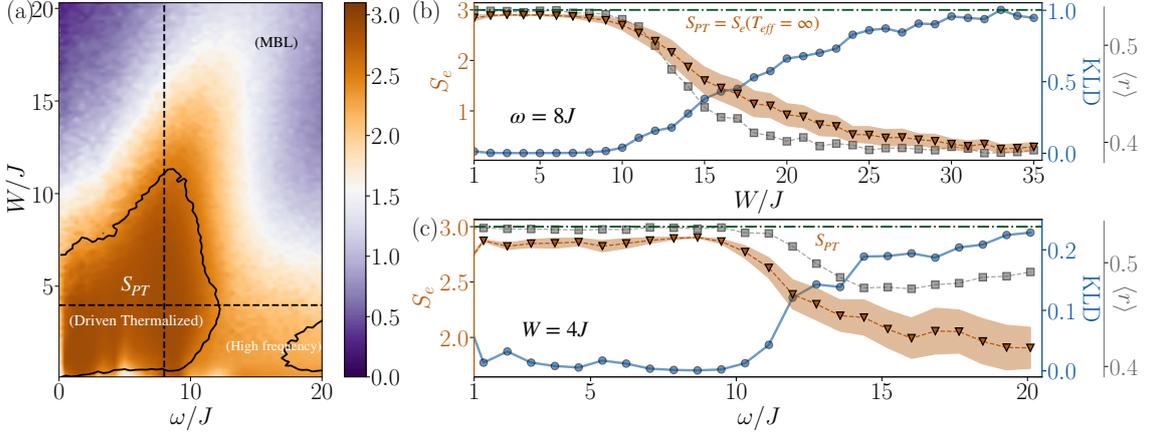


Figure 3.7: **Probing the phase diagram with entanglement entropy.** (a) The average entanglement entropy over six different subsystems, each containing three sites chosen randomly, is used as an alternative quantum primacy signature to revisit the phase diagram. The vertical and horizontal cuts show the average entanglement entropy as a function of (b) W/J and (c) ω/J . The shaded orange region indicates one standard deviation. The horizontal dashed lines represent the maximal entropy at the infinite temperature $S_{\max} = S_e(T_{\text{eff}} = \infty)$. The KLD to PT $\text{KLD}(\text{Pr}(p) \parallel \text{PT}(p))$ (blue circles) and the average level spacing $\langle r \rangle_{\hat{U}_F}$ (grey squares) are also plotted for comparison. All parameters are identical to those in Fig. 3.4. The low variance in the thermalized phase indicates the homogeneity.

distribution can play the role of an order parameter capturing the transitions from the driven thermalized phase to the driven MBL phase and the Floquet prethermalized regime.

In this context, we have highlighted the clear connection between the effective multi-body long-range interactions generated by a drive and the capability of the system to reach the PT distribution. Compared to the commonly measured population imbalance [138, 165–167], which captures the diffusion of an initial state in real space, the KLD to PT gives us information about diffusion in the Hilbert space. Beside proposing an alternative order parameter for dynamical phase transitions, this work adopts a different angle more oriented towards the complexity theory. It represents a direct application of the very same protocol proposed to demonstrate

CHAPTER 3. PROBING PHASE TRANSITIONS WITH QUANTUM ADVANTAGE SIGNATURES

quantum primacy in generic driven many-body systems currently available in wide range of analog quantum platforms including cold atom, ions and superconducting chips. An interesting next step would be to analyse in more details the computational complexity aspects of the high frequency limit or explore the cases of bosonic models such as the Bose-Hubbard one.

Chapter 4

Parametrized analog quantum systems for machine learning applications

This chapter summarizes the material published in

- J. Tangpanitanon, S. Thanasilp, MA. Lemonde, N. Dangiam, DG. Angelakis, “Expressibility and trainability of parametrized analog quantum systems for machine learning applications”, *Physical Review Research* 2 (4), 043364, (2020).

4.1 Introduction

A common approach to operate NISQ devices is to implement variational quantum algorithms (VQAs), where a classical feedback loop is used to passively mitigate the noise in the quantum device [87, 183, 184]. VQAs have been implemented to tackle a wide range of problems, from quantum chemistry [185–190], machine learning [191, 192], quadratic binary optimization [124, 193, 194], to high energy physics [195].

One of the key questions for NISQ devices is whether they can provide provable quantum advantage for real-world problems. A hint to answer this question lies in the ability of NISQ devices to efficiently explore Hilbert space. For example, in

CHAPTER 4. PARAMETRIZED ANALOG QUANTUM SYSTEMS FOR MACHINE LEARNING APPLICATIONS

quantum chemistry, NISQ devices can produce highly-entangled variational ansatzes, such as unitary coupled clusters, that cannot be efficiently represented on a classical computer [196]. In machine learning, quantum circuits have been proven to have more ‘expressive power’ than any classical neuron networks [90–92]. This means that those circuits can produce complex probability distributions that cannot be efficiently sampled from a classical computer.

Similar to classical variational algorithms, VQAs rely on ‘good’ ansatzes that can efficiently capture the answer of a given problem. In the case when such ansatz is not known or implementable, it is desirable to exploit high expressibility of some NISQ devices to generate an unbiased guess. The latter is known as ‘hardware efficient’ [187]. A common feature of this approach is to explore the chaotic dynamics which allows the system to quickly explore the entire Hilbert space. However, this chaoticity also makes it difficult, if not impossible, to classically optimize the system since it is highly sensitive to any small changes in the parameters. In the digital case, hardware efficient ansatzes with high expressibility suffer from the barren plateaus problem [94, 95], where the landscape of the cost function becomes exponentially flat as the number of qubits increases. Hence, finding the optimal variational ansatz for a given problem is an emerging art of balancing expressibility, implementability and trainability of the NISQ devices.

Analog quantum simulators stand out from their digital counterpart when it comes to implementability [34, 114, 115]. Here, a quantum device is built to mimic a specific Hamiltonian, which requires significantly less control than universal quantum circuits. State-of-the-art quantum simulators have already been able to produce

CHAPTER 4. PARAMETRIZED ANALOG QUANTUM SYSTEMS FOR MACHINE LEARNING APPLICATIONS

dynamics intractable by existing classical algorithms [40]. Proposals to demonstrate quantum primacy in analog simulators have also been proposed in 2D Ising lattice [116, 117], cluster states [118], and more recently in periodically-driven quantum many-body systems (as introduced in the previous chapters). Hybrid analog-digital approaches for VQAs have been explored in Refs [186–188, 192, 193, 197–199].

In this work, we analyze the expressibility and trainability of analog quantum devices focusing on parameterized driven quantum many-body systems. We show that these properties are intimately related to phases of the system. We focus on four generic phases depending on whether the dynamics is thermalized or many-body localized (MBL) [138, 200] and whether a continuous drive is applied. As an example, we consider the standard Ising chain, globally driven by an external magnetic field. We find that, evolving under the dynamics resulting from a series of quenches between randomized disorder configurations, the system in all four phases are capable of reaching the maximal expressibility regime where the system can uniformly explore the whole Hilbert space, which we called the “quantum primacy” regime. We then devise a simple sequential training protocol to train the system for generative modeling tasks in machine learning. We show that the chaoticity in the thermalized phase prevents the training as in the digital case. However, the integrability of the MBL within each quench increases drastically the trainability of the system. The final learning accuracy depends solely on the phase of the system.

CHAPTER 4. PARAMETRIZED ANALOG QUANTUM SYSTEMS FOR
MACHINE LEARNING APPLICATIONS

Features	$f(t) = 0$		$f(t) \neq 0$	
	Thermalized	MBL	Thermalized	MBL
Statistics of $\hat{H}_{\text{ave}}(\boldsymbol{\theta}_m)$	GOE	POI	-	-
Statistics of $\hat{U}(\boldsymbol{\theta}_m)$	-	-	COE	POI
Statistics of $\hat{U}(\boldsymbol{\Theta}_M)$ with $M \gg 1$	CUE	CUE	CUE	CUE
High expressibility (quantum primacy)	yes	yes	yes	yes
Trainability for generative modeling	no	yes	no	yes (best)

Table 4.1: A summary of statistics, expressibility, and trainability in the four regimes, defined by whether $\hat{U}(\boldsymbol{\theta}_m)$ is thermalized or MBL and whether $f(t) = 0$ or $f(t) \neq 0$. The symbol ‘-’ indicates that the statistics is not defined.

4.2 General framework

In this section, we study the many-body dynamics of generic parameterized quantum systems and the different statistics associated with their phases. We then analyze a specific example of driven quantum Ising chain which will be used for the analysis of the expressibility and trainability in the following sections.

4.2.1 Quench dynamics as a parametrized model

We consider parametrized quenched quantum many-body systems $|\psi(\boldsymbol{\Theta}_M)\rangle = \hat{U}(\boldsymbol{\Theta}_M)|\psi_0\rangle$, where $|\psi_0\rangle$ is an initial product state, $\boldsymbol{\Theta}_M$ is a vector containing all variational parameters during the evolution and M is the number of times the system is quenched. The unitary time evolution is

$$\hat{U}(\boldsymbol{\Theta}_M) = \hat{U}(\boldsymbol{\theta}_M)\hat{U}(\boldsymbol{\theta}_{M-1})\dots\hat{U}(\boldsymbol{\theta}_1), \quad (4.1)$$

CHAPTER 4. PARAMETRIZED ANALOG QUANTUM SYSTEMS FOR
MACHINE LEARNING APPLICATIONS

where $\Theta_M = \{\boldsymbol{\theta}_m\}_{m=1}^M$ and each quench/layer is obtained from a time-dependent Hamiltonian $\hat{H}(\boldsymbol{\theta}_m, t)$, i.e.

$$\hat{U}(\boldsymbol{\theta}_m) = \hat{\mathcal{T}} \exp \left(-i \int_0^T \hat{H}(\boldsymbol{\theta}_m, t) dt \right), \quad (4.2)$$

with $m \in \{1, 2, \dots, M\}$, $\hat{\mathcal{T}}$ being the time-ordering operator and T being the evolution time during each layer. The Hamiltonian is further decomposed as

$$\hat{H}(\boldsymbol{\theta}_m, t) = \hat{H}_0(\boldsymbol{\theta}_m) + f(t)\hat{H}_d, \quad (4.3)$$

where $\hat{H}_0(\boldsymbol{\theta}_m)$ is a static Hamiltonian, \hat{H}_d is the driving Hamiltonian such that $[\hat{H}_0(\boldsymbol{\theta}_m), \hat{H}_d] \neq 0$. The modulation $f(t)$ is an oscillating function with the period T . We require that the time-averaged Hamiltonian $\hat{H}_{\text{ave}}(\boldsymbol{\theta}_m) = \frac{1}{T} \int_0^T \hat{H}(\boldsymbol{\theta}_m, t) dt$ is many-body [125].

4.2.2 The four phases of $U(\boldsymbol{\theta}_m)$

In the following, we will refer to $\hat{U}(\boldsymbol{\theta}_m)$ as ‘thermalized’ if any observations made on $|\psi'_{M'}\rangle = \hat{U}(\boldsymbol{\theta}_m)^{M'}|\psi_0\rangle$ with $M' \rightarrow \infty$ can be obtained from the micro-canonical ensemble predictions associated with the energy $\bar{E}(\boldsymbol{\theta}_m) \pm \Delta E$, where $\bar{E}(\boldsymbol{\theta}_m) = \langle \psi_0 | \hat{H}_{\text{eff}}(\boldsymbol{\theta}_m) | \psi_0 \rangle$. The effective Hamiltonian $\hat{H}_{\text{eff}}(\boldsymbol{\theta}_m)$ is defined such that $\hat{U}(\boldsymbol{\theta}_m) \equiv \exp[-i\hat{H}_{\text{eff}}(\boldsymbol{\theta}_m)T]$. Most quantum many-body systems follow this property according to the eigenstate thermalization hypothesis (ETH) [163]. Likewise, we refer to $\hat{U}(\boldsymbol{\theta}_m)$ as ‘many-body localized’ if the above is not true due to large disorder [119]. Partial experimental signatures of the MBL have been observed in cold neutral atoms [38, 40, 201–203], superconducting circuits [39, 204], and trapped ions [205].

CHAPTER 4. PARAMETRIZED ANALOG QUANTUM SYSTEMS FOR MACHINE LEARNING APPLICATIONS

We can now define the four regimes or ‘phases’ of $\hat{U}(\boldsymbol{\theta}_m)$ in the above sense according to whether the dynamics is thermalized or MBL and whether $f(t)$ is zero or non-zero. To allow non-trivial dynamics within each layer, we require $2\pi/T$ to be smaller than a typical energy gap of $\hat{H}_{\text{ave}}(\boldsymbol{\theta}_m)$. We assume that all $\hat{U}(\boldsymbol{\theta}_m)$ ’s in $\hat{\mathcal{U}}(\boldsymbol{\Theta}_M)$ belong to the same phase for simplicity.

Let us explore the various statistics associated with the four phases, starting with the $f(t) = 0$ case in which $\hat{H}_{\text{eff}}(\boldsymbol{\theta}_m) = \hat{H}_{\text{ave}}(\boldsymbol{\theta}_m)$. For the thermalized dynamics, the statistics of $\hat{H}_{\text{ave}}(\boldsymbol{\theta}_m)$ follows the Gaussian orthogonal ensemble (GOE) [163]. This is the ensemble of matrices whose entries are independent normal random variables subjected to the orthogonality constraint. This randomness is a signature of quantum chaos, which is a crucial ingredient for thermalization [119]. A large disorder can prevent the system from thermalization leading to MBL dynamics. In this case, the eigenenergies of $\hat{H}_{\text{ave}}(\boldsymbol{\theta}_m)$ follow the Poisson (POI) statistics, indicating that they are uncorrelated.

In the driven case, i.e. $f(t) \neq 0$, the statistics are defined at the level of the unitary operator $\hat{U}(\boldsymbol{\theta}_m)$, as it is generally not possible to have access to \hat{H}_{eff} . For the driven thermalized dynamics, the statistics of $\hat{U}(\boldsymbol{\theta}_m)$ follows the circular orthogonal ensemble (COE) [120]. This is the ensemble of matrices whose entries are independent complex normal random variables subjected to the orthogonality and the unitary constraints. Unlike the GOE, the COE is intimately related to the infinite-temperature ensemble and is not possible to obtain without a drive [120]. As before, a large disorder can prevent thermalization even with $f(t) \neq 0$, leading to the POI statistics of the quasi-energies (to be defined later) [154, 156]. A summary

of all the statistics is given in Table 4.1.

4.2.3 Driven disordered quantum Ising chains

To illustrate the four generic phases, we consider the same model of driven quantum Ising chains used in the previous chapters with

$$\hat{H}_0(\boldsymbol{\theta}_m) = \sum_{i=1}^L \theta_{i,m} \hat{\sigma}_i^z + J \sum_{i=1}^{L-1} \hat{\sigma}_i^z \hat{\sigma}_{i+1}^z + B_0 \sum_{i=1}^L \hat{\sigma}_i^x, \quad (4.4)$$

$$\hat{H}_d = \delta B \cos(\omega t) \sum_{i=1}^L \hat{\sigma}_i^x, \quad (4.5)$$

where $f(t) = \delta B \cos(\omega t)$, $\omega = 2\pi/T$, L is the number of spins, $\{\hat{\sigma}_i^x, \hat{\sigma}_i^z\}$ are Pauli operators acting on site i , J is the interaction strength, B_0 is a static magnetic field and δB is the driving amplitude. The parameters $\boldsymbol{\theta}_m = \{\theta_{i,m}\}_{i=1}^L$ are ‘varied’ by randomly drawing them from a uniform distribution in the range $[-W/2, W/2]$ where W is the disorder strength. This allows us to vary the parameters without changing the phase of the system. The dimension of the Hilbert space is $N = 2^L$. The initial state $|\psi_0\rangle$ is prepared as a product state where each spin points along the $+z$ direction.

We recall that the standard way to analyze the statistics of the system is to define the level statistics $\text{Pr}(r_\alpha)$ as the normalized distribution of

$$r_\alpha = \frac{\min(\delta_\alpha, \delta_{\alpha+1})}{\max(\delta_\alpha, \delta_{\alpha+1})}, \quad (4.6)$$

where $\Delta_\alpha = \mathcal{E}_{\alpha+1} - \mathcal{E}_\alpha$ is the level spacing with $\mathcal{E}_{\alpha+1} > \mathcal{E}_\alpha$ and $\alpha = 1, 2, \dots, 2^L - 1$. In the $f(t) = 0$ case, $\{\mathcal{E}_\alpha\}$ are eigenenergies of $\hat{H}_{\text{ave}}(\boldsymbol{\theta}_m)$. In the $f(t) \neq 0$ case, $\{\mathcal{E}_\alpha\}$ are quasi-energies, defined such that $\{\exp(-i\mathcal{E}_\alpha)\}$ are eigenvalues of $\hat{U}(\boldsymbol{\theta}_m)$. Not only that the effective Hamiltonian of one driving cycle (i.e., Floquet Hamiltonian)

CHAPTER 4. PARAMETRIZED ANALOG QUANTUM SYSTEMS FOR MACHINE LEARNING APPLICATIONS

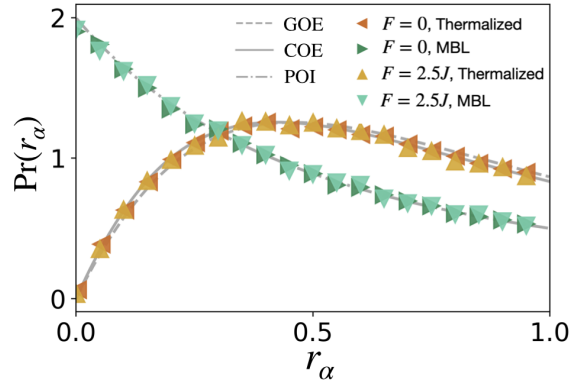


Figure 4.1: Level statistics of $\hat{H}_{\text{ave}}(\boldsymbol{\theta}_m)$ for $f(t) = 0$ and $\hat{U}(\boldsymbol{\theta}_m)$ for $\delta B = -1.25J$. The thermalized and the MBL phases are obtained with $W = 1J$ and $W = 20J$, respectively. ($L = 9$, $\omega = 8J$, $B_0 = 1.25J$, 500 disorder realizations).

is not equal to the time-averaged Hamiltonian $\hat{H}_F \neq \hat{H}_{\text{ave}}$ in the driven case, but the quasi-energies are also defined in the limited range $\mathcal{E}_\alpha \in [0, 2\pi)$. This ‘energy folding’ has profound impact on the resulting statistic.

In Fig. 4.1, we show the level statistics for $\delta B = 0$ and $\delta B = -1.25J$ with $W = 1J$ and $W = 20J$. For a small disorder $W = 1J$, the level statistics of $\hat{H}_{\text{ave}}(\boldsymbol{\theta}_m)$ and $\hat{U}(\boldsymbol{\theta}_m)$ agree with the predictions from the GOE and the COE, respectively. For a large disorder $W = 20J$, the level statistics of both $\hat{H}_{\text{ave}}(\boldsymbol{\theta}_m)$ and $\hat{U}(\boldsymbol{\theta}_m)$ follows the POI distribution, as expected.

4.3 Expressibility of driven quantum-many body systems

In this section, we show that, given a large number of quenches M , the overall dynamics described by $\hat{U}(\boldsymbol{\Theta}_M)$ for all four phases is capable of reaching the quantum primacy regime, implying high expressibility of our system beyond a classical computer.

4.3.1 Expressibility and quantum primacy

Expressibility is the term used in machine learning to describe the range of the resulting functions that a model can compute [206]. Exact measures for expressibility usually differ depending on the task. In the context of quantum computing, expressibility usually relates to how much a quantum system can explore the Hilbert space [93]. For example, product state ansatz have a lower expressibility than tensor-network ansatz, due to their inability to capture entangled states [207]. Specifically, the measure of expressibility proposed in [93] is related to the frame potential which measures how far a given unitary ensemble is from t -design [131]. However, the number of unitaries in the ensemble required to show t -design grows exponentially with L , making it impractical for large systems.

In this work, we say that a quantum model has a higher expressibility than any classical models if there exists a probability distribution $p(\mathbf{z}; \Theta_M)$ that cannot be efficiently sampled from a classical computer unless the polynomial hierarchy collapses. This situation is referred to as quantum primacy. In random quantum circuit proposals for quantum supremacy, universal set of quantum gates are designed such that the system is chaotic and follows t -design [50]. Hence, these quantum circuits produce the highest expressibility according to the measure proposed in Ref. [93].

We recall the requirements for quantum primacy. Let us consider the task of approximating $p(\mathbf{z}; \Theta_M)$ up to additive error, i.e.

$$\sum_{\mathbf{z} \in \{0,1\}^L} |p(\mathbf{z}; \Theta_M) - q(\mathbf{z})| \leq \beta, \quad (4.7)$$

where β is a positive constant, $\{\mathbf{z}\}$ are output bit-strings measured in the computational basis, $p(\mathbf{z}; \Theta_M) = |\langle \mathbf{z} | \psi(\Theta_M) \rangle|^2$ is the exact output probability, and $q(\mathbf{z})$ is the approximated value obtained from a classical / quantum device. In principle, a quantum device can satisfy this condition by directly implementing $\hat{U}(\Theta_M)$ in the hardware and measure the output multiple times to construct $q(\mathbf{z})$. To show that a classical computer cannot do the same efficiently unless the polynomial hierarchy collapses, one need to show that (i) it is #P-hard to approximate $p(\mathbf{z}; \Theta_M)$ up to multiplicative error [128], i.e.

$$|p(\mathbf{z}; \Theta_M) - q(\mathbf{z})| \leq \eta p(\mathbf{z}; \Theta_M) \quad (4.8)$$

for some η and (ii) the output probability anti-concentrates [127], i.e.

$$\Pr \left(p(\mathbf{z}; \Theta_M) > \frac{\delta}{N} \right) \geq \gamma, \quad (4.9)$$

where δ, γ are some constants.

4.3.2 Achieving quantum primacy with quenched quantum many-body systems

The #P-hardness to approximate $p(\mathbf{z}; \Theta_M)$ up to multiplicative error has been shown (for the worse instance) in the case where it results from a unitary evolution that follows the circular unitary ensemble (CUE) statistics [57, 58]. The CUE is the ensemble of matrices whose entries are independent complex normal random variables subject to the unitary constraint [130]. Such statistics can be probed from both the previously defined level statistics $\Pr(r_\alpha)$ and the distribution $\Pr(c = |\langle \mathbf{z} | \mathcal{E}_\alpha \rangle|^2)$ of the eigenstates $|\mathcal{E}_\alpha\rangle$ of $\hat{U}(\Theta_M)$.

CHAPTER 4. PARAMETRIZED ANALOG QUANTUM SYSTEMS FOR
MACHINE LEARNING APPLICATIONS

Fig. 4.2(a) and (b) show the statistics of the eigenstates and the quasi-energies of $\hat{\mathcal{U}}(\Theta_M)$ in the four regimes at $M = 400$, respectively. It can be seen that in all cases the results match with the CUE statistics, indicating the #P-hardness to approximate the resulting $p(\mathbf{z}; \Theta_M)$ up to multiplicative error. Our finding agrees with Ref [208], which shows that random quenches in atomic Hubbard and spin models with long-range interactions lead to the t -design property. The t -design ensemble produces the CUE when $t \rightarrow \infty$ which happens in the long-time limit [132].

In Fig. 4.2(c), we plot the Kullback-Leibler (KL) divergence of the output distribution $\Pr(p)$ from the Porter-Thomas distribution, $\text{PT}(p) = Ne^{-Np}$. The latter implies that the system explores the entire Hilbert space. (Here, we drop the argument Θ_M for brevity). The Porter-Thomas distribution satisfies the anti-concentration condition since $\Pr\left(p > \frac{1}{N}\right) = \int_{Np=1}^{\infty} d(Np)e^{-Np} = 1/e$ [57]. From Fig. 4.2(c), it can be seen that the system in all four phases reaches the Porter-Thomas distribution over time with different timescales. The thermalized case with the drive reaches it first at $M \sim 10$. The thermalized case with no drive and the driven MBL case have a similar convergence rate and saturate at $M \sim 100$. The static MBL has the slowest rate and saturates at $M \sim 250$. This is expected as MBL dynamics localizes the system, while the drive ‘heats up’ the system leading to de-localization.

Fig. 4.2(a)-(c) provides evidences that $|\psi(\Theta_M)\rangle$ cannot be efficiently approximated by a classical computer. This suggests that, for a large number of qubits, our system in all phases have higher expressibility than any classical models.

Lastly, we note that, unlike the previous chapters where the quantum primacy is

CHAPTER 4. PARAMETRIZED ANALOG QUANTUM SYSTEMS FOR MACHINE LEARNING APPLICATIONS

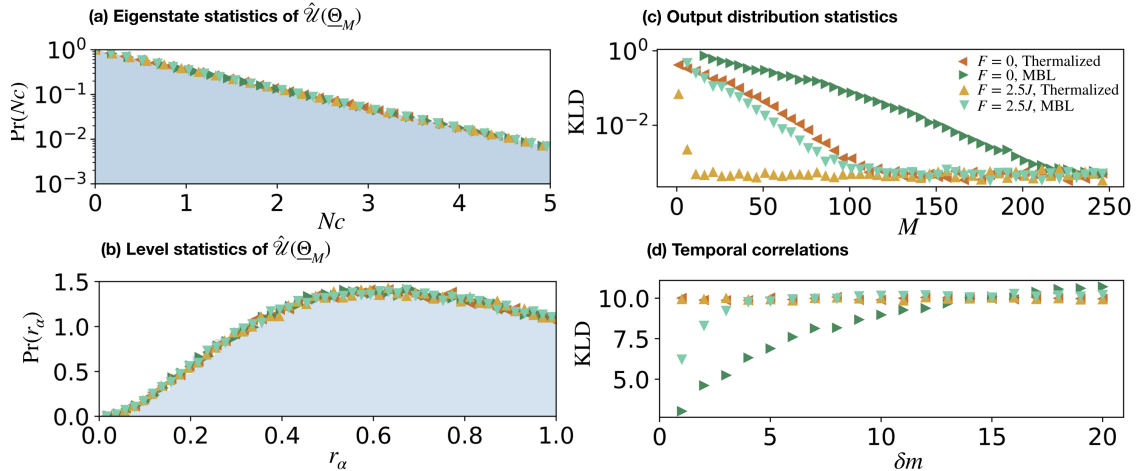


Figure 4.2: **Statistics of parameterized analog quantum many-body evolution:** (a) and (b) shows the eigenstate distribution $\Pr(N_c)$ and the level statistics $\Pr(r_\alpha)$ for the four phases of $\hat{U}(\theta_m)$, respectively with $M = 400$. The shaded areas are the predictions from the CUE statistics. (c) The KLD of the output distribution from the Porter-Thomas distribution as a function of M . (d) The KLD of $p(\mathbf{z}; \Theta_{m+\delta m})$ from $p(\mathbf{z}; \Theta_m)$ as a function of δm . The KLD is averaged over $M \in [378, 400)$ for a given δm . The thermalized and the MBL phases are obtained with $W = 1J$ and $W = 20J$, respectively. ($L = 9$, $\omega = 8J$, $B_0 = 1.25J$ and $\delta B = -B_0$ with the drive, 500 disorder realizations).

reached with periodically driven quantum systems in the thermalized phase, here the quantum primacy is achieved through the quench dynamics for all phases.

4.4 Trainability of driven analog quantum-many body systems

In the context of machine learning, having a model with large expressibility is necessary but not sufficient as the model also need to be trainable. We here address the interplay between expressibility and trainability for the four generic phases of driven analog many-body systems discussed so far. Interestingly, we show that the external drive and the temporal correlations between different quenches in the MBL phase are the key ingredients to combine those two crucial characteristics.

4.4.1 Generative modeling in classical machine learning

As a testbed to analyse the trainability of our model, we solve a generative modeling problem in machine learning [71]. The latter is an unsupervised task, meaning that the training data are unlabelled. The goal is to find the unknown probability distribution, $Q(\mathbf{z})$, underlying the training data. Here, the data is a set of binary vectors $\{\mathbf{z}\}_{\text{data}} = \{\mathbf{z}_1, \mathbf{z}_2, \dots\}$. For example, it can represent the opinions of a group of customers on a set of L different products, as depicted in Fig. 4.3(a). The opinion of the customer i is represented by a binary vector $\mathbf{z}_i = [z_{i1}, z_{i2}, \dots, z_{iL}]$ where $z_{ij} = 1$ if he/she likes the product j and -1 otherwise. After knowing $Q(\mathbf{z})$, the company can generate new data from this distribution and recommends products with $+1$ score to new customers.

In this section we use an artificial dataset as a working example. To assure the generality of the data, we assume that $Q(\mathbf{z})$ is the Boltzmann distribution of classical Ising spins with all-to-all connectivity, *i.e.*,

$$Q(\mathbf{z}) = \frac{1}{Z} e^{-E(\mathbf{z})/k_B T_0}, \quad (4.10)$$

where $Z = \sum_{\mathbf{z}} \exp(-E(\mathbf{z})/k_B T_0)$ is the partition function, k_B is the Boltzmann constant, T_0 plays the role of a temperature, and

$$E(\mathbf{z}) = \sum_{i=1}^L a_i z_i + \sum_{\langle i,j \rangle} b_{ij} z_i z_j \quad (4.11)$$

with a_i, b_{ij} being random numbers between $\pm J/2$. This model is known as the Boltzmann machine which is one of the standard types of artificial neuron networks used in machine learning and has been shown to capture a wide range of real-world data [209]. Its quantum version has been studied in [210, 211].

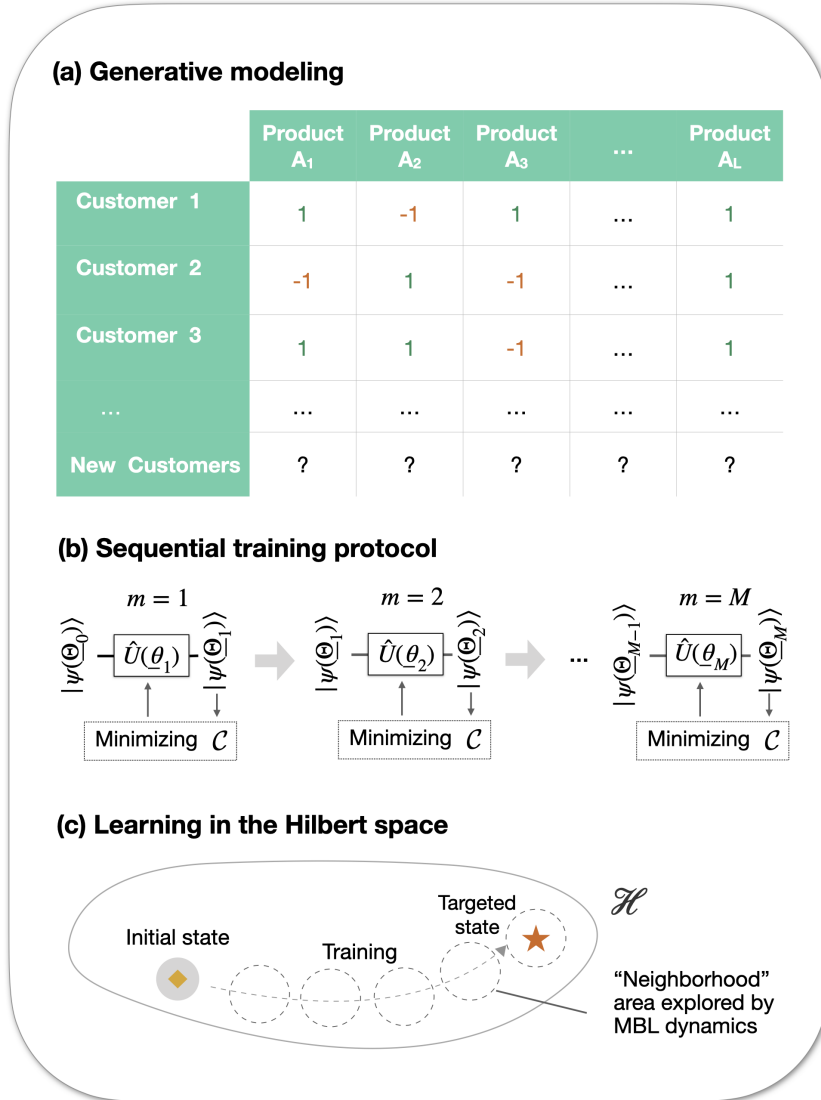


Figure 4.3: **Machine learning with a driven analog quantum processor:** (a) A table demonstrating a real-world application of generative modeling tasks in machine learning. Each customer is asked to rate whether he/she likes (+1) or dislikes (-1) a given product. (b) A sketch of optimization loops used in the training protocol. (c) A diagram showing the movement of the system in the Hilbert space during the training in the MBL phase.

4.4.2 Sequential training scheme using an analog quantum model

Classically, the distribution of $\{\mathbf{z}\}_{\text{data}}$ can be obtained by first guessing a model $P_{\text{model}}(\mathbf{z}; \Theta)$, such as the Poisson or the Boltzmann distribution, which has some variational parameters Θ . The ‘training’ is done by minimizing the cost function, which is the KL divergence of $P_{\text{model}}(\mathbf{z}; \Theta)$ from $\tilde{Q}(\mathbf{z})$ using either gradient descent or gradient-free optimization algorithms. Here, \tilde{Q} is the normalized histogram of $\{\mathbf{z}\}_{\text{data}}$.

In our case, we show how the distribution of $\{\mathbf{z}\}_{\text{data}}$ can be recovered as the output probability $p(\mathbf{z}; \Theta_M)$ of the driven quantum Ising chain. This approach is also known as the Born’s machine [92]. Our goal here is to guide or ‘train’ the quantum system to a specific point in the Hilbert space such that $p(\mathbf{z}; \Theta_M) = Q(\mathbf{z})$. Our training protocol, depicted in Fig. 4.3(b), takes place as follows:

1. Initialize the system at $|\psi(\Theta_m)\rangle = |\psi_0\rangle$ with $m = 0$ and $\Theta_0 = \{\}$.
2. Evolve the system by one layer $|\psi(\Theta_{m+1})\rangle = \hat{U}(\theta_{m+1})|\psi(\Theta_m)\rangle$ with $\Theta_{m+1} = \{\theta_{m+1}\} \cup \Theta_m$, and then measure $p(\mathbf{z}; \Theta_{m+1})$ to compute \mathcal{C} .
3. Repeat the step (2) D times with different disorder realization θ_{m+1} , randomly chosen from $[0, W]$. In the thermalized case, the system will randomly explore the entire Hilbert space in this step. However, in the MBL case, the system will only explore the Hilbert space locally near $|\psi(\Theta_m)\rangle$ allowing systematic optimization, see Fig. 4.3(c).

CHAPTER 4. PARAMETRIZED ANALOG QUANTUM SYSTEMS FOR
MACHINE LEARNING APPLICATIONS

4. Choose the disorder realization in the step (3) that minimizes \mathcal{C} , then update $m \rightarrow m + 1$. This will ‘move’ the state in the most promising direction in the Hilbert space.
5. Repeat the step (3)-(4) until convergence.

We note here three characteristics of our training protocol. First, it is sequential since not all parameters in Θ are updated at the same time, making them easier for classical optimization. Second, although the parameters are randomly drawn during the training, our optimization is done systematically in the Hilbert space. This makes an important difference to the usual optimization approaches which are done in the parameter space [94, 210]. Third, a large fraction of results is ‘thrown away’ in the step (3). Although in principle this data can be utilized to improve the training efficiency, it is our goal to keep the training protocol as simple as possible, so that the focus is made on distinct learning behaviors displayed by each phase.

4.4.3 Training results

The training results are shown in Fig. 4.4(a). As expected, the system in the thermalized phase cannot be trained. The cost function from the thermalized case with the drive saturates at $C \sim 2$ already at the first layer. In the undriven case, the cost function starts at around $C \sim 3.5$ and then falls down to saturate at $C \sim 2$, the same value as the driven case, when $M \sim 50$. For the undriven MBL case, during $M \lesssim 10^2$, the cost function steadily decays to 0.7. Then during $10^2 \lesssim M \lesssim 10^3$, the cost function continues to decay with a slower rate. Interestingly, after $M \gtrsim 10^3$, the cost function increases and saturates at 0.7 when $M \sim 10^4$. In contrast, for the

CHAPTER 4. PARAMETRIZED ANALOG QUANTUM SYSTEMS FOR MACHINE LEARNING APPLICATIONS

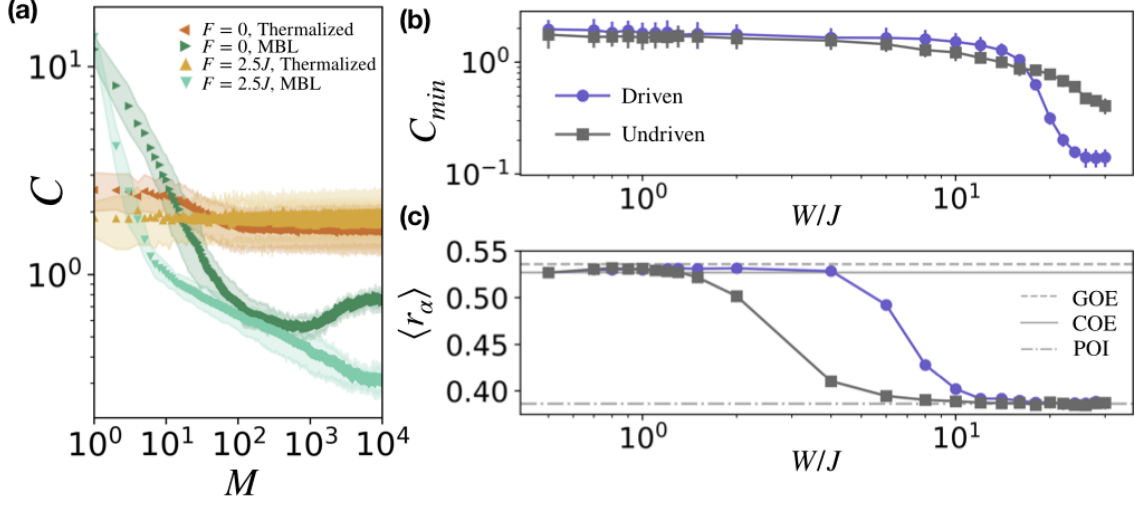


Figure 4.4: **Training analog quantum systems in the Hilbert space:** (a) The lowest cost function at each training step M for $\delta B = 0$ and $\delta B = -1.25J$. The thermalized and the MBL phases are obtained with $W = 1J$ and $W = 20J$, respectively. The shaded areas represent standard deviations. (b) The cost function at $M = 10^4$ as a function of W . The results are averaged over 10 dataset, i.e., 10 realizations of $\{a_i, b_i\}$ in Eq. (4.11). Each dataset consists of 3000 samples. (c) The averaged level spacing $\langle r_\alpha \rangle$ at $M = 10^4$ as a function of W . ($L = 9, \omega = 8J, B_0 = 1.25J, k_B T_0 = J$ and $D = 200$.)

driven MBL case, the cost function goes down steadily when $M \lesssim 10$. Then, the cost function further decays monotonically with a slower rate to saturate at $C \sim 0.1$ at $M \sim 10^4$. This results show that the learning behavior changes qualitatively depending on the phase and the timescale of the system. The best learning accuracy is obtained with the driven MBL phase.

In Fig. 4.4(b), we plot the final learning results as a function of W for the driven and undriven cases. For comparison, in Fig. 4.4(c), we also plot the averaged level spacing $\langle r_\alpha \rangle$ as a function of W for both cases. In the driven case, the final learning accuracy shows a transition between the trainable and the untrainable regimes, which corresponds roughly to the phase transition between the CUE and the POI statistics. In the undriven case, the system moves towards the trainability

CHAPTER 4. PARAMETRIZED ANALOG QUANTUM SYSTEMS FOR MACHINE LEARNING APPLICATIONS

regime as W approaches $30J$. However, we stop our calculation here as the training takes too long to converge when $W > 30J$ ¹. Nevertheless, our present results are sufficient to conclude that the drive leads to a better learning accuracy for this timescale. We conjecture that, once the system in the undriven case fully reaches the trainable regime, the learning accuracy should monotonically decrease with M until saturation.

Lastly, in machine learning, the ultimate goal is not just trainability but the capability of the model to make prediction, i.e. generalization. In addition, NISQ can only operate in a finite coherence time. To show both generalisation and implementability of our model in the MBL phase with the drive, we train the model with 2,000 training data sampled from the distribution in Eq. (4.10) using only up to $M = 20$ cycles. In Fig. 4.5, we plot the KLD between $p(\mathbf{z}; \Theta_M)$ and the testing distribution generated by 1,000 testing data which are newly sampled from Eq. (4.10). We can see that the cost function converges for both training and testing data set, indicating that the model does not overfit the data. We have also repeated the calculations in this section with a different dataset drawn from the Bernoulli distributions [210] and similar results are obtained (not presented).

4.4.3.1 Temporal correlations enabled by MBL

To understand different learning accuracy in different phases, we calculate the KL divergence between $p(\mathbf{z}; \Theta_M)$ and $p(\mathbf{z}; \Theta_{M+\delta m})$ to measure the temporal correlations or the ‘memory’ between outputs at different layers. In Fig. 4.2(d), we plot such KL

¹For $M = 10^4$, it takes approximately 1,200 CPU hours to generate Fig. 4.4(b) using Intel Xeon E5-2690 v3 processors.

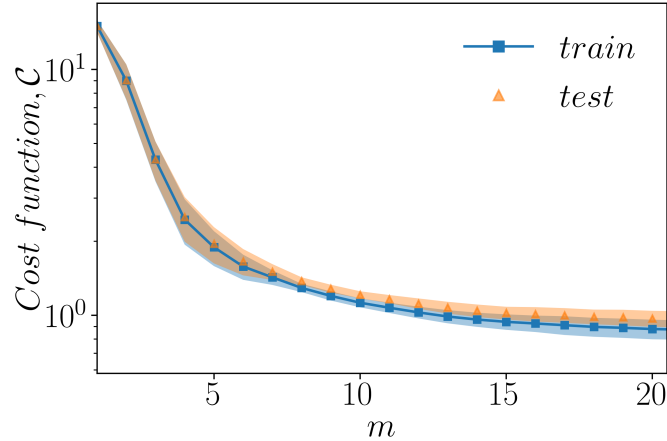


Figure 4.5: The lowest cost function at each training step M for $\delta B = -1.25J$ and $W = 30J$. The training data (2,000 samples) and the testing data (1,000 samples) are independently generated from Eq. (4.10). ($L = 9$, $\omega = 8J$, $B_0 = 1.25J$, $k_B T_0 = J$.)

divergence as a function of δm , averaged over various M 's. In the thermalized phase, we find that there are no temporal correlations between layers. This is expected as each layer has chaotic dynamics which is highly sensitive to any small changes introduced to the system. In contrast, in the MBL phase, the system displays short-term memory that decays with δm . The MBL dynamics with $f(t) = 0$ has the longest memory. This memory were exploited during the training to improve trainability of the system. We note that since at large M the system produces a random state, the results in Fig.4.2(d) can be equivalently obtained using short-time dynamics with $M = 0$, but averaged over many random initial states.

4.5 Conclusions

In this work, we have thoroughly analyzed the expressibility and trainability of parameterized analog quantum many-body systems. We show that both thermalized

CHAPTER 4. PARAMETRIZED ANALOG QUANTUM SYSTEMS FOR MACHINE LEARNING APPLICATIONS

and MBL dynamics with and without the driving modulation $f(t)$ are capable of reaching the quantum supremacy regime, indicating high expressibility beyond any classical models. In the context of generative modeling, we show that chaoticity prevents systematic optimization of the system. However, the latter can be qualitatively improved by the MBL dynamics. The key to successful training in the MBL cases is due to the temporal memory in the evolution. In the future, it would be interesting to further analyze generalization of our models as well as more complex training protocol for efficient optimization.

Chapter 5

Conclusion and Future Work

5.1 Conclusion

In this thesis, we have discussed and investigated the connection among analog quantum simulation, quantum primacy and quantum machine learning. Here, we summarize our key findings and future prospects of our work.

5.1.1 Summary of results

In Chapter 2, we provide theoretical evidence that the quantum primacy can be achieved by sampling from generic periodically driven many-body systems in the thermalized phase. Our theoretical analysis relies on the non-collapse of the polynomial hierarchy and a closed connection between random matrix theory and driven quantum many-body systems. Our proposal can be practically implemented using currently available analog quantum devices and demonstrate the formal connection between phases of matter and computational complexity. In Chapter 3, we show that the previously proposed set-up can be extended to probe quantum phase transitions. Our new accessible order parameters based on quantum primacy signatures

can be used to well capture the phase transitions from the driven thermalized to MBL phases, as well as to the high frequency regime of prethermalization. Moving to quantum machine learning, in Chapter 4, we investigate the expressibility and trainability of analog quantum simulators based on quantum quench dynamics to perform machine learning tasks. Maximally expressive power can be achieved for all phases. However, training performance depends significantly on the phases that the analog systems operate on. While thermalized phases exhibit chaoticity which leads to their untrainability, MBL phases can be well trained due to their temporal correlation between quenches. Our work suggests that the phases of analog quantum simulators are fundamentally linked with the performance of machine learning tasks.

5.1.2 Future prospects

There are a few directions we can extend our thesis. The obvious extension of studies in Chapter 2 is to practically implement our quantum primacy proposal using available quantum platforms such as cold atoms or trapped ions. The large-scale experiment would serve as a crucial benchmark in the field of quantum simulation. Currently, we are closely working with an experimental group in UCST, China to experimentally demonstrate analog quantum primacy. In addition, one can try to extend our analysis of diagnosing the computational complexity of the physical systems by studying their respective random matrix ensembles, for examples, the prethermalized regime at high frequency or a family of topological quantum phases. The extension of Chapter 3 where quantum primacy signatures related to anti-concentration are used to probe phases of matter is to see whether there are other

CHAPTER 5. CONCLUSION AND FUTURE WORK

signatures that can be easily measured and used as order parameters. Studying performances of analog quantum simulators as a function of phases in quantum machine learning in Chapter 4 can be extended to other contexts. For example, one can implement analog quantum simulators as variational hardware-efficient ansätze to solve binary optimization problems. In this context, one can also investigate quality of the obtained solutions as the function of phases.

Bibliography

- [1] R. P. Feynman, “Quantum mechanical computers”, *Optics news*, vol. 11, no. 2, pp. 11–20, 1985.
- [2] D. Deutsch, “Quantum theory, the church–turing principle and the universal quantum computer”, *Proceedings of the Royal Society of London. A. Mathematical and Physical Sciences*, vol. 400, no. 1818, pp. 97–117, 1985.
- [3] P. Benioff, “The computer as a physical system: A microscopic quantum mechanical hamiltonian model of computers as represented by turing machines”, *Journal of statistical physics*, vol. 22, no. 5, pp. 563–591, 1980.
- [4] R. P. Feynman, “Simulating physics with computers”, in *Feynman and computation*, CRC Press, 2018, pp. 133–153.
- [5] J. Preskill, “The physics of quantum information”, *arXiv preprint arXiv:2208.08064*, 2022.
- [6] A. A. Houck, H. E. Türeci, and J. Koch, “On-chip quantum simulation with superconducting circuits”, *Nature Physics*, vol. 8, p. 292, Apr. 2012. [Online]. Available: <http://dx.doi.org/10.1038/nphys2251>.
- [7] M. Kjaergaard, M. E. Schwartz, J. Braumüller, P. Krantz, J. I.-J. Wang, S. Gustavsson, and W. D. Oliver, “Superconducting qubits: Current state

BIBLIOGRAPHY

- of play”, *Annual Review of Condensed Matter Physics*, vol. 11, pp. 369–395, 2020.
- [8] R. Blatt and C. F. Roos, “Quantum simulations with trapped ions”, *Nature Physics*, vol. 8, p. 277, Apr. 2012. [Online]. Available: <http://dx.doi.org/10.1038/nphys2252>.
- [9] C. Monroe, W. C. Campbell, L. .-. Duan, Z. .-. Gong, A. V. Gorshkov, P. Hess, R. Islam, K. Kim, N. Linke, G. Pagano, P. Richerme, C. Senko, and N. Y. Yao, “Programmable Quantum Simulations of Spin Systems with Trapped Ions”,, arXiv: 1912.07845.
- [10] A. Eckardt, “Colloquium: Atomic quantum gases in periodically driven optical lattices”, *Rev. Mod. Phys.*, vol. 89, p. 011 004, 1 Mar. 2017. [Online]. Available: <https://link.aps.org/doi/10.1103/RevModPhys.89.011004>.
- [11] C. Gross and I. Bloch, “Quantum simulations with ultracold atoms in optical lattices”, *Science*, vol. 357, no. 6355, pp. 995–1001, 2017, ISSN: 0036-8075. [Online]. Available: <http://science.sciencemag.org/content/357/6355/995>.
- [12] F. Schäfer, T. Fukuhara, S. Sugawa, Y. Takasu, and Y. Takahashi, “Tools for quantum simulation with ultracold atoms in optical lattices”, *Nature Reviews Physics*, vol. 2, no. 8, pp. 411–425, 2020.
- [13] C. Noh and D. G. Angelakis, “Quantum simulations and many-body physics with light”, *Reports on Progress in Physics*, vol. 80, no. 1, p. 016 401, 2017.

BIBLIOGRAPHY

- [Online]. Available: <http://stacks.iop.org/0034-4885/80/i=1/a=016401>.
- [14] M. J. Hartmann, “Quantum simulation with interacting photons”, *Journal of Optics*, vol. 18, no. 10, p. 104005, 2016.
- [15] A. Browaeys and T. Lahaye, “Many-body physics with individually controlled rydberg atoms”, *Nature Physics*, vol. 16, no. 2, pp. 132–142, 2020.
- [16] T. Hensgens, T. Fujita, L. Janssen, X. Li, C. J. Van Diepen, C. Reichl, W. Wegscheider, S. Das Sarma, and L. M. K. Vandersypen, “Quantum simulation of a fermi–hubbard model using a semiconductor quantum dot array”, *Nature*, vol. 548, p. 70, Aug. 2017. [Online]. Available: <http://dx.doi.org/10.1038/nature23022>.
- [17] N. Y. Yao, L. Jiang, A. V. Gorshkov, P. C. Maurer, G. Giedke, J. I. Cirac, and M. D. Lukin, “Scalable architecture for a room temperature solid-state quantum information processor”, *Nature Communications*, vol. 3, p. 800, Apr. 2012. [Online]. Available: <http://dx.doi.org/10.1038/ncomms1788>.
- [18] G. Tosi, F. A. Mohiyaddin, V. Schmitt, S. Tenberg, R. Rahman, G. Klimeck, and A. Morello, “Silicon quantum processor with robust long-distance qubit couplings”, *Nature Communications*, vol. 8, no. 1, p. 450, 2017. [Online]. Available: <https://doi.org/10.1038/s41467-017-00378-x>.
- [19] J. Preskill, “Quantum Computing in the NISQ era and beyond”, *Quantum*, vol. 2, p. 79, Aug. 2018, ISSN: 2521-327X. [Online]. Available: <https://doi.org/10.22331/q-2018-08-06-79>.

BIBLIOGRAPHY

- [20] A. J. Daley, I. Bloch, C. Kokail, S. Flannigan, N. Pearson, M. Troyer, and P. Zoller, “Practical quantum advantage in quantum simulation”, *Nature*, vol. 607, no. 7920, pp. 667–676, 2022.
- [21] D. Hangleiter and J. Eisert, “Computational advantage of quantum random sampling”, *arXiv preprint arXiv:2206.04079*, 2022.
- [22] F. Arute, K. Arya, R. Babbush, D. Bacon, J. C. Bardin, R. Barends, R. Biswas, S. Boixo, F. G. S. L. Brandao, D. A. Buell, B. Burkett, Y. Chen, Z. Chen, B. Chiaro, R. Collins, W. Courtney, A. Dunsworth, E. Farhi, B. Foxen, A. Fowler, C. Gidney, M. Giustina, R. Graff, K. Guerin, S. Habegger, M. P. Harrigan, M. J. Hartmann, A. Ho, M. Hoffmann, T. Huang, T. S. Humble, S. V. Isakov, E. Jeffrey, Z. Jiang, D. Kafri, K. Kechedzhi, J. Kelly, P. V. Klimov, S. Knysh, A. Korotkov, F. Kostritsa, D. Landhuis, M. Lindmark, E. Lucero, D. Lyakh, S. Mandrà, J. R. McClean, M. McEwen, A. Megrant, X. Mi, K. Michielsen, M. Mohseni, J. Mutus, O. Naaman, M. Neeley, C. Neill, M. Y. Niu, E. Ostby, A. Petukhov, J. C. Platt, C. Quintana, E. G. Rieffel, P. Roushan, N. C. Rubin, D. Sank, K. J. Satzinger, V. Smelyanskiy, K. J. Sung, M. D. Trevithick, A. Vainsencher, B. Villalonga, T. White, Z. J. Yao, P. Yeh, A. Zalcman, H. Neven, and J. M. Martinis, “Quantum supremacy using a programmable superconducting processor”, *Nature*, vol. 574, no. 7779, pp. 505–510, Oct. 2019. [Online]. Available: <https://doi.org/10.1038/s41586-019-1666-5>.

BIBLIOGRAPHY

- [23] H.-Y. Huang, M. Broughton, J. Cotler, S. Chen, J. Li, M. Mohseni, H. Neven, R. Babbush, R. Kueng, J. Preskill, *et al.*, “Quantum advantage in learning from experiments”, *Science*, vol. 376, no. 6598, pp. 1182–1186, 2022.
- [24] D. Vallespin, K. Badcock, A. Da Ronch, M. White, P. Perfect, and M. Ghoreyshi, “Computational fluid dynamics framework for aerodynamic model assessment”, *Progress in Aerospace Sciences*, vol. 52, pp. 2–18, 2012.
- [25] T. Pang, “An introduction to computational physics”, American Association of Physics Teachers, 1999.
- [26] D. Noble, “The rise of computational biology”, *Nature Reviews Molecular Cell Biology*, vol. 3, no. 6, pp. 459–463, 2002.
- [27] R. Seydel and R. Seydel, “Tools for computational finance”, Springer, 2006, vol. 3.
- [28] F. Jensen, “Introduction to computational chemistry”, John wiley & sons, 2017.
- [29] J. Banks, “Discrete event system simulation”, Pearson Education India, 2005.
- [30] H. Goosse, P.-Y. BARRIAT, M.-F. LOUTRE, and V. ZUNZ, “Introduction to climate dynamics and climate modeling”, Centre de recherche sur la Terre et le climat Georges Lemaitre-UCLouvain, 2010.
- [31] S. H. Strogatz, “Nonlinear dynamics and chaos: with applications to physics, biology, chemistry, and engineering”, CRC press, 2018.

BIBLIOGRAPHY

- [32] J. Preskill, “Quantum computing and the entanglement frontier”, *arXiv preprint arXiv:1203.5813*, 2012.
- [33] S. McArdle, S. Endo, A. Aspuru-Guzik, S. C. Benjamin, and X. Yuan, “Quantum computational chemistry”, *Rev. Mod. Phys.*, vol. 92, p. 015 003, 1 Mar. 2020. [Online]. Available: <https://link.aps.org/doi/10.1103/RevModPhys.92.015003>.
- [34] J. I. Cirac and P. Zoller, “Goals and opportunities in quantum simulation”, *Nat Phys*, vol. 8, p. 264, Apr. 2012. [Online]. Available: <http://dx.doi.org/10.1038/nphys2275>.
- [35] I. M. Georgescu, S. Ashhab, and F. Nori, “Quantum simulation”, *Rev. Mod. Phys.*, vol. 86, pp. 153–185, 1 Mar. 2014. [Online]. Available: <https://link.aps.org/doi/10.1103/RevModPhys.86.153>.
- [36] S. Lloyd, “Universal quantum simulators”, *Science*, vol. 273, no. 5278, pp. 1073–1078, 1996.
- [37] A. Rubio-Abadal, M. Ippoliti, S. Hollerith, D. Wei, J. Rui, S. L. Sondhi, V. Khemani, C. Gross, and I. Bloch, “Floquet prethermalization in a bose-hubbard system”, *Phys. Rev. X*, vol. 10, p. 021 044, 2 May 2020. [Online]. Available: <https://link.aps.org/doi/10.1103/PhysRevX.10.021044>.
- [38] P. Bordia, H. Lüschen, U. Schneider, M. Knap, and I. Bloch, “Periodically driving a many-body localized quantum system”, *Nature Physics*, vol. 13, 460 EP -, Jan. 2017. [Online]. Available: <https://doi.org/10.1038/nphys4020>.

BIBLIOGRAPHY

- [39] P. Roushan, C. Neill, J. Tangpanitanon, V. M. Bastidas, A. Megrant, R. Barends, Y. Chen, Z. Chen, B. Chiaro, A. Dunsworth, A. Fowler, B. Foxen, M. Giustina, E. Jeffrey, J. Kelly, E. Lucero, J. Mutus, M. Neeley, C. Quintana, D. Sank, A. Vainsencher, J. Wenner, T. White, H. Neven, D. G. Angelakis, and J. Martinis, “Spectroscopic signatures of localization with interacting photons in superconducting qubits”, *Science*, vol. 358, no. 6367, pp. 1175–1179, Dec. 2017, ISSN: 0036-8075. [Online]. Available: <http://science.sciencemag.org/content/358/6367/1175>.
- [40] J.-Y. Choi, S. Hild, J. Zeiher, P. Schauß, A. Rubio-Abadal, T. Yefsah, V. Khemani, D. A. Huse, I. Bloch, and C. Gross, “Exploring the many-body localization transition in two dimensions”, *Science*, vol. 352, no. 6293, pp. 1547–1552, 2016, ISSN: 0036-8075. [Online]. Available: <http://science.sciencemag.org/content/352/6293/1547>.
- [41] G. Semeghini, H. Levine, A. Keesling, S. Ebadi, T. T. Wang, D. Bluvstein, R. Verresen, H. Pichler, M. Kalinowski, R. Samajdar, *et al.*, “Probing topological spin liquids on a programmable quantum simulator”, *Science*, vol. 374, no. 6572, pp. 1242–1247, 2021.
- [42] K. Satzinger, Y.-J. Liu, A. Smith, C. Knapp, M. Newman, C. Jones, Z. Chen, C. Quintana, X. Mi, A. Dunsworth, *et al.*, “Realizing topologically ordered states on a quantum processor”, *Science*, vol. 374, no. 6572, pp. 1237–1241, 2021.

BIBLIOGRAPHY

- [43] C. S. Chiu, G. Ji, A. Bohrdt, M. Xu, M. Knap, E. Demler, F. Grusdt, M. Greiner, and D. Greif, “String patterns in the doped hubbard model”, *Science*, vol. 365, no. 6450, pp. 251–256, 2019.
- [44] J. Koepsell, J. Vijayan, P. Sompet, F. Grusdt, T. A. Hilker, E. Demler, G. Salomon, I. Bloch, and C. Gross, “Imaging magnetic polarons in the doped fermi–hubbard model”, *Nature*, vol. 572, no. 7769, pp. 358–362, 2019.
- [45] P. W. Shor, “Algorithms for quantum computation: Discrete logarithms and factoring”, in *Proceedings 35th annual symposium on foundations of computer science*, Ieee, 1994, pp. 124–134.
- [46] L. K. Grover, “A fast quantum mechanical algorithm for database search”, in *Proceedings of the twenty-eighth annual ACM symposium on Theory of computing*, 1996, pp. 212–219.
- [47] A. W. Harrow, A. Hassidim, and S. Lloyd, “Quantum algorithm for linear systems of equations”, *Physical review letters*, vol. 103, no. 15, p. 150 502, 2009.
- [48] E. Bernstein and U. Vazirani, “Quantum complexity theory”, in *Proceedings of the twenty-fifth annual ACM symposium on Theory of computing*, 1993, pp. 11–20.
- [49] A. Vergis, K. Steiglitz, and B. Dickinson, “The complexity of analog computation”, *Mathematics and computers in simulation*, vol. 28, no. 2, pp. 91–113, 1986.

BIBLIOGRAPHY

- [50] A. W. Harrow and A. Montanaro, “Quantum computational supremacy”, *Nature*, vol. 549, p. 203, Sep. 2017. [Online]. Available: <https://doi.org/10.1038/nature23458>.
- [51] C. Gidney and M. Ekerå, “How to factor 2048 bit rsa integers in 8 hours using 20 million noisy qubits”, *Quantum*, vol. 5, p. 433, 2021.
- [52] Q. Zhu, S. Cao, F. Chen, M.-C. Chen, X. Chen, T.-H. Chung, H. Deng, Y. Du, D. Fan, M. Gong, *et al.*, “Quantum computational advantage via 60-qubit 24-cycle random circuit sampling”, *Science bulletin*, vol. 67, no. 3, pp. 240–245, 2022.
- [53] H.-S. Zhong, H. Wang, Y.-H. Deng, M.-C. Chen, L.-C. Peng, Y.-H. Luo, J. Qin, D. Wu, X. Ding, Y. Hu, P. Hu, X.-Y. Yang, W.-J. Zhang, H. Li, Y. Li, X. Jiang, L. Gan, G. Yang, L. You, Z. Wang, L. Li, N.-L. Liu, C.-Y. Lu, and J.-W. Pan, “Quantum computational advantage using photons”, *Science*, vol. 370, no. 6523, pp. 1460–1463, 2020. eprint: <https://www.science.org/doi/pdf/10.1126/science.abe8770>. [Online]. Available: <https://www.science.org/doi/abs/10.1126/science.abe8770>.
- [54] H.-S. Zhong, Y.-H. Deng, J. Qin, H. Wang, M.-C. Chen, L.-C. Peng, Y.-H. Luo, D. Wu, S.-Q. Gong, H. Su, Y. Hu, P. Hu, X.-Y. Yang, W.-J. Zhang, H. Li, Y. Li, X. Jiang, L. Gan, G. Yang, L. You, Z. Wang, L. Li, N.-L. Liu, J. J. Renema, C.-Y. Lu, and J.-W. Pan, “Phase-programmable gaussian boson sampling using stimulated squeezed light”, *Phys. Rev. Lett.*, vol. 127,

BIBLIOGRAPHY

- p. 180502, 18 Oct. 2021. [Online]. Available: <https://link.aps.org/doi/10.1103/PhysRevLett.127.180502>.
- [55] L. S. Madsen, F. Laudenbach, M. F. Askarani, F. Rortais, T. Vincent, J. F. F. Bulmer, F. M. Miatto, L. Neuhaus, L. G. Helt, M. J. Collins, A. E. Lita, T. Gerrits, S. W. Nam, V. D. Vaidya, M. Menotti, I. Dhand, Z. Vernon, N. Quesada, and J. Lavoie, “Quantum computational advantage with a programmable photonic processor”, *Nature*, vol. 606, no. 7912, pp. 75–81, 2022. [Online]. Available: <https://doi.org/10.1038/s41586-022-04725-x>.
- [56] A. P. Lund, M. J. Bremner, and T. C. Ralph, “Quantum sampling problems, bosonsampling and quantum supremacy”, *npj Quantum Information*, vol. 3, no. 1, p. 15, Apr. 2017. [Online]. Available: <https://doi.org/10.1038/s41534-017-0018-2>.
- [57] S. Boixo, S. V. Isakov, V. N. Smelyanskiy, R. Babbush, N. Ding, Z. Jiang, M. J. Bremner, J. M. Martinis, and H. Neven, “Characterizing quantum supremacy in near-term devices”, *Nature Physics*, vol. 14, no. 6, pp. 595–600, Apr. 2018. [Online]. Available: <https://doi.org/10.1038/s41567-018-0124-x>.
- [58] A. Bouland, B. Fefferman, C. Nirkhe, and U. Vazirani, “On the complexity and verification of quantum random circuit sampling”, *Nature Physics*, vol. 15, no. 2, pp. 159–163, Oct. 2019. [Online]. Available: <https://doi.org/10.1038/s41567-018-0318-2>.

BIBLIOGRAPHY

- [59] D. Shepherd and M. J. Bremner, “Temporally unstructured quantum computation”, *Proceedings of the Royal Society A: Mathematical, Physical and Engineering Sciences*, vol. 465, no. 2105, pp. 1413–1439, 2009.
- [60] M. J. Bremner, R. Jozsa, and D. J. Shepherd, “Classical simulation of commuting quantum computations implies collapse of the polynomial hierarchy”, *Proceedings of the Royal Society A: Mathematical, Physical and Engineering Sciences*, vol. 467, no. 2126, pp. 459–472, Aug. 2011.
- [61] M. J. Bremner, A. Montanaro, and D. J. Shepherd, “Average-Case Complexity Versus Approximate Simulation of Commuting Quantum Computations”, *Phys. Rev. Lett.*, vol. 117, no. 8, p. 080 501, Aug. 2016, Publisher: American Physical Society. [Online]. Available: <https://link.aps.org/doi/10.1103/PhysRevLett.117.080501> (visited on 06/09/2020).
- [62] S. Aaronson and A. Arkhipov, “The computational complexity of linear optics”, *Proceedings of the 43rd annual ACM Symposium on Theory of Computing, (STOC '11)*, pp. 333–342, Jun. 2011, ISSN: 0036-8075. [Online]. Available: <http://hdl.handle.net/1721.1/62805>.
- [63] A. Scott, “A linear-optical proof that the permanent is np-hard”, *Proceedings of the Royal Society A: Mathematical, Physical and Engineering Sciences*, vol. 467, p. 3393, 5 Jul. 2011.
- [64] D. J. Brod, E. F. Galvão, A. Crespi, R. Osellame, N. Spagnolo, and F. Sciarrino, “Photonic implementation of boson sampling: a review”, *Advanced*

BIBLIOGRAPHY

- Photonics*, vol. 1, no. 3, pp. 1–14, May 2019. [Online]. Available: <https://doi.org/10.1117/1.AP.1.3.034001>.
- [65] Y. Wu, W.-S. Bao, S. Cao, F. Chen, M.-C. Chen, X. Chen, T.-H. Chung, H. Deng, Y. Du, D. Fan, M. Gong, C. Guo, C. Guo, S. Guo, L. Han, L. Hong, H.-L. Huang, Y.-H. Huo, L. Li, N. Li, S. Li, Y. Li, F. Liang, C. Lin, J. Lin, H. Qian, D. Qiao, H. Rong, H. Su, L. Sun, L. Wang, S. Wang, D. Wu, Y. Xu, K. Yan, W. Yang, Y. Yang, Y. Ye, J. Yin, C. Ying, J. Yu, C. Zha, C. Zhang, H. Zhang, K. Zhang, Y. Zhang, H. Zhao, Y. Zhao, L. Zhou, Q. Zhu, C.-Y. Lu, C.-Z. Peng, X. Zhu, and J.-W. Pan, “Strong quantum computational advantage using a superconducting quantum processor”, *Phys. Rev. Lett.*, vol. 127, p. 180 501, 18 Oct. 2021. [Online]. Available: <https://link.aps.org/doi/10.1103/PhysRevLett.127.180501>.
- [66] D. Hangleiter, “Sampling and the complexity of nature”, *arXiv preprint arXiv:2012.07905*, 2020.
- [67] P. Mehta, M. Bukov, C.-H. Wang, A. G. Day, C. Richardson, C. K. Fisher, and D. J. Schwab, “A high-bias, low-variance introduction to machine learning for physicists”, *Physics reports*, vol. 810, pp. 1–124, 2019.
- [68] W. Rawat and Z. Wang, “Deep convolutional neural networks for image classification: A comprehensive review”, *Neural computation*, vol. 29, no. 9, pp. 2352–2449, 2017.
- [69] K. Chowdhary, “Natural language processing”, *Fundamentals of artificial intelligence*, pp. 603–649, 2020.

BIBLIOGRAPHY

- [70] M. F. Dixon, I. Halperin, and P. Bilokon, “Machine learning in Finance”, Springer, 2020, vol. 1406.
- [71] E. Alpaydin, “Introduction to machine learning”, Massachusetts Institute of Technology, 2020, ISBN: 9780262043793.
- [72] S. Levine, A. Kumar, G. Tucker, and J. Fu, “Offline reinforcement learning: Tutorial, review, and perspectives on open problems”, *arXiv preprint arXiv:2005.01643*, 2020.
- [73] V. Mnih, K. Kavukcuoglu, D. Silver, A. Graves, I. Antonoglou, D. Wierstra, and M. Riedmiller, “Playing atari with deep reinforcement learning”, *arXiv preprint arXiv:1312.5602*, 2013.
- [74] J. Biamonte, P. Wittek, N. Pancotti, P. Rebentrost, N. Wiebe, and S. Lloyd, “Quantum machine learning”, *Nature*, vol. 549, no. 7671, pp. 195–202, 2017. [Online]. Available: <https://www.nature.com/articles/nature23474>.
- [75] H.-Y. Huang, R. Kueng, and J. Preskill, “Information-theoretic bounds on quantum advantage in machine learning”, *Phys. Rev. Lett.*, vol. 126, p. 190 505, 19 May 2021. [Online]. Available: <https://link.aps.org/doi/10.1103/PhysRevLett.126.190505>.
- [76] D. Aharonov, J. Cotler, and X.-L. Qi, “Quantum algorithmic measurement”, *Nature Communications*, vol. 13, no. 1, pp. 1–9, 2022.
- [77] R. Sweke, J.-P. Seifert, D. Hangleiter, and J. Eisert, “On the Quantum versus Classical Learnability of Discrete Distributions”, *Quantum*, vol. 5, p. 417, Mar.

BIBLIOGRAPHY

- 2021, ISSN: 2521-327X. [Online]. Available: <https://doi.org/10.22331/q-2021-03-23-417>.
- [78] H.-Y. Huang, M. Broughton, M. Mohseni, R. Babbush, S. Boixo, H. Neven, and J. R. McClean, “Power of data in quantum machine learning”, *Nature Communications*, vol. 12, no. 1, pp. 1–9, 2021. [Online]. Available: <https://www.nature.com/articles/s41467-021-22539-9>.
- [79] J. Kübler, S. Buchholz, and B. Schölkopf, “The inductive bias of quantum kernels”, *Advances in Neural Information Processing Systems*, vol. 34, pp. 12 661–12 673, 2021. [Online]. Available: <https://proceedings.neurips.cc/paper/2021/hash/69adc1e107f7f7d035d7baf04342e1ca-Abstract.html>.
- [80] Y. Liu, S. Arunachalam, and K. Temme, “A rigorous and robust quantum speed-up in supervised machine learning”, *Nature Physics*, pp. 1–5, 2021. [Online]. Available: <https://www.nature.com/articles/s41567-021-01287-z>.
- [81] P. Rebentrost, M. Mohseni, and S. Lloyd, “Quantum support vector machine for big data classification”, *Physical review letters*, vol. 113, no. 13, p. 130 503, 2014.
- [82] S. Lloyd, M. Mohseni, and P. Rebentrost, “Quantum principal component analysis”, *Nature Physics*, vol. 10, no. 9, pp. 631–633, 2014.
- [83] N. Wiebe, D. Braun, and S. Lloyd, “Quantum algorithm for data fitting”, *Physical review letters*, vol. 109, no. 5, p. 050 505, 2012.

BIBLIOGRAPHY

- [84] S. Lloyd, M. Mohseni, and P. Rebentrost, “Quantum algorithms for supervised and unsupervised machine learning”, *arXiv preprint arXiv:1307.0411*, 2013.
- [85] M. Cerezo, A. Arrasmith, R. Babbush, S. C. Benjamin, S. Endo, K. Fujii, J. R. McClean, K. Mitarai, X. Yuan, L. Cincio, and P. J. Coles, “Variational quantum algorithms”, *Nature Reviews Physics*, vol. 3, no. 1, pp. 625–644, 2021. [Online]. Available: <https://www.nature.com/articles/s42254-021-00348-9>.
- [86] M. Schuld and N. Killoran, “Is quantum advantage the right goal for quantum machine learning?” *PRX Quantum*, vol. 3, p. 030 101, 3 Jul. 2022. [Online]. Available: <https://link.aps.org/doi/10.1103/PRXQuantum.3.030101>.
- [87] M. Benedetti, E. Lloyd, S. Sack, and M. Fiorentini, “Parameterized quantum circuits as machine learning models”, *Quantum Science and Technology*, vol. 4, no. 4, p. 043 001, Nov. 2019. [Online]. Available: <https://doi.org/10.1088/2F2058-9565%2Fab4eb5>.
- [88] M. Schuld, R. Sweke, and J. J. Meyer, “Effect of data encoding on the expressive power of variational quantum-machine-learning models”, *Physical Review A*, vol. 103, no. 3, p. 032 430, 2021.
- [89] A. Pérez-Salinas, A. Cervera-Lierta, E. Gil-Fuster, and J. I. Latorre, “Data re-uploading for a universal quantum classifier”, *Quantum*, vol. 4, p. 226, 2020.
- [90] N. Killoran, T. R. Bromley, J. M. Arrazola, M. Schuld, N. Quesada, and S. Lloyd, “Continuous-variable quantum neural networks”, *Phys. Rev. Research*,

BIBLIOGRAPHY

- vol. 1, p. 033063, 3 Oct. 2019. [Online]. Available: <https://link.aps.org/doi/10.1103/PhysRevResearch.1.033063>.
- [91] Y. Du, M.-H. Hsieh, T. Liu, and D. Tao, “The Expressive Power of Parameterized Quantum Circuits”,, arXiv: [1810.11922](https://arxiv.org/abs/1810.11922).
- [92] B. Coyle, D. Mills, V. Danos, and E. Kashefi, “The Born Supremacy: Quantum Advantage and Training of an Ising Born Machine”,, arXiv: [1904.02214](https://arxiv.org/abs/1904.02214).
- [93] S. Sim, P. D. Johnson, and A. Aspuru-Guzik, “Expressibility and entangling capability of parameterized quantum circuits for hybrid quantum-classical algorithms”, *Advanced Quantum Technologies*, vol. 2, no. 12, p. 1900070, 2019.
- [94] J. R. McClean, S. Boixo, V. N. Smelyanskiy, R. Babbush, and H. Neven, “Barren plateaus in quantum neural network training landscapes”, *Nature Communications*, vol. 9, no. 1, p. 4812, Nov. 2018. [Online]. Available: <https://doi.org/10.1038/s41467-018-07090-4>.
- [95] M. Cerezo, A. Sone, T. Volkoff, L. Cincio, and P. J. Coles, “Cost function dependent barren plateaus in shallow parametrized quantum circuits”, *Nature Communications*, vol. 12, no. 1, pp. 1–12, 2021. [Online]. Available: <https://www.nature.com/articles/s41467-021-21728-w>.
- [96] M. Larocca, P. Czarnik, K. Sharma, G. Muraleedharan, P. J. Coles, and M. Cerezo, “Diagnosing barren plateaus with tools from quantum optimal control”, *arXiv preprint arXiv:2105.14377*, 2021. [Online]. Available: <https://arxiv.org/abs/2105.14377>.

BIBLIOGRAPHY

- [97] Z. Holmes, K. Sharma, M. Cerezo, and P. J. Coles, “Connecting ansatz expressibility to gradient magnitudes and barren plateaus”, *PRX Quantum*, vol. 3, p. 010313, 1 Jan. 2022. [Online]. Available: <https://link.aps.org/doi/10.1103/PRXQuantum.3.010313>.
- [98] S. Thanasilp, S. Wang, N. A. Nghiem, P. J. Coles, and M. Cerezo, “Subtleties in the trainability of quantum machine learning models”, *arXiv preprint arXiv:2110.14753*, 2021. [Online]. Available: <https://arxiv.org/abs/2110.14753>.
- [99] M. Schuld, “Supervised quantum machine learning models are kernel methods”, *arXiv preprint arXiv:2101.11020*, 2021. [Online]. Available: <https://arxiv.org/abs/2101.11020>.
- [100] S. Thanasilp, S. Wang, M. Cerezo, and Z. Holmes, “Exponential concentration and untrainability in quantum kernel methods”, *arXiv preprint arXiv:2208.11060*, 2022. [Online]. Available: <https://arxiv.org/abs/2208.11060>.
- [101] C. O. Marrero, M. Kieferová, and N. Wiebe, “Entanglement-induced barren plateaus”, *PRX Quantum*, vol. 2, no. 4, p. 040316, 2021.
- [102] S. Wang, E. Fontana, M. Cerezo, K. Sharma, A. Sone, L. Cincio, and P. J. Coles, “Noise-induced barren plateaus in variational quantum algorithms”, *Nature Communications*, vol. 12, no. 1, pp. 1–11, 2021. [Online]. Available: <https://www.nature.com/articles/s41467-021-27045-6>.

BIBLIOGRAPHY

- [103] I. Cong, S. Choi, and M. D. Lukin, “Quantum convolutional neural networks”, *Nature Physics*, pp. 1–6, 2019.
- [104] A. Pesah, M. Cerezo, S. Wang, T. Volkoff, A. T. Sornborger, and P. J. Coles, “Absence of barren plateaus in quantum convolutional neural networks”, *Physical Review X*, vol. 11, no. 4, p. 041 011, 2021. [Online]. Available: <https://journals.aps.org/prx/abstract/10.1103/PhysRevX.11.041011>.
- [105] A. Abbas, D. Sutter, C. Zoufal, A. Lucchi, A. Figalli, and S. Woerner, “The power of quantum neural networks”, *Nature Computational Science*, vol. 1, no. 6, pp. 403–409, 2021.
- [106] M. Larocca, F. Sauvage, F. M. Sbahi, G. Verdon, P. J. Coles, and M. Cerezo, “Group-invariant quantum machine learning”, *arXiv preprint arXiv:2205.02261*, 2022. [Online]. Available: <https://arxiv.org/abs/2205.02261>.
- [107] J. J. Meyer, M. Mularski, E. Gil-Fuster, A. A. Mele, F. Arzani, A. Wilms, and J. Eisert, “Exploiting symmetry in variational quantum machine learning”, *arXiv preprint arXiv:2205.06217*, 2022. [Online]. Available: <https://arxiv.org/abs/2205.06217>.
- [108] J. B. Spring, B. J. Metcalf, P. C. Humphreys, W. S. Kolthammer, X.-M. Jin, M. Barbieri, A. Datta, N. Thomas-Peter, N. K. Langford, D. Kundys, J. C. Gates, B. J. Smith, P. G. R. Smith, and I. A. Walmsley, “Boson sampling on a photonic chip”, *Science*, vol. 339, no. 6121, pp. 798–801, 2013, ISSN: 0036-8075. [Online]. Available: <http://science.sciencemag.org/content/339/6121/798>.

BIBLIOGRAPHY

- [109] M. A. Broome, A. Fedrizzi, S. Rahimi-Keshari, J. Dove, S. Aaronson, T. C. Ralph, and A. G. White, “Photonic boson sampling in a tunable circuit”, *Science*, vol. 339, no. 6121, pp. 794–798, 2013, ISSN: 0036-8075. [Online]. Available: <https://science.sciencemag.org/content/339/6121/794>.
- [110] M. Tillmann, B. Dakić, R. Heilmann, S. Nolte, A. Szameit, and P. Walther, “Experimental boson sampling”, *Nature Photonics*, vol. 7, p. 540, May 2013. [Online]. Available: <https://doi.org/10.1038/nphoton.2013.102>.
- [111] A. Crespi, R. Osellame, R. Ramponi, D. J. Brod, E. F. Galvão, N. Spagnolo, C. Vitelli, E. Maiorino, P. Mataloni, and F. Sciarrino, “Integrated multimode interferometers with arbitrary designs for photonic boson sampling”, *Nature Photonics*, vol. 7, p. 545, May 2013. [Online]. Available: <https://doi.org/10.1038/nphoton.2013.112>.
- [112] H. Wang, J. Qin, X. Ding, M.-C. Chen, S. Chen, X. You, Y.-M. He, X. Jiang, L. You, Z. Wang, C. Schneider, J. J. Renema, S. Höfling, C.-Y. Lu, and J.-W. Pan, “Boson sampling with 20 input photons and a 60-mode interferometer in a 10^{14} -dimensional hilbert space”, *Phys. Rev. Lett.*, vol. 123, p. 250 503, 25 Dec. 2019. [Online]. Available: <https://link.aps.org/doi/10.1103/PhysRevLett.123.250503>.
- [113] C. Neill, P. Roushan, K. Kechedzhi, S. Boixo, S. V. Isakov, V. Smelyanskiy, A. Megrant, B. Chiaro, A. Dunsworth, K. Arya, R. Barends, B. Burkett, Y. Chen, Z. Chen, A. Fowler, B. Foxen, M. Giustina, R. Graff, E. Jeffrey, T. Huang, J. Kelly, P. Klimov, E. Lucero, J. Mutus, M. Neeley, C. Quintana, D.

BIBLIOGRAPHY

- Sank, A. Vainsencher, J. Wenner, T. C. White, H. Neven, and J. M. Martinis, “A blueprint for demonstrating quantum supremacy with superconducting qubits”, *Science*, vol. 360, no. 6385, pp. 195–199, Apr. 2018, ISSN: 0036-8075.
- [114] P. Hauke, F. M. Cucchietti, L. Tagliacozzo, I. Deutsch, and M. Lewenstein, “Can one trust quantum simulators?” *Reports on Progress in Physics*, vol. 75, no. 8, p. 082401, 2012. [Online]. Available: <http://stacks.iop.org/0034-4885/75/i=8/a=082401>.
- [115] T. H. Johnson, S. R. Clark, and D. Jaksch, “What is a quantum simulator?” *EPJ Quantum Technology*, vol. 1, no. 1, p. 10, Jul. 2014, ISSN: 2196-0763. [Online]. Available: <https://doi.org/10.1140/epjqt10>.
- [116] J. Bermejo-Vega, D. Hangleiter, M. Schwarz, R. Raussendorf, and J. Eisert, “Architectures for quantum simulation showing a quantum speedup”, *Phys. Rev. X*, vol. 8, p. 021010, 2 Apr. 2018. [Online]. Available: <https://link.aps.org/doi/10.1103/PhysRevX.8.021010>.
- [117] X. Gao, S.-T. Wang, and L.-M. Duan, “Quantum supremacy for simulating a translation-invariant ising spin model”, *Phys. Rev. Lett.*, vol. 118, p. 040502, 4 Jan. 2017. [Online]. Available: <https://link.aps.org/doi/10.1103/PhysRevLett.118.040502>.
- [118] L. Novo, J. Bermejo-Vega, and R. Garcia-Patrón, “Quantum advantage from energy measurements of many-body quantum systems”, *arXiv e-prints*, arXiv:1912.06608, arXiv:1912.06608, Dec. 2019. arXiv: [1912.06608](https://arxiv.org/abs/1912.06608) [quant-ph].

BIBLIOGRAPHY

- [119] L. D’Alessio, Y. Kafri, A. Polkovnikov, and M. Rigol, “From quantum chaos and eigenstate thermalization to statistical mechanics and thermodynamics”, *Advances in Physics*, vol. 65, no. 3, pp. 239–362, 2016. [Online]. Available: <https://doi.org/10.1080/00018732.2016.1198134>.
- [120] L. D’Alessio and M. Rigol, “Long-time behavior of isolated periodically driven interacting lattice systems”, *Phys. Rev. X*, vol. 4, p. 041048, 4 Dec. 2014. [Online]. Available: <https://link.aps.org/doi/10.1103/PhysRevX.4.041048>.
- [121] K. Singh, C. J. Fujiwara, Z. A. Geiger, E. Q. Simmons, M. Lipatov, A. Cao, P. Dotti, S. V. Rajagopal, R. Senaratne, T. Shimasaki, M. Heyl, A. Eckardt, and D. M. Weld, “Quantifying and controlling prethermal nonergodicity in interacting floquet matter”, *Phys. Rev. X*, vol. 9, p. 041021, 4 Oct. 2019. [Online]. Available: <https://link.aps.org/doi/10.1103/PhysRevX.9.041021>.
- [122] K. Wintersperger, M. Bukov, J. Näger, S. Lellouch, E. Demler, U. Schneider, I. Bloch, N. Goldman, and M. Aidelsburger, “Parametric instabilities of interacting bosons in periodically driven 1d optical lattices”, *Phys. Rev. X*, vol. 10, p. 011030, 1 Feb. 2020. [Online]. Available: <https://link.aps.org/doi/10.1103/PhysRevX.10.011030>.
- [123] C. Monroe, W. C. Campbell, L. Duan, Z.-X. Gong, A. V. Gorshkov, P. Hess, R. Islam, K. Kim, N. Linke, G. Pagano, P. Richerme, C. Senko, and N. Yao,

BIBLIOGRAPHY

- “Programmable quantum simulations of spin systems with trapped ions”,
arXiv preprint, arXiv:1912.07845, 2019.
- [124] J. S. Otterbach, R. Manenti, N. Alidoust, A. Bestwick, M. Block, B. Bloom, S. Caldwell, N. Didier, E. Schuyler Fried, S. Hong, P. Karalekas, C. B. Osborn, A. Papageorge, E. C. Peterson, G. Prawiroatmodjo, N. Rubin, C. A. Ryan, D. Scarabelli, M. Scheer, E. A. Sete, P. Sivarajah, R. S. Smith, A. Staley, N. Tezak, W. J. Zeng, A. Hudson, B. R. Johnson, M. Reagor, M. P. da Silva, and C. Rigetti, “Unsupervised Machine Learning on a Hybrid Quantum Computer”,, arXiv: **1712.05771**.
- [125] J. Eisert, F. M., and C. Gogolin, “Quantum many-body systems out of equilibrium”, *Nature Physics*, no. 11, pp. 124–130, 2015.
- [126] J. Eisert, D. Hangleiter, N. Walk, I. Roth, D. Markham, R. Parekh, U. Chabaud, and E. Kashefi, “Quantum certification and benchmarking”, *Nature Reviews Physics*, vol. 2, no. 7, pp. 382–390, 2020. [Online]. Available: <https://doi.org/10.1038/s42254-020-0186-4>.
- [127] D. Hangleiter, J. Bermejo-Vega, M. Schwarz, and J. Eisert, “Anticoncentration theorems for schemes showing a quantum speedup”, *Quantum*, vol. 2, p. 65, May 2018, ISSN: 2521-327X. [Online]. Available: <https://doi.org/10.22331/q-2018-05-22-65>.
- [128] L. Stockmeyer, “On approximation algorithms for $\# p$ ”, *SIAM Journal on Computing*, vol. 14, no. 4, pp. 849–861, 1985. eprint: <https://doi.org/10.1137/0214060>. [Online]. Available: <https://doi.org/10.1137/0214060>.

BIBLIOGRAPHY

- [129] L. A. Goldberg and H. Guo, “The complexity of approximating complex-valued ising and tutte partition functions”, *computational complexity*, vol. 26, no. 4, pp. 765–833, 2017.
- [130] F. Haake, “Quantum Signatures of Chaos”, Springer International Publishing, US, 2010, ISBN: 978-3-642-05427-3.
- [131] D. A. Roberts and B. Yoshida, “Chaos and complexity by design”, *Journal of High Energy Physics*, vol. 2017, no. 4, p. 121, 2017. [Online]. Available: [https://doi.org/10.1007/JHEP04\(2017\)121](https://doi.org/10.1007/JHEP04(2017)121).
- [132] A. W. Harrow and R. A. Low, “Random quantum circuits are approximate 2-designs”, *Communications in Mathematical Physics*, vol. 291, no. 1, pp. 257–302, Oct. 2009, ISSN: 1432-0916.
- [133] N. R. Jones, “Chaos and randomness in strongly-interacting quantum systems”, *Dissertation (Ph.D.)*, California Institute of Technology., 2018.
- [134] M. K. Simon, “Probability Distributions Involving Gaussian Random Variables”, Springer, Boston, MA, 2002, ISBN: 978-0-387-34657-1.
- [135] H. Kim, T. N. Ikeda, and D. A. Huse, “Testing whether all eigenstates obey the eigenstate thermalization hypothesis”, *Phys. Rev. E*, vol. 90, p. 052105, 5 Nov. 2014. [Online]. Available: <https://link.aps.org/doi/10.1103/PhysRevE.90.052105>.
- [136] A. Lazarides, A. Das, and R. Moessner, “Equilibrium states of generic quantum systems subject to periodic driving”, *Phys. Rev. E*, vol. 90, p. 012110,

BIBLIOGRAPHY

- 1 Jul. 2014. [Online]. Available: <https://link.aps.org/doi/10.1103/PhysRevE.90.012110>.
- [137] T. Mori, T. Kuwahara, and K. Saito, “Rigorous bound on energy absorption and generic relaxation in periodically driven quantum systems”, *Phys. Rev. Lett.*, vol. 116, p. 120401, 12 Mar. 2016. [Online]. Available: <https://link.aps.org/doi/10.1103/PhysRevLett.116.120401>.
- [138] D. A. Abanin, E. Altman, I. Bloch, and M. Serbyn, “Colloquium: Many-body localization, thermalization, and entanglement”, *Rev. Mod. Phys.*, vol. 91, p. 021001, 2 May 2019. [Online]. Available: <https://link.aps.org/doi/10.1103/RevModPhys.91.021001>.
- [139] T. Mori, T. N. Ikeda, E. Kaminishi, and M. Ueda, “Thermalization and prethermalization in isolated quantum systems: A theoretical overview”, *Journal of Physics B: Atomic, Molecular and Optical Physics*, vol. 51, no. 11, p. 112001, May 2018. [Online]. Available: <https://doi.org/10.1088%2F1361-6455%2Faabcdf>.
- [140] S. Thanasilp, J. Tangpanitanon, M.-A. Lemonde, N. Dangniam, and D. G. Angelakis, “Quantum supremacy and quantum phase transitions”, *Phys. Rev. B*, vol. 103, p. 165132, 16 Apr. 2021. [Online]. Available: <https://link.aps.org/doi/10.1103/PhysRevB.103.165132>.
- [141] H.-S. Zhong, H. Wang, Y.-H. Deng, M.-C. Chen, L.-C. Peng, Y.-H. Luo, J. Qin, D. Wu, X. Ding, Y. Hu, P. Hu, X.-Y. Yang, W.-J. Zhang, H. Li, Y. Li, X. Jiang, L. Gan, G. Yang, L. You, Z. Wang, L. Li, N.-L. Liu, C.-Y. Lu, and J.-W.

BIBLIOGRAPHY

- Pan, “Quantum computational advantage using photons”, *Science*, vol. 370, no. 6523, pp. 1460–1463, Dec. 2020, ISSN: 0036-8075. [Online]. Available: <https://science.sciencemag.org/content/370/6523/1460>.
- [142] B. Coyle, D. Mills, V. Danos, and E. Kashefi, “The born supremacy: Quantum advantage and training of an ising born machine”, *npj Quantum Information*, vol. 6, no. 1, p. 60, Jul. 2020. [Online]. Available: <https://doi.org/10.1038/s41534-020-00288-9>.
- [143] R. Movassagh, “Quantum supremacy and random circuits”,, arXiv: **1909.06210**.
- [144] J. Richter and A. Pal, “Simulating hydrodynamics on nisq devices with random circuits”,, arXiv: **2012.02795**.
- [145] E. Knill, D. Leibfried, R. Reichle, J. Britton, R. B. Blakestad, J. D. Jost, C. Langer, R. Ozeri, S. Seidelin, and D. J. Wineland, “Randomized benchmarking of quantum gates”, *Phys. Rev. A*, vol. 77, p. 012307, 1 Jan. 2008. [Online]. Available: <https://link.aps.org/doi/10.1103/PhysRevA.77.012307>.
- [146] J. Emerson, Y. S. Weinstein, M. Saraceno, S. Lloyd, and D. G. Cory, “Pseudo-random unitary operators for quantum information processing”, *Science*, vol. 302, no. 5653, pp. 2098–2100, Dec. 2003, ISSN: 0036-8075. [Online]. Available: <https://science.sciencemag.org/content/302/5653/2098>.
- [147] Y. Cao, J. Romero, J. P. Olson, M. Degroote, P. D. Johnson, M. Kieferová, I. D. Kivlichan, T. Menke, B. Peropadre, N. P. D. Sawaya, S. Sim, L. Veis, and A. Aspuru-Guzik, “Quantum chemistry in the age of quantum computing”,

BIBLIOGRAPHY

- Chemical Reviews*, vol. 119, no. 19, pp. 10 856–10 915, Oct. 2019. [Online]. Available: <https://doi.org/10.1021/acs.chemrev.8b00803>.
- [148] B. Bauer, S. Bravyi, M. Motta, and G. Kin-Lic Chan, “Quantum algorithms for quantum chemistry and quantum materials science”, *Chemical Reviews*, vol. 120, no. 22, pp. 12 685–12 717, Nov. 2020. [Online]. Available: <https://doi.org/10.1021/acs.chemrev.9b00829>.
- [149] M. Ippoliti, K. Kechedzhi, R. Moessner, S. L. Sondhi, and V. Khemani, “Many-body physics in the nisq era: Quantum programming a discrete time crystal”,, arXiv: [2007.11602](https://arxiv.org/abs/2007.11602).
- [150] M. Benedetti, E. Lloyd, S. Sack, and M. Fiorentini, “Parameterized quantum circuits as machine learning models”, *Quantum Science and Technology*, vol. 4, no. 4, p. 043 001, Nov. 2019. [Online]. Available: <https://doi.org/10.1088/2F2058-9565%2Fab4eb5>.
- [151] J. Tangpanitanon, S. Thanasilp, M.-A. Lemonde, N. Dangiam, and D. G. Angelakis, “Quantum supremacy in driven quantum many-body systems”, *arXiv preprint arXiv:2002.11946*, 2020. [Online]. Available: <https://arxiv.org/abs/2002.11946>.
- [152] P. Ponte, A. Chandran, Z. Papić, and D. A. Abanin, “Periodically driven ergodic and many-body localized quantum systems”, *Annals of Physics*, vol. 353, pp. 196–204, Feb. 2015, ISSN: 0003-4916. [Online]. Available: <http://www.sciencedirect.com/science/article/pii/S0003491614003212>.

BIBLIOGRAPHY

- [153] L. D’Alessio and A. Polkovnikov, “Many-body energy localization transition in periodically driven systems”, *Annals of Physics*, vol. 333, pp. 19–33, Jun. 2013, ISSN: 0003-4916. [Online]. Available: <http://www.sciencedirect.com/science/article/pii/S0003491613000389>.
- [154] P. Ponte, Z. Papić, F. Huveneers, and D. A. Abanin, “Many-body localization in periodically driven systems”, *Phys. Rev. Lett.*, vol. 114, p. 140401, 14 Apr. 2015. [Online]. Available: <https://link.aps.org/doi/10.1103/PhysRevLett.114.140401>.
- [155] A. Lazarides, A. Das, and R. Moessner, “Fate of many-body localization under periodic driving”, *Phys. Rev. Lett.*, vol. 115, p. 030402, 3 Jul. 2015. [Online]. Available: <https://link.aps.org/doi/10.1103/PhysRevLett.115.030402>.
- [156] D. A. Abanin, W. D. Roeck, and F. Huveneers, “Theory of many-body localization in periodically driven systems”, *Annals of Physics*, vol. 372, pp. 1–11, Sep. 2016, ISSN: 0003-4916. [Online]. Available: <http://www.sciencedirect.com/science/article/pii/S000349161630001X>.
- [157] M. Friesdorf, A. H. Werner, W. Brown, V. B. Scholz, and J. Eisert, “Many-body localization implies that eigenvectors are matrix-product states”, *Phys. Rev. Lett.*, vol. 114, p. 170505, 17 May 2015. [Online]. Available: <https://link.aps.org/doi/10.1103/PhysRevLett.114.170505>.
- [158] A. Chandran, J. Carrasquilla, I. H. Kim, D. A. Abanin, and G. Vidal, “Spectral tensor networks for many-body localization”, *Phys. Rev. B*, vol. 92,

BIBLIOGRAPHY

- p. 024 201, 2 Jul. 2015. [Online]. Available: <https://link.aps.org/doi/10.1103/PhysRevB.92.024201>.
- [159] T. B. Wahl, A. Pal, and S. H. Simon, “Efficient representation of fully many-body localized systems using tensor networks”, *Phys. Rev. X*, vol. 7, p. 021 018, 2 May 2017. [Online]. Available: <https://link.aps.org/doi/10.1103/PhysRevX.7.021018>.
- [160] J. Tangpanitanon, S. Thanasilp, N. Dangniam, M.-A. Lemonde, and D. G. Angelakis, “Expressibility and trainability of parametrized analog quantum systems for machine learning applications”, *Phys. Rev. Research*, vol. 2, p. 043 364, 4 Dec. 2020. [Online]. Available: <https://link.aps.org/doi/10.1103/PhysRevResearch.2.043364>.
- [161] S. Kullback and R. A. Leibler, “On information and sufficiency”, *Ann. Math. Statist.*, vol. 22, no. 1, pp. 79–86, Mar. 1951. [Online]. Available: <https://doi.org/10.1214/aoms/1177729694>.
- [162] C. E. Porter and R. G. Thomas, “Fluctuations of nuclear reaction widths”, *Phys. Rev.*, vol. 104, pp. 483–491, 2 Oct. 1956. [Online]. Available: <https://link.aps.org/doi/10.1103/PhysRev.104.483>.
- [163] L. D’Alessio, Y. Kafri, A. Polkovnikov, and M. Rigol, “From quantum chaos and eigenstate thermalization to statistical mechanics and thermodynamics”, *Advances in Physics*, vol. 65, no. 3, pp. 239–362, Jun. 2016. [Online]. Available: <https://doi.org/10.1080/00018732.2016.1198134>.

BIBLIOGRAPHY

- [164] N. Schuch, M. M. Wolf, F. Verstraete, and J. I. Cirac, “Entropy scaling and simulability by matrix product states”, *Phys. Rev. Lett.*, vol. 100, p. 030 504, 3 Jan. 2008. [Online]. Available: <https://link.aps.org/doi/10.1103/PhysRevLett.100.030504>.
- [165] A. Rubio-Abadal, J.-y. Choi, J. Zeiher, S. Hollerith, J. Rui, I. Bloch, and C. Gross, “Many-body delocalization in the presence of a quantum bath”, *Phys. Rev. X*, vol. 9, p. 041 014, 4 Oct. 2019. [Online]. Available: <https://link.aps.org/doi/10.1103/PhysRevX.9.041014>.
- [166] T. Kohlert, S. Scherg, X. Li, H. P. Lüschen, S. Das Sarma, I. Bloch, and M. Aidelsburger, “Observation of many-body localization in a one-dimensional system with a single-particle mobility edge”, *Phys. Rev. Lett.*, vol. 122, p. 170 403, 17 May 2019. [Online]. Available: <https://link.aps.org/doi/10.1103/PhysRevLett.122.170403>.
- [167] B. Chiaro, C. Neill, A. Bohrdt, M. Filippone, F. Arute, K. Arya, R. Babbush, D. Bacon, J. Bardin, R. Barends, S. Boixo, D. Buell, B. Burkett, Y. Chen, Z. Chen, R. Collins, A. Dunsworth, E. Farhi, A. Fowler, B. Foxen, C. Gidney, M. Giustina, M. Harrigan, T. Huang, S. Isakov, E. Jeffrey, Z. Jiang, D. Kafri, K. Kechedzhi, J. Kelly, P. Klimov, A. Korotkov, F. Kostritsa, D. Landhuis, E. Lucero, J. McClean, X. Mi, A. Megrant, M. Mohseni, J. Mutus, M. McEwen, O. Naaman, M. Neeley, M. Niu, A. Petukhov, C. Quintana, N. Rubin, D. Sank, K. Satzinger, A. Vainsencher, T. White, Z. Yao, P. Yeh, A. Zalcman, V. Smelyanskiy, H. Neven, S. Gopalakrishnan, D. Abanin, M. Knap,

BIBLIOGRAPHY

- J. Martinis, and P. Roushan, “Direct measurement of non-local interactions in the many-body localized phase”,, arXiv: **1910.06024**.
- [168] A. Russomanno, G. E. Santoro, and R. Fazio, “Entanglement entropy in a periodically driven ising chain”, *Journal of Statistical Mechanics: Theory and Experiment*, vol. 2016, no. 7, p. 073 101, Jul. 2016. [Online]. Available: <https://doi.org/10.1088%2F1742-5468%2F2016%2F07%2F073101>.
- [169] U. Schollwöck, “The density-matrix renormalization group in the age of matrix product states”, *Annals of Physics*, vol. 326, no. 1, pp. 96–192, Jan. 2011, Special Issue, ISSN: 0003-4916. [Online]. Available: <http://www.sciencedirect.com/science/article/pii/S0003491610001752>.
- [170] J. H. Bardarson, F. Pollmann, and J. E. Moore, “Unbounded growth of entanglement in models of many-body localization”, *Phys. Rev. Lett.*, vol. 109, p. 017 202, 1 Jul. 2012. [Online]. Available: <https://link.aps.org/doi/10.1103/PhysRevLett.109.017202>.
- [171] M. Serbyn, Z. Papić, and D. A. Abanin, “Universal slow growth of entanglement in interacting strongly disordered systems”, *Phys. Rev. Lett.*, vol. 110, p. 260 601, 26 Jun. 2013. [Online]. Available: <https://link.aps.org/doi/10.1103/PhysRevLett.110.260601>.
- [172] J.-Y. Choi, S. Hild, J. Zeiher, P. Schauß, A. Rubio-Abadal, T. Yefsah, V. Khemani, D. A. Huse, I. Bloch, and C. Gross, “Exploring the many-body localization transition in two dimensions”, *Science*, vol. 352, no. 6293, pp. 1547–

BIBLIOGRAPHY

- 1552, Jun. 2016, ISSN: 0036-8075. [Online]. Available: <http://science.sciencemag.org/content/352/6293/1547>.
- [173] I. Q. team. Retrieved from <https://quantum-computing.ibm.com>, “Ibmq”, 2020.
- [174] F. Schäfer, T. Fukuhara, S. Sugawa, Y. Takasu, and Y. Takahashi, “Tools for quantum simulation with ultracold atoms in optical lattices”, *Nature Reviews Physics*, vol. 2, no. 8, pp. 411–425, Jul. 2020. [Online]. Available: <https://doi.org/10.1038/s42254-020-0195-3>.
- [175] G. Wendin, “Quantum information processing with superconducting circuits: A review”, *Reports on Progress in Physics*, vol. 80, no. 10, p. 106 001, Sep. 2017. [Online]. Available: <https://doi.org/10.1088/1361-6633/aa7e1a>.
- [176] M. Morgado and S. Whitlock, “Quantum simulation and computing with rydberg-interacting qubits”,, arXiv: 2011.03031.
- [177] D. N. Page, “Average entropy of a subsystem”, *Phys. Rev. Lett.*, vol. 71, pp. 1291–1294, 9 Aug. 1993. [Online]. Available: <https://link.aps.org/doi/10.1103/PhysRevLett.71.1291>.
- [178] W. Magnus, “On the exponential solution of differential equations for a linear operator”, *Communications on Pure and Applied Mathematics*, vol. 7, no. 4, pp. 649–673, Nov. 1954. [Online]. Available: <https://onlinelibrary.wiley.com/doi/abs/10.1002/cpa.3160070404>.
- [179] M. Bukov, L. D’Alessio, and A. Polkovnikov, “Universal high-frequency behavior of periodically driven systems: From dynamical stabilization to

BIBLIOGRAPHY

- floquet engineering”, *Advances in Physics*, vol. 64, no. 2, pp. 139–226, Sep. 2015.
- [180] S. Blanes, F. Casas, J. Oteo, and J. Ros, “The magnus expansion and some of its applications”, *Physics Reports*, vol. 470, no. 5, pp. 151–238, Jan. 2009, ISSN: 0370-1573. [Online]. Available: <http://www.sciencedirect.com/science/article/pii/S0370157308004092>.
- [181] J. Schachenmayer, B. P. Lanyon, C. F. Roos, and A. J. Daley, “Entanglement growth in quench dynamics with variable range interactions”, *Phys. Rev. X*, vol. 3, p. 031 015, 3 Sep. 2013. [Online]. Available: <https://link.aps.org/doi/10.1103/PhysRevX.3.031015>.
- [182] R. Islam, R. Ma, P. M. Preiss, M. Eric Tai, A. Lukin, M. Rispoli, and M. Greiner, “Measuring entanglement entropy in a quantum many-body system”, *Nature*, vol. 528, no. 7580, pp. 77–83, Dec. 2015. [Online]. Available: <https://doi.org/10.1038/nature15750>.
- [183] N. Moll, P. Barkoutsos, L. S. Bishop, J. M. Chow, A. Cross, D. J. Egger, S. Filipp, A. Fuhrer, J. M. Gambetta, M. Ganzhorn, A. Kandala, A. Mezza-capo, P. Müller, W. Riess, G. Salis, J. Smolin, I. Tavernelli, and K. Temme, “Quantum optimization using variational algorithms on near-term quantum devices”, *Quantum Science and Technology*, vol. 3, no. 3, p. 030 503, Jun. 2018. [Online]. Available: <https://doi.org/10.1088%2F2058-9565%2Faab822>.

BIBLIOGRAPHY

- [184] J. R. McClean, J. Romero, R. Babbush, and A. Aspuru-Guzik, “The theory of variational hybrid quantum-classical algorithms”, *New Journal of Physics*, vol. 18, no. 2, p. 023 023, Feb. 2016.
- [185] G. A. Quantum, Collaborators*†, F. Arute, K. Arya, R. Babbush, D. Bacon, J. C. Bardin, R. Barends, S. Boixo, M. Broughton, B. B. Buckley, *et al.*, “Hartree-fock on a superconducting qubit quantum computer”, *Science*, vol. 369, no. 6507, pp. 1084–1089, 2020.
- [186] C. Hempel, C. Maier, J. Romero, J. McClean, T. Monz, H. Shen, P. Jurcevic, B. P. Lanyon, P. Love, R. Babbush, A. Aspuru-Guzik, R. Blatt, and C. F. Roos, “Quantum Chemistry Calculations on a Trapped-Ion Quantum Simulator”, *Physical Review X*, vol. 8, 031022, p. 031 022, Jul. 2018.
- [187] A. Kandala, A. Mezzacapo, K. Temme, M. Takita, M. Brink, J. M. Chow, and J. M. Gambetta, “Hardware-efficient variational quantum eigensolver for small molecules and quantum magnets”, *Nature*, vol. 549, p. 242, Sep. 2017. [Online]. Available: <https://doi.org/10.1038/nature23879>.
- [188] Y. Li and S. C. Benjamin, “Efficient variational quantum simulator incorporating active error minimization”, *Phys. Rev. X*, vol. 7, p. 021 050, 2 Jun. 2017. [Online]. Available: <https://link.aps.org/doi/10.1103/PhysRevX.7.021050>.
- [189] P. J. J. O’Malley, R. Babbush, I. D. Kivlichan, J. Romero, J. R. McClean, R. Barends, J. Kelly, P. Roushan, A. Tranter, N. Ding, B. Campbell, Y. Chen, Z. Chen, B. Chiaro, A. Dunsworth, A. G. Fowler, E. Jeffrey, E. Lucero,

BIBLIOGRAPHY

- A. Megrant, J. Y. Mutus, M. Neeley, C. Neill, C. Quintana, D. Sank, A. Vainsencher, J. Wenner, T. C. White, P. V. Coveney, P. J. Love, H. Neven, A. Aspuru-Guzik, and J. M. Martinis, “Scalable quantum simulation of molecular energies”, *Phys. Rev. X*, vol. 6, p. 031 007, 3 Jul. 2016. [Online]. Available: <https://link.aps.org/doi/10.1103/PhysRevX.6.031007>.
- [190] A. Peruzzo, J. McClean, P. Shadbolt, M.-H. Yung, X.-Q. Zhou, P. J. Love, A. Aspuru-Guzik, and J. L. O’Brien, “A variational eigenvalue solver on a photonic quantum processor”, *Nature Communications*, vol. 5, p. 4213, Jul. 2014. [Online]. Available: <https://doi.org/10.1038/ncomms5213>.
- [191] D. Zhu, N. M. Linke, M. Benedetti, K. A. Landsman, N. H. Nguyen, C. H. Alderete, A. Perdomo-Ortiz, N. Korda, A. Garfoot, C. Brecque, L. Egan, O. Perdomo, and C. Monroe, “Training of quantum circuits on a hybrid quantum computer”, *Science Advances*, vol. 5, no. 10, 2019. eprint: <https://advances.sciencemag.org/content/5/10/eaaw9918.full.pdf>. [Online]. Available: <https://advances.sciencemag.org/content/5/10/eaaw9918>.
- [192] V. Havlíček, A. D. Córcoles, K. Temme, A. W. Harrow, A. Kandala, J. M. Chow, and J. M. Gambetta, “Supervised learning with quantum-enhanced feature spaces”, *Nature*, vol. 567, no. 7747, pp. 209–212, 2019. [Online]. Available: <https://doi.org/10.1038/s41586-019-0980-2>.
- [193] G. Pagano, A. Bapat, P. Becker, K. S. Collins, A. De, P. W. Hess, H. B. Kaplan, A. Kyprianidis, W. L. Tan, C. Baldwin, *et al.*, “Quantum approximate optimization of the long-range ising model with a trapped-ion quantum

BIBLIOGRAPHY

- simulator”, *Proceedings of the National Academy of Sciences*, vol. 117, no. 41, pp. 25 396–25 401, 2020.
- [194] M. P. Harrigan, K. J. Sung, M. Neeley, K. J. Satzinger, F. Arute, K. Arya, J. Atalaya, J. C. Bardin, R. Barends, S. Boixo, *et al.*, “Quantum approximate optimization of non-planar graph problems on a planar superconducting processor”, *Nature Physics*, vol. 17, no. 3, pp. 332–336, 2021.
- [195] C. Kokail, C. Maier, R. van Bijnen, T. Brydges, M. K. Joshi, P. Jurcevic, C. A. Muschik, P. Silvi, R. Blatt, C. F. Roos, and P. Zoller, “Self-verifying variational quantum simulation of lattice models”, *Nature*, vol. 569, no. 7756, pp. 355–360, 2019. [Online]. Available: <https://doi.org/10.1038/s41586-019-1177-4>.
- [196] J. Romero, R. Babbush, J. R. McClean, C. Hempel, P. J. Love, and A. Aspuru-Guzik, “Strategies for quantum computing molecular energies using the unitary coupled cluster ansatz”, *Quantum Science and Technology*, vol. 4, no. 1, p. 014008, 2018.
- [197] A. Parra-Rodriguez, P. Lougovski, L. Lamata, E. Solano, and M. Sanz, “Digital-analog quantum computation”, *Phys. Rev. A*, vol. 101, p. 022 305, 2 Feb. 2020. [Online]. Available: <https://link.aps.org/doi/10.1103/PhysRevA.101.022305>.
- [198] A. Martin, L. Lamata, E. Solano, and M. Sanz, “Digital-analog quantum algorithm for the quantum fourier transform”, *Phys. Rev. Research*, vol. 2,

BIBLIOGRAPHY

- p. 013 012, 1 Jan. 2020. [Online]. Available: <https://link.aps.org/doi/10.1103/PhysRevResearch.2.013012>.
- [199] A. Galicia, B. Ramon, E. Solano, and M. Sanz, “Enhanced connectivity of quantum hardware with digital-analog control”, *Physical Review Research*, vol. 2, no. 3, p. 033 103, 2020.
- [200] R. Nandkishore and D. A. Huse, “Many-body localization and thermalization in quantum statistical mechanics”, *Annual Review of Condensed Matter Physics*, vol. 6, no. 1, pp. 15–38, 2015. eprint: <https://doi.org/10.1146/annurev-conmatphys-031214-014726>. [Online]. Available: <https://doi.org/10.1146/annurev-conmatphys-031214-014726>.
- [201] M. Schreiber, S. S. Hodgman, P. Bordia, H. P. Lüschen, M. H. Fischer, R. Vosk, E. Altman, U. Schneider, and I. Bloch, “Observation of many-body localization of interacting fermions in a quasirandom optical lattice”, *Science*, vol. 349, no. 6250, pp. 842–845, 2015, ISSN: 0036-8075. [Online]. Available: <http://science.sciencemag.org/content/349/6250/842>.
- [202] P. Bordia, H. P. Lüschen, S. S. Hodgman, M. Schreiber, I. Bloch, and U. Schneider, “Coupling identical one-dimensional many-body localized systems”, *Phys. Rev. Lett.*, vol. 116, p. 140 401, 14 Apr. 2016. [Online]. Available: <https://link.aps.org/doi/10.1103/PhysRevLett.116.140401>.
- [203] A. Lukin, M. Rispoli, R. Schittko, M. Tai, A. Kaufman, S. Choi, V. Khemani, J. L’eonard, and M. Greiner, “Probing entanglement in a many-body-localized system”, *Science*, vol. 364, pp. 256–260, 2019.

BIBLIOGRAPHY

- [204] K. Xu, J.-J. Chen, Y. Zeng, Y.-R. Zhang, C. Song, W. Liu, Q. Guo, P. Zhang, D. Xu, H. Deng, K. Huang, H. Wang, X. Zhu, D. Zheng, and H. Fan, “Emulating many-body localization with a superconducting quantum processor”, *Phys. Rev. Lett.*, vol. 120, p. 050 507, 5 Feb. 2018. [Online]. Available: <https://link.aps.org/doi/10.1103/PhysRevLett.120.050507>.
- [205] J. Smith, A. Lee, P. Richerme, B. Neyenhuis, P. W. Hess, P. Hauke, M. Heyl, D. A. Huse, and C. Monroe, “Many-body localization in a quantum simulator with programmable random disorder”, *Nature Physics*, vol. 12, 907 EP -, Jun. 2016. [Online]. Available: <https://doi.org/10.1038/nphys3783>.
- [206] M. Raghu, B. Poole, J. Kleinberg, S. Ganguli, and J. Sohl-Dickstein, “On the expressive power of deep neural networks”, in *international conference on machine learning*, PMLR, 2017, pp. 2847–2854.
- [207] I. Glasser, R. Sweke, N. Pancotti, J. Eisert, and I. Cirac, “Expressive power of tensor-network factorizations for probabilistic modeling”, *Advances in neural information processing systems*, vol. 32, 2019.
- [208] B. Vermersch, A. Elben, M. Dalmonte, J. I. Cirac, and P. Zoller, “Unitary n -designs via random quenches in atomic hubbard and spin models: Application to the measurement of rényi entropies”, *Phys. Rev. A*, vol. 97, p. 023 604, 2 Feb. 2018. [Online]. Available: <https://link.aps.org/doi/10.1103/PhysRevA.97.023604>.

BIBLIOGRAPHY

- [209] D. H. ACKLEY, G. E. HINTON, and T. J. SEJNOWSKI, “A learning algorithm for boltzmann machines”, in *Readings in Computer Vision*, M. A. Fischler and O. Firschein, Eds., San Francisco (CA): Morgan Kaufmann, 1987, pp. 522–533, ISBN: 978-0-08-051581-6. [Online]. Available: <http://www.sciencedirect.com/science/article/pii/B9780080515816500532>.
- [210] M. H. Amin, E. Andriyash, J. Rolfe, B. Kulchytskyy, and R. Melko, “Quantum boltzmann machine”, *Phys. Rev. X*, vol. 8, p. 021 050, 2 May 2018. [Online]. Available: <https://link.aps.org/doi/10.1103/PhysRevX.8.021050>.
- [211] E. R. Anschuetz and Y. Cao, “Realizing Quantum Boltzmann Machines Through Eigenstate Thermalization”, *arXiv e-prints*, arXiv:1903.01359, arXiv:1903.01359, Mar. 2019. arXiv: [1903.01359](https://arxiv.org/abs/1903.01359) [quant-ph].
- [212] M. Serbyn, Z. Papi , and D. A. Abanin, “Local conservation laws and the structure of the many-body localized states”, *Phys. Rev. Lett.*, vol. 111, p. 127 201, 12 Sep. 2013. [Online]. Available: <https://link.aps.org/doi/10.1103/PhysRevLett.111.127201>.
- [213] D. A. Huse, R. Nandkishore, and V. Oganesyan, “Phenomenology of fully many-body-localized systems”, *Phys. Rev. B*, vol. 90, p. 174 202, 17 Nov. 2014. [Online]. Available: <https://link.aps.org/doi/10.1103/PhysRevB.90.174202>.
- [214] J. Z. Imbrie, “On many-body localization for quantum spin chains”, *Journal of Statistical Physics*, vol. 163, no. 5, pp. 998–1048, Apr. 2016. [Online]. Available: <https://doi.org/10.1007/s10955-016-1508-x>.

Appendix A

Mapping procedure from COE dynamics to complex Ising models

In this section, we prove Eq. (2.5) by providing justifications of the diagrammatic recipes to map the the evolution \hat{U}_{COE} on a Ising spin model with complex fields. Again, the quantum gates of interest consist of both diagonal gates $\{\hat{T}, CZ\}$ and non-diagonal gates $\{\sqrt{\hat{\sigma}^x}, \sqrt{\hat{\sigma}^y}, \sqrt{\hat{\sigma}^{y^T}}, \hat{H}\}$. For simplicity, we start with one- and two-qubit examples before generalizing to the COE dynamics. The mathematical procedure here is adapted from Ref. [57].

A.1 One-qubit example

Let us consider a one-qubit circuit and $N_g + 1$ gates randomly chosen from the set $\{\sqrt{\hat{\sigma}^x}, \sqrt{\hat{\sigma}^y}, \sqrt{\hat{\sigma}^{y^T}}, \hat{T}\}$. The zeroth gate is fixed to be a Hadamard gate. The output probability is $p(z) = |\langle z | \hat{U} | 0 \rangle|^2$, where $\hat{U} = \prod_{n=0}^{N_g} \hat{U}^{(n)}$ is the total unitary matrix, $\hat{U}^{(n)}$ is the n^{th} gate and $z \in \{0, 1\}$ is the readout bit. Below, we outline the mathematical steps underlying the diagrammatic approach followed by detailed

APPENDIX A. MAPPING PROCEDURE FROM COE DYNAMICS TO
COMPLEX ISING MODELS

explanations for each step:

$$p(z) = \left| \langle z | \prod_{n=0}^{N_g} \hat{U}^{(n)} | 0 \rangle \right|^2 \quad (\text{A.1})$$

$$= \left| \sum_{\mathbf{z} \in \{0,1\}^N} \prod_{n=0}^{N_g} \langle z_n | \hat{U}^{(n)} | z_{n-1} \rangle \right|^2 \quad (\text{A.2})$$

$$= \left| \sum_{\mathbf{z} \in \{0,1\}^{N_g}} \prod_{n=0}^N A(z_n, z_{n-1}) \exp \left[\frac{i\pi}{4} \Phi(z_n, z_{n-1}) \right] \right|^2 \quad (\text{A.3})$$

$$= \left| \sum_{\mathbf{z} \in \{0,1\}^{N_g+2}} A(\mathbf{z}) \exp \left[\frac{i\pi}{4} \sum_{n=0}^{N_g} \Phi(z_n, z_{n-1}) \right] \right|^2. \quad (\text{A.4})$$

In the second line, we insert an identity $\hat{I}_n = \sum_{z_n \in \{0,1\}} |z_n\rangle\langle z_n|$ between $\hat{U}^{(n+1)}$ and $\hat{U}^{(n)}$ for every $n \in \{0, \dots, N_g - 1\}$. As a result, this line can be interpreted as the Feynman's path integral where each individual path or 'world-line' is characterized by a sequence of basis variables $\mathbf{z} = (z_{-1}, z_0, \dots, z_{N_g})$. The initial and the end points for every path are $|z_{-1}\rangle = |0\rangle$ and $|z_{N_g}\rangle = |z\rangle$, respectively. In the third line, we decompose $\langle z_n | \hat{U}^{(n)} | z_{n-1} \rangle$ into the amplitude $A(z_n, z_{n-1})$ and phase $\Phi(z_n, z_{n-1})$. In the fourth line, we introduce $A(\mathbf{z}) = \prod_{n=0}^{N_g} A(z_n, z_{n-1})$. The equation now takes the form of the partition of a classical Ising model with complex energies. Here, \mathbf{z} can be interpreted as a classical spin configuration, $A(\mathbf{z})$ as the degeneracy number and $\frac{i\pi}{4}\Phi(z_n, z_{n-1})$ as a complex energy associated with spin-spin interaction.

Further simplifications are possible by noticing that, the diagonal gates in the circuits allow the reduction of the number of classical spins. Specifically, if a \hat{T} gate is applied to $|z_{n-1}\rangle$, it follows that $z_n = z_{n-1}$. Hence, the variables z_{n-1} and z_n can be represented by a single classical spin state. The two variables z_{n-1}, z_n become independent only when a non-diagonal gate is applied. Therefore, we can group all variables $\{z_n\}$ between two non-diagonal gates as one classical spin. This

APPENDIX A. MAPPING PROCEDURE FROM COE DYNAMICS TO
COMPLEX ISING MODELS

procedure leads to the directives presented as the the STEP I of the mapping procedure in Section 2.3.1.1 in Chapter 2. Formally, for $N_s + 1$ non-diagonal gates in the circuit (including the first Hadamard gate) \mathbf{z} can be characterized by a classical spin configuration $\mathbf{s} = (s_{-1}, s_0, \dots, s_k, \dots, s_{N_s})$ where $s_k = 1 - 2z_k \in \{\pm 1\}$ is a spin representing the basis variable immediately after the k^{th} non-diagonal gate, i.e.

$$p(z) = \left| \sum_{\mathbf{s} \in \{\pm 1\}^{N_s+1}} A(\mathbf{s}) \exp \left[\frac{i\pi}{4} \sum_{k=0}^{N_s} \Phi(s_k, s_{k-1}) \right] \right|^2 \quad (\text{A.5})$$

$$= |Z_{\text{Ising}}|^2 \quad (\text{A.6})$$

Lastly, we need to specify $A(\mathbf{s})$ and $\Phi(s_k, s_{k-1})$ in term of the local fields h_{k-1} , h_k , the interaction $J_{k-1,k}$, and spin configurations s_{k-1}, s_k . This is done by first considering the gates in their matrix form, i.e.

APPENDIX A. MAPPING PROCEDURE FROM COE DYNAMICS TO
COMPLEX ISING MODELS

$$\sqrt{\hat{\sigma}^x} = \frac{1}{\sqrt{2}} \begin{pmatrix} e^{\frac{i\pi}{2}} & 1 \\ 1 & e^{\frac{i\pi}{2}} \end{pmatrix} = \frac{1}{\sqrt{2}} \left[e^{\frac{i\pi}{4}(1+s_k s_{k-1})} \right]_{s_k, s_{k-1}}, \quad (\text{A.7})$$

$$\sqrt{\hat{\sigma}^y} = \frac{1}{\sqrt{2}} \begin{pmatrix} 1 & -1 \\ 1 & 1 \end{pmatrix} = \frac{1}{\sqrt{2}} \left[e^{\frac{i\pi}{4}(1-s_{k-1})(1+s_k)} \right]_{s_k, s_{k-1}}, \quad (\text{A.8})$$

$$\sqrt{\hat{\sigma}^{yT}} = \frac{1}{\sqrt{2}} \begin{pmatrix} 1 & 1 \\ -1 & 1 \end{pmatrix} = \frac{1}{\sqrt{2}} \left[e^{\frac{i\pi}{4}(1+s_{k-1})(1-s_k)} \right]_{s_k, s_{k-1}}, \quad (\text{A.9})$$

$$\hat{H} = \frac{1}{\sqrt{2}} \begin{pmatrix} 1 & 1 \\ 1 & -1 \end{pmatrix} = \frac{1}{\sqrt{2}} \left[e^{\frac{i\pi}{4}(1-s_{k-1})(1-s_k)} \right]_{s_k, s_{k-1}}, \quad (\text{A.10})$$

$$\hat{T} = \begin{pmatrix} 1 & 0 \\ 0 & e^{\frac{i\pi}{4}} \end{pmatrix} = \text{Diag} \left[e^{\frac{i\pi}{4}(\frac{1-s_k}{2})} \right]_{s_k} \quad (\text{A.11})$$

Notice that all non-diagonal gates contribute to the same amplitude $A(s_k, s_{k-1}) = 1/\sqrt{2}$, leading to $A(\mathbf{s}) = 2^{-(N_S+1)/2}$. Hence, we can extract the contribution of each gate to $\Phi(s_k, s_{k-1})$ as

$$\Phi_{\sqrt{\hat{\sigma}^x}}(s_k, s_{k-1}) = 1 + s_{k-1}s_k, \quad (\text{A.12})$$

$$\Phi_{\sqrt{\hat{\sigma}^y}}(s_k, s_{k-1}) = (1 - s_{k-1})(1 + s_k) \quad (\text{A.13})$$

$$= 1 - s_{k-1} + s_k - s_{k-1}s_k, \quad (\text{A.14})$$

$$\Phi_{\sqrt{\hat{\sigma}^{yT}}}(s_k, s_{k-1}) = (1 + s_{k-1})(1 - s_k) \quad (\text{A.15})$$

$$= 1 + s_{k-1} - s_k - s_{k-1}s_k, \quad (\text{A.16})$$

$$\Phi_{\hat{T}}(s_k) = \frac{1 - s_k}{2}. \quad (\text{A.17})$$

The under-script indicates which gate is contributing to the phase. The cor-

APPENDIX A. MAPPING PROCEDURE FROM COE DYNAMICS TO
COMPLEX ISING MODELS

responding h_i , h_j and J_{ij} are depicted in the lookup table in Fig. 2.1(f), where $i = k - 1$ and $j = k$. The global phase that does not depend on \mathbf{s} is ignored as it does not contribute to $p(z)$.

A.2 Two-qubit example

Now we consider a two-qubit random circuits to demonstrate the action of the CZ gates. We introduce a new index $l \in \{1, 2\}$ to label each qubit, which is placed on a given horizontal line (row). Since the CZ gate is diagonal, its presence does not alter the number of spins in each row. However, the gate introduces interaction between spins in different rows. This can be seen from its explicit form, i.e.

$$CZ = \begin{pmatrix} 1 & 0 & 0 & 0 \\ 0 & 1 & 0 & 0 \\ 0 & 0 & 1 & 0 \\ 0 & 0 & 0 & -1 \end{pmatrix} = \text{Diag} \left[e^{\frac{i\pi}{4}(1-s_{1,k})(1-s_{2,k'})} \right]_{s_{1,k}, s_{2,k'}}, \quad (\text{A.18})$$

where $s_{1,k}$ ($s_{2,k'}$) is the state of the k^{th} (k^{th}) spin at the first (second) row. It follows that

$$\Phi_{s_{1,k}, s_{2,k'}}^{CZ} = (1 - s_{1,k})(1 - s_{2,k'}) \quad (\text{A.19})$$

$$= 1 - s_{1,k} - s_{2,k'} + s_{1,k}s_{2,k'}. \quad (\text{A.20})$$

The corresponding h_i , h_j , and J_{ij} are depicted in Fig. 2.1(f) where $i = (1, k)$ and $j = (2, k')$. We have now derived all necessary ingredients to map a random

quantum circuit to a classical Ising model.

A.3 Full COE dynamics

Since the COE dynamics can be expressed in terms of a quasi-random quantum circuit, we can straightforwardly apply the above procedure to find the corresponding Ising model. The complexity here solely arises from the number of indices required to specify the positions of all the gates in the circuit. To deal with this, we introduce the following indices

- an index $l \in \{1, \dots, L\}$ to indicate which qubit / row.
- an index $m \in \{1, \dots, M\}$ to indicate which period.
- an index $\mu \in \{A, B\}$ to indicate which part of the period. A and B refer to the \hat{U}_{CUE} part and the \hat{U}_{CUE}^T part, respectively
- an index $k \in \{0, 1, \dots, N_S(l)\}$ to indicate the spin position for a given m and μ . Here, $N_S(l)$ is the total number of spins at the l^{th} row. Note that due to the symmetric structure of \hat{U}_{CUE} and \hat{U}_{CUE}^T , we run the index k backward for the transpose part, i.e. $k = 0$ refers to the last layer.
- an index $\nu_{l,k}$ so that $\nu_{l,k} = 1$ if the k^{th} non-diagonal gate acting on the qubit l is $\sqrt{\hat{\sigma}^x}$ otherwise $\nu_{l,k} = 0$.

With these indices, the partition function of the circuit, as shown in Fig. 2.1(a), can be written as

$$\langle \mathbf{z} | \psi \rangle = 2^{-\frac{G}{2}} \sum_{\mathbf{s} \in \mathcal{S}} \exp \left[\frac{i\pi}{4} E(\mathbf{s}) \right], \quad (\text{A.21})$$

APPENDIX A. MAPPING PROCEDURE FROM COE DYNAMICS TO
COMPLEX ISING MODELS

with

$$\begin{aligned}
E(\mathbf{s}) = & E(\mathbf{z}) + \sum_{m=1}^M \sum_{\mu=A}^B \sum_{l=1}^L \sum_{k=0}^{N_S(l)} h_{lk} s_{l,k}^{\mu,m} \\
& + \sum_{m=1}^M \sum_{\mu=A}^B \sum_{l=1}^L \sum_{k=1}^{N_S(l)} (2\nu_{l,k} - 1) s_{l,k-1}^{\mu,m} s_{l,k}^{\mu,m} \\
& + \sum_{m=1}^M \sum_{\mu=A}^B \sum_{l=1}^L \sum_{l'=1}^{l-1} \sum_{k=1}^{N_S(l)} \sum_{k'=1}^{N_S(l')} \zeta_{(l,k)}^{(l',k')} s_{l,k}^{\mu,m} s_{l',k'}^{\mu,m},
\end{aligned} \tag{A.22}$$

and

$$h_{lk} = \nu_{l,k+1} - \nu_{l,k} - \frac{1}{2} N_T(l, k) - N_{CZ}(l, k), \tag{A.23}$$

$$E(\mathbf{z}) = -s_{0,l}^{B,M} - s_{z_l} + s_{0,l}^{B,M} s_{z_l}. \tag{A.24}$$

Here G is the total number of non-diagonal gates in the circuit. $\zeta_{(l,k)}^{(l',k')}$ represents the total number of CZ gates which introduces the interaction between spins $s_{l,k}^{\mu,m}$ and $s_{l',k'}^{\mu,m}$. $N_{CZ}(l, k)$ ($N_T(l, k)$) is the total number of CZ (T) gates which introduces local fields on the spin $s_{l,k}^{\mu,m}$. $E(\mathbf{z})$ is the contribution from the last Hadamard layer which depends on the readout bit-string \mathbf{z} . $\{s_{z_l}\}$ are the spins corresponding to \mathbf{z} and their configuration is fixed. In addition, there are also two extra boundary conditions (i) between part A and B and (ii) between the two adjacent periods m and $m + 1$, i.e. $s_{l,N_S(l)}^{A,m} = s_{l,N_S(l)}^{B,m}$ and $s_{l,0}^{A,m+1} = s_{l,0}^{B,m}$.

Appendix B

MBL phase and its sampling complexity

We here provide a more detailed mathematical description of the MBL phase and its connection to quantum supremacy signatures. We focus on demonstrating that the probability distribution $p_m(\mathbf{z})$ of a quantum state evolving under its dynamics fails to satisfy the anti-concentration condition given in Eq. (3.10). Finally, we discuss the feasibility to efficiently construct a classical sampler \mathcal{C} capable of providing bitstrings from a distribution $q(\mathbf{z})$ that is additively closed to $p_m(\mathbf{z})$ as defined in Eq. (3.9).

B.1 General framework

The standard approach to describe the MBL phase is via a complete set of quasi-local integral of motions [138, 212–214], defined as $[\hat{\tau}_i^z, \hat{H}_{\text{MBL}}] = 0$, where

$$\hat{\tau}_i^z = Z \hat{\sigma}_i^z + \sum_{m=1} e^{-m/\xi} \hat{O}_i^{(m)}. \quad (\text{B.1})$$

Here, $Z \approx 1$, $\xi \ll 1$ is the characteristic localization length and $\hat{O}_i^{(m)}$ are generic operators describing interaction between up to $(2m + 1)$ -body over sites from $i - m$

to $i + m$. A generic MBL Hamiltonian then adopts the form

$$\hat{H}_{\text{MBL}} = \sum_i h_i \hat{\tau}_i^z + \sum_{i < j} J_0 e^{-|i-j|/\xi'} \hat{\tau}_i^z \hat{\tau}_j^z \quad (\text{B.2})$$

$$+ \sum_{i < j < k} J_0 e^{-|i-k|/\xi'} \hat{\tau}_i^z \hat{\tau}_j^z \hat{\tau}_k^z + \dots, \quad (\text{B.3})$$

where $h_i \in [0, W]$ are on-site energies uniformly drawn from a random distribution, J_0 is an effective interaction strength and $\xi' \sim \xi$ is an additional localization length. For periodically driven systems, the standard approach is to cast the Floquet Hamiltonian \hat{H}_F onto the form of Eq. (B.2) [156].

B.2 Concentration of output distribution

By inserting Eq. (B.1) into Eq. (B.2), The MBL Hamiltonian can be expanded as a perturbation series

$$\hat{H}_{\text{MBL}} = \hat{H}_0 + \sum_{m=1}^{\infty} \sum_{i=1}^L \epsilon^m \hat{V}_i^{(m)}, \quad (\text{B.4})$$

where $\epsilon = e^{-1/\xi} \ll 1$ (we took $\xi' = \xi$ for simplicity), $\hat{H}_0 = \sum_i h_i Z \hat{\sigma}_i^z$ is the non-interacting part and $\hat{V}_i^{(m)}$ are local perturbations acting on at most sites from $i - m$ to $i + m$. At first order perturbation ($m = 1$), $\hat{V}_i^{(1)}$ can flip at max 3 neighbouring spins and can thus only mix an unperturbed product state of L spins $|\mathbf{z}_0\rangle$ with up to $4L$ different basis states (neglecting the boundary corrections). The same logic applies at second order perturbation where this time $|\mathbf{z}_0\rangle$ becomes a linear superposition of up to $16L$ additional basis states. As the order of perturbation increases, a polynomial number (in L) of additional basis states have to be taken into account. This is a consequence of the local nature of each perturbation term.

APPENDIX B. MBL PHASE AND ITS SAMPLING COMPLEXITY

In contrast, extended interactions, as it would be the case in the thermal phase, would lead to an exponential increase of additional basis states. Assuming that an initial product state evolves deep inside the MBL phase where only few orders of perturbation is required, the output state would only have a polynomial number of basis state populated. Since the anti-concentration condition in Eq. (3.10) requires most of the 2^L basis states to be populated, the output distribution in the MBL phase can not satisfy it.

B.3 Complexity of sampling task

Previous works have demonstrated the ability of MPS states to efficiently approximate all eigenstates of any MBL Hamiltonians [138, 157]. In what follows we denote an exact eigenstate of \hat{H}_{MBL} with eigenenergy E_k as $|\varphi_k\rangle$ and the associated MPS approximation as $|\text{MPS}_k\rangle$. We define the error made by the approximation, $\nu \ll 1$, as

$$|\text{MPS}_k\rangle = (1 - \nu)|\varphi_k\rangle + \sqrt{2\nu - \nu^2} \sum_{k' \neq k} a_{kk'} |\varphi_{k'}\rangle \quad (\text{B.5})$$

$$\approx |\varphi_k\rangle + \sqrt{2\nu} \sum_{k' \neq k} a_{kk'} |\varphi_{k'}\rangle, \quad (\text{B.6})$$

where $\sum_{k' \neq k} a_{kk'}$ captures the overlap over all other eigenstates $|\varphi_{k'}\rangle$ with $\sum_{k' \neq k} |a_{kk'}|^2 =$

1. The mean energy associated with $|\text{MPS}_k\rangle$ can be written as

$$\tilde{E}_k = \langle \text{MPS}_k | \hat{H}_{\text{MBL}} | \text{MPS}_k \rangle \quad (\text{B.7})$$

$$\approx E_k + 2\nu \sum_{k' \neq k} |a_{kk'}|^2 E_{k'} \quad (\text{B.8})$$

$$\equiv E_k + 2\nu \Lambda_k, \quad (\text{B.9})$$

APPENDIX B. MBL PHASE AND ITS SAMPLING COMPLEXITY

where $\Lambda_{k'}$ represents the average over the entire energy spectrum following the “error distribution” $\sum_{k' \neq k} |a_{kk'}|^2$. The bond dimension of the MPS states required to maintain a fix level of precision ν have been shown to scale polynomially with the system size L [138, 157]; the exact scaling depends on the specifics of \hat{H}_{MBL} . The approximated output probability distribution $q_t(\mathbf{z})$, after evolving from the initial state $|\mathbf{z}_0\rangle$ for a time t , then reads

$$q_t(\mathbf{z}) = \left| \langle \mathbf{z} | \left(\sum_k e^{-i\hat{E}_k t} |\text{MPS}_k\rangle \langle \text{MPS}_k| \right) | \mathbf{z}_0 \rangle \right|^2 \quad (\text{B.10})$$

$$\approx \left| \langle \mathbf{z} | \sum_k e^{-i(E_k + 2\nu\Lambda_k)t} \left(|\varphi_k\rangle \langle \varphi_k| + \sqrt{2\nu} \sum_{k' \neq k} [a_{kk'} |\varphi_{k'}\rangle \langle \varphi_k| + \text{H.c.}] \right) | \mathbf{z}_0 \rangle \right|^2 \quad (\text{B.11})$$

$$\approx \left| \langle \mathbf{z} | \sum_k e^{-iE_k t} \left([1 - 2i\nu\Lambda_k t] |\varphi_k\rangle \langle \varphi_k| + \sqrt{2\nu} \sum_{k' \neq k} [a_{kk'} |\varphi_{k'}\rangle \langle \varphi_k| + \text{H.c.}] \right) | \mathbf{z}_0 \rangle \right|^2 \quad (\text{B.12})$$

$$\approx p(\mathbf{z}) + \left[\sqrt{2\nu} \sum_{k,k'} e^{-i(E_k - E_{k'})t} \langle \mathbf{z} | \hat{P}_k | \mathbf{z}_0 \rangle \langle \mathbf{z}_0 | \hat{M}_{k'} | \mathbf{z} \rangle + 2i\nu t \sum_{k,k'} e^{-i(E_k - E_{k'})t} \Lambda_{k'} \langle \mathbf{z} | \hat{P}_k | \mathbf{z}_0 \rangle \langle \mathbf{z}_0 | \hat{P}_{k'} | \mathbf{z} \rangle + c.c. \right]. \quad (\text{B.13})$$

Here $\hat{P}_k = |\varphi_k\rangle \langle \varphi_k|$, $\hat{M}_k = \sum_{k' \neq k} a_{kk'} |\varphi_{k'}\rangle \langle \varphi_k| + \text{H.c.}$ and the exact distribution is given by $p_t(\mathbf{z}) = \left| \sum_k e^{-iE_k t} \langle \mathbf{z} | \hat{P}_k | \mathbf{z}_0 \rangle \right|^2$. In the above expression, we keep only the leading order in ν and νt and we considered the limit $\nu\Lambda_k t \ll 1$.

In the short time limit where the last term in the last line of Eq. (B.10) can be neglected, the error made in approximating $p_t(\mathbf{z})$ is proportional to $\sqrt{2\nu} \sum_k e^{-iE_k t} \langle \mathbf{z} | \hat{P}_k | \mathbf{z}_0 \rangle$. Following the discussion in the previous subsection, we know that for a dynamics deep in the MBL phase, only a small fraction $[\text{poly}(L)/2^L]$ of $\langle \mathbf{z} | \hat{P}_k | \mathbf{z}_0 \rangle$ will be

APPENDIX B. MBL PHASE AND ITS SAMPLING COMPLEXITY

nonzero and at max proportional to $e^{-1/\xi}$. Therefore, the additive error condition in Eq. (3.9), i.e. $\sum_{\mathbf{z}} |p_t(\mathbf{z}) - q_t(\mathbf{z})| \leq \beta_0$, is expected to be reachable with arbitrary small β_0 for bond dimensions of the MPS states that scale polynomially with the system size. For longer evolution times, the term proportional to νt will start to become increasingly important. It will inevitably reach a point where any small initial mistake $2\nu\Lambda_k$ made estimating the eigenenergies accumulates, leading to a large error in the phases. While any approximation method should fail in this very large time limit, we note that the same is bounded to happen for a quantum simulator; any small amount of dephasing or decay will inevitably accumulate beyond the required accuracy in the large time limit.